國立臺灣大學工學院土木工程學系

碩士論文

Department of Civil Engineering
College of Engineering
National Taiwan University

Master's Thesis

海床拖錨承載力之數值研究

Numerical Investigation of Capacity of Drag Embedment Anchors

楊承華

Cheng-Hua Yang

指導教授：郭安妮 博士

Advisor: Annie On-Lei Kwok, Ph.D.

中華民國 113 年 7 月

July, 2024

doi:10.6342/NTU202403515

謝辭

時光飛逝，兩年的碩士生活終於要畫下句點，首先要感謝郭安妮老師這兩年間的指導與栽培，老師自由的學風以及教學方式，允許我們獨自在學術的海洋中獨自遨遊與探索，不受任何拘束，讓我練就了一身探索的能力，非常感謝老師。

謝謝中神與和尚，常常在研究之餘一起相約打球紓壓，謝謝佳榮、政恩、家祥、凡哥，總能在我研究遇到問題時伸出援手，讓我在每個奮戰後的夜晚能安心睡覺。另外，謝謝昕成學長與奕杰學長在這段期間的照顧，不管遇到什麼問題，總是能給予我相當多的方向，有時候都覺得問到不好意思了，但學長總是能靜下心來回答我的白痴問題，對於兩位學長的拔刀相助，真是不知如何以言語表達我的感激之情。在台大的兩年，真是令我大開眼界，除了各位神人的腦袋令我望塵莫及，最讓我佩服的是研究室各位同學對於每件事的堅持與熱情，回想我 23 年來的人生經驗，這種體驗是從未有過的，也預祝研究室的各位未來一切順利。

謝謝研究所的路上遇到的所有人，沒有各位就沒有碩士學位，每一位對我的幫助我都永遠的記在心中，未來若有需要幫忙，必定鼎力相助。

最後，我要感謝我的家人，讓我能衣食無憂的在超貴的台北好好念書，也能理解我在研究所期間所受到的挑戰與磨練，感謝您們一路以來的照顧，讓我能平安地長大成人，讓我能無憂無慮的坐在這裡寫謝辭， 感謝您們的無私奉獻，我愛你們。

Ted

2024/08/05

doi:10.6342/NTU202403515

摘要

近年來，隨著環保意識的提升，各國積極推動綠色能源以減少碳排放。在各種綠色能源中，風力發電是台灣積極發展的領域之一。風力發電機的建設面臨許多挑戰，其中之一就是確保浮動平台的穩定性。本研究的目的是通過數值模擬評估拖曳式錨（Drag Embedment Anchor, DEA）的承載力。為了了解這種錨在海床中能夠提供多少承載力，必須了解錨在海床中的拖曳軌跡和行為。在本研究中，我們參考了美國船務局（American Bureau of Shipping, 2017）制定的方法，構建了錨在黏土海床中的軌跡和成載力的預測模型。然而，由於文獻和相關研究的有限性，目前尚無可靠的模型可用於預測錨在砂土中的拖曳軌跡。基於 ABS 方法預測的軌跡，本研究使用 ABAQUS 進行數值模擬，評估拖曳式錨在黏土地層中的成載力。結果表明，在不同深度、錨爪角度和土壤強度下，該數值模型具有良好的預測精度，這意味著該模型可能也適用於分析錨在黏土以外的地質材料組成的海床中的成載力。

本研究還考慮了地震載荷對拖曳式錨成載力的影響。具體而言，本研究探討了黏土的循環軟化對成載力的影響。循環軟化的程度取決於循環應變振幅和載荷循環次數。在本研究中，這兩個數值通過基於場地特定的地盤反應分析和基於 Tsai 等人（2014）的經驗模型來估算。隨後，進行數值模擬以評估拖曳錨在軟化後海床中的成載力。

。**關鍵字**：拖錨、ABAQUS、動態分析、地盤反應分析、循環軟化

doi:10.6342/NTU202403515

Abstract

In recent years, environmental awareness has surged, and countries are actively promoting green energy to reduce carbon emissions. Among various green energy sources, wind power generation is an area that Taiwan has been actively developing. The construction of wind turbine is one of the challenges that need to be addressed. The research objective of this study is to evaluate the holding capacity of drag embedment anchor (DEA) through numerical simulation. To understand how much holding capacity this anchor can provide for securing the floating platforms, it is necessary to understand the drag trajectory and behavior of the anchor in the seabed. In this study, we refer to the methods specified in the American Bureau of Shipping (2017) to construct a prediction model for the trajectory and holding capacity of the anchor in clay seabed. However, due to limited literature and related studies, reliable models for predicting the drag trajectory in sandy soils are not readily available. Using the predicted trajectory based on the ABS method, numerical simulations were conducted using ABAQUS to evaluate the holding capacity of drag embedment anchor in clayey seabed. The results showed good predictive accuracy at different depths, fluke angles, and soil strengths, indicating that this numerical model may be used for analyzing the holding capacity of drag anchors in seabed composed of geologic materials other than clays.

This study also considered the changes in the holding capacity of drag embedment anchors due to seismic loading. More specifically, this study examines the effect of cyclic softening of clays on the holding capacity. The amount of cyclic softening depends on the cyclic strain amplitude and the number of loading cycles. In this study, these two quantities were estimated by two methods, which are based on site-specific ground response analysis and an empirical model based on Tsai et al. (2014). Subsequently,

doi:10.6342/NTU202403515

numerical simulations were performed to evaluate the holding capacity of the drag anchor that were embedded in a softened seabed.

Key words：Drag Anchor, ABAQUS, Dynamic Analysis, Ground Response Analysis, Cyclic Softening

doi:10.6342/NTU202403515

TABLE OF CONTENTS

doi:10.6342/NTU202403515

doi:10.6342/NTU202403515

doi:10.6342/NTU202403515

doi:10.6342/NTU202403515

List of Figures

doi:10.6342/NTU202403515

doi:10.6342/NTU202403515

doi:10.6342/NTU202403515

doi:10.6342/NTU202403515

doi:10.6342/NTU202403515

doi:10.6342/NTU202403515

List of Tables

doi:10.6342/NTU202403515

doi:10.6342/NTU202403515

Chapter 1 Introduction

1.1 Motivation

Due to the global push for green energy development, offshore wind energy has received significant attention. The foundations of wind turbines can be classified into fixed foundations and floating foundations. Fixed foundations require piling to secure the base to the seabed, making construction feasible and economical only near the coast or in shallow water regions. Additionally, pile foundation relies on the bearing capacity of the soil. Hence, the piles may be very long if the geological condition of the seabed is undesirable or a large wind turbine is to be supported. On the other hand, the shallow water region will soon be saturated with offshore wind farms. The future wind turbines will have to be constructed in deep water region. Floating wind turbines are generally consisted of the floating platform, the mooring system and the anchor system. One type of anchors is the drag embedment anchor (DEA) which is dragged for a certain distance until it is completely embedded into the seabed. To determine the drag distance, it is essential to understand the drag trajectory of the drag embedment anchor in the seabed and its holding capacity. The purpose of this study is to develop the numerical models for evaluating the holding capacity. Additionally, since Taiwan is located in an active seismic zone, the impact of earthquake loading on the holding capacity will also be taken into consideration.

1.2 Research Method

This study first reconstructed the embedment trajectory of drag anchors based on past developed models. Then numerical models, which incorporated the anchor-soil interaction, were developed to evaluate the holding capacity. As the past embedment

doi:10.6342/NTU202403515

prediction models for drag anchor in sandy seabed were limited and found to be unreliable, predictions were exclusively made for clayey seabed, while extensive numerical simulations were conducted for sandy seabed such that an empirical model was subsequently derived to predict the holding capacity. Additionally, the study also analyzed the seismic impact on holding capacity. ABAQUS was employed as the numerical software in this research.

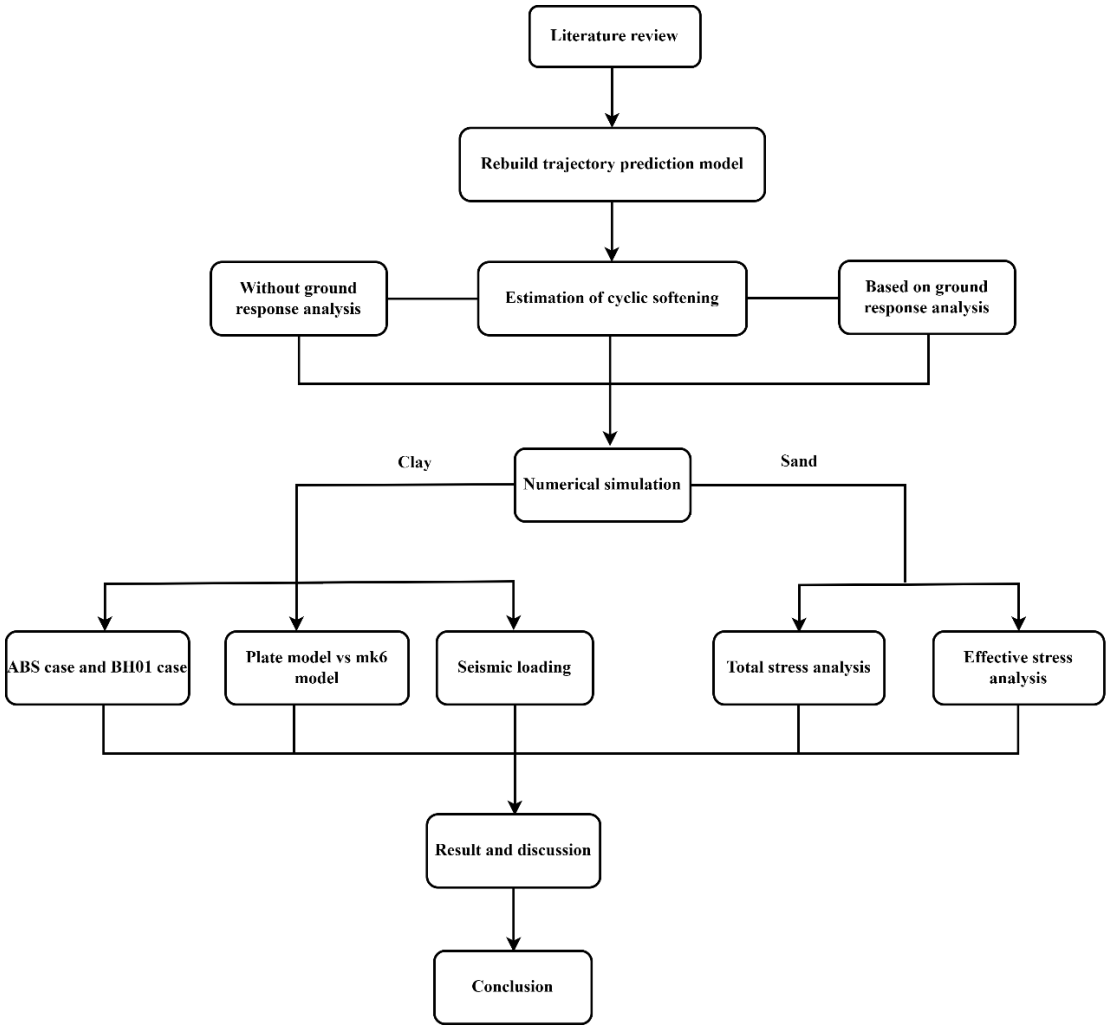

Figure 1. 1 The flowchart of this study

doi:10.6342/NTU202403515

1.3 Thesis Organization

The thesis is divided into five main chapters. Chapter 1 provides a brief overview of the research motivation, methods, and overall framework. Chapter 2 provides the literature review on the behavior of drag anchors in sandy and clayey soils, the influence of seismic loading on clay strength, the methodology for constructing the numerical model, and how to simulate the dynamic nonlinear behavior of soils in ABAQUS. Chapter 3 introduces the methods employed in this study, including trajectory prediction, numerical model for drag anchor simulation, parameters used to simulate the soil dynamic behavior, parameter calibration methods, and a compilation of the calculation steps, necessary parameters, and acquisition methods related to cyclic softening. Chapter 4 presents the numerical simulation results, which include the comparisons between the numerical model and solutions proposed by the American Bureau of Shipping (2017), as well as the impact of strength degradation on holding capacity. Chapter 5 concludes with findings based on the research results and offers recommendations for future studies. Figure 1.1 is a flowchart summarizing the research tasks completed in this study.

doi:10.6342/NTU202403515

Chapter 2 Literature Review

2.1 Borehole Location and Information

The drag embedment anchor analysis cases in this study are divided into sand and clay. For clay, two sets of soil parameters are used: those provided by ABS and those provided by the Taipower BH04 borehole. For sand, only the information provided by the BH04 borehole is used. This section introduces the location of the BH04 borehole and the soil information.

2.1.1 Introduction to the Taipower BH04 Borehole

The borehole data was based on Taiwan Power Company (2018). As shown in Figure 2.1, borehole BH04 is located offshore in the western part of Taiwan. The borehole data are presented in Table 2.1. When the undrained shear strength value is absent, it indicates that the soil layer is non-cohesive. The values in parentheses represent the average undrained shear strength.

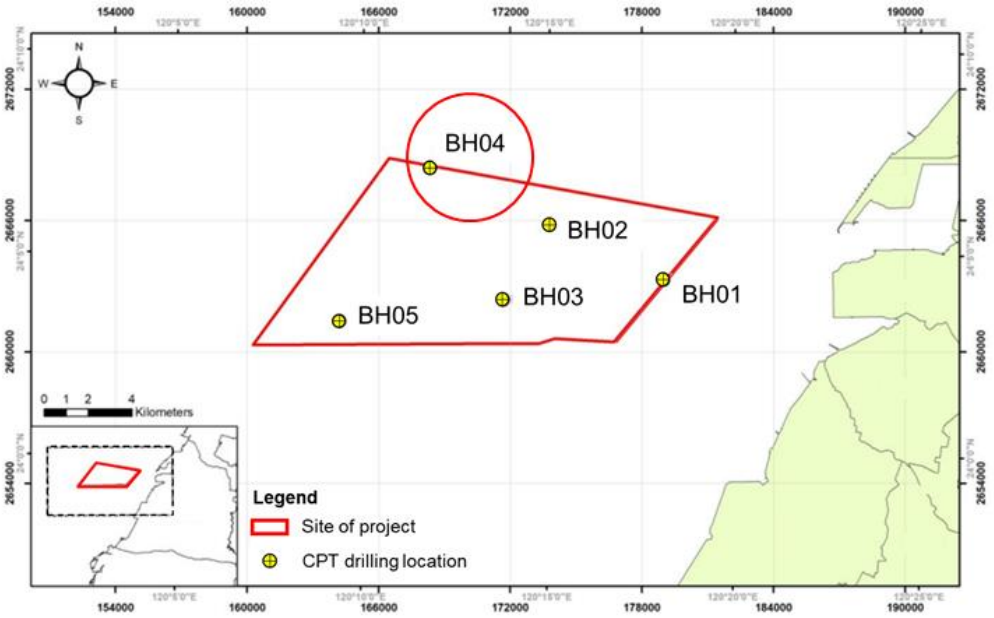

Figure 2. 1 Borehole location (Taiwan Power Company, 2018)

doi:10.6342/NTU202403515

Table 2.1 The information of BH04 borehole Sources: (Taiwan Power Company, 2018)

Depth	S_u (kPa)	Submerge unit weight (kN/m^3)	V_s (m/s)	G (MPa)	E (MPa)	ν
0~12m	6.9~145.8 (45.1)	4.8	88.6	13	33.9	0.3038
12~19.6m	33.5~353.7 (97.5)	7.3	162.8	47.9	124.6	0.3006
19.6~24.9m	67.4~447.6 (244.2)	7	184.6	59.3	154.3	0.3010
24.9~27.7m	36.2~356.1 (101.4)	7.6	189.6	66.1	171.8	0.2995
27.7~35.5m	-	8.3	228.3	98.1	255.1	0.3002
35.5~38.2m	45.7~169.4 (96.0)	8	217.1	86.5	225	0.3006
38.2~39.7m	-	9	258.5	129.4	336.5	0.3002
39.7~42.9m	47.8~500.1 (122.3)	8	230.9	98.3	255.6	0.3001

2.2 Behavior of the Drag Embedment Anchor in Clay

With the rise of offshore wind power generation, the method of securing wind turbines becomes a crucial issue. Drag anchor is one of the methods used for this purpose. Due to the fact that the bearing capacity of drag anchor typically increases with the depth of penetration, its penetration capability, along with the applied installation tension and trajectory prediction, is of paramount importance. In this section, we will introduce the behavior of drag anchor in clay and present a predictive procedure.

doi:10.6342/NTU202403515

2.2.1 Introduction of Drag Embedment Anchor

The American Bureau of Shipping (ABS) (2017) provides a detailed description of the construction and installation process of drag anchors. The drag anchor is designed to penetrate the seabed and provide holding capacity, with its load-bearing capacity being provided by the soil resistance in front of the anchor. The main components of a drag anchor are the fluke, shank, shackle, and chain or wire, shown in Figure 2.2. The fluke-shank angle (θ_{fs}) typically ranges from 30 degrees to 50 degrees. Higher angles are required for soft clay, while lower angles suffice for stiff clay or sands. This is because greater bearing capacity is needed in soft clay layers, and a 50 degrees penetration depth exceeds that of 30 degrees, thus providing higher bearing capacity.

The installation of the drag anchor is accomplished by dragging it through the soil. The load applied during dragging equals the design load. Once installed, it can resist a force equivalent to the installation load without the need for further penetration. In cohesive soils without layering, the drag anchor requires a horizontal dragging distance to achieve the desired design strength. As the dragging distance increases, the gradient of dragging distance to penetration depth decreases, shown in Figure 2.3 the fluke angle (θ_f) decreases as the penetration depth increases. When reaching the ultimate penetration depth (Z_{ult}) the fluke angle (θ_f) decreases to 0 degrees, and the drag anchor ceases to penetrate. In this state, the drag anchor achieves its maximum bearing capacity. Hence, ensuring accurate estimation of the installation tension and precise prediction of anchor trajectory during installation are crucial for design.

doi:10.6342/NTU202403515

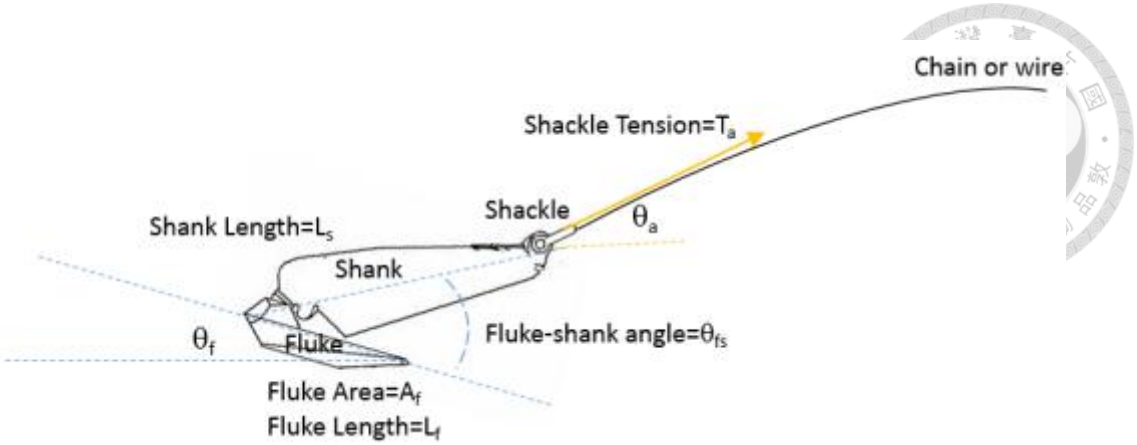

Figure 2. 2 Component of drag anchor (American Bureau of Shipping, 2017)

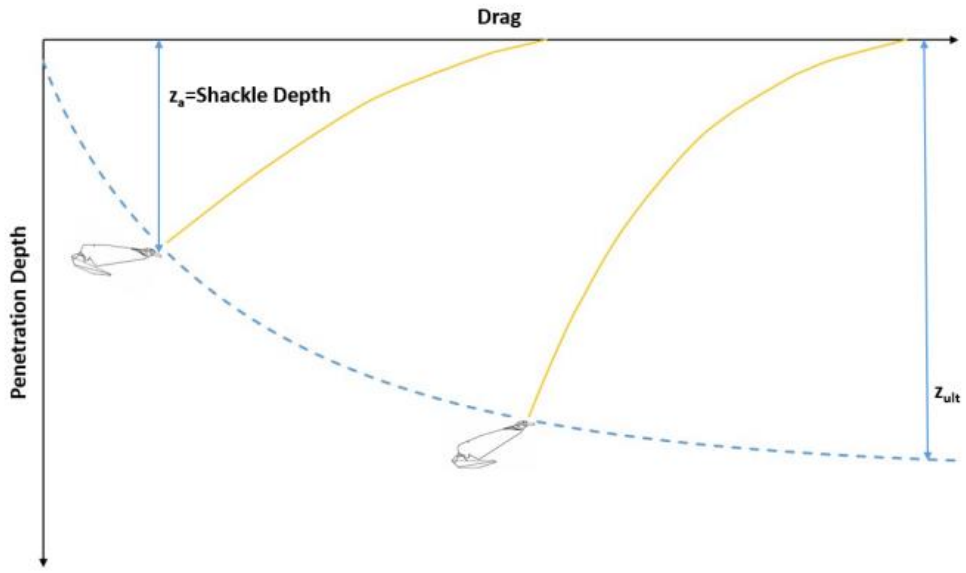

Figure 2. 3 Drag trajectory of drag anchor (American Bureau of Shipping, 2017)

2.2.2 Anchor Holding Capacity Under Combined Load

Drag anchors are typically subjected to normal (F_n), tangential (F_t), and moment loading (M), shown in Figure 2.4. In order to describe the interaction of these forces with the drag anchor, the relationship between shallow foundation and combined loading proposed by Murff (1994) has been adopted by O'Neill et al. (2003) and Aubeny and Chi (2010), characterizes the interaction as follows:

doi:10.6342/NTU202403515

$$f = (\frac{|c_1| N_e}{N_{n,\max}})^q + \left[\left(\frac{|c_3| N_e}{N_{m,\max}} \right)^m + \left(\frac{|c_2| N_e}{N_{t,\max}} \right)^n \right]^{\frac{1}{p}} - 1 = 0 \quad (2.1)$$

where

$$c_1 = \frac{F_n}{F} = \sin(\theta_a + \theta_f) \quad (2.2)$$

$$c_2 = \frac{F_t}{F} = \cos(\theta_a + \theta_f) \quad (2.3)$$

$$c_3 = \frac{M}{FL} = \left\{ \frac{e_t}{L} \sin(\theta_a + \theta_f) - \frac{e_n}{L} \cos(\theta_a + \theta_f) \right\} \quad (2.4)$$

$$N_{n,\max} = 3\pi + 2 + \frac{t}{L}(\alpha + \frac{1+\alpha}{\sqrt{2}}) \quad (2.5)$$

$$N_{t,\max} = 2\alpha + 15\frac{t}{L} \quad (2.6)$$

$$N_{m,\max} = \frac{\pi}{2}\left[1 + \left(\frac{t}{L} \right)^2 \right] \quad (2.7)$$

N_e is bearing capacity factor under combined loadings, $N_{n,\max}$ is bearing capacity factor under condition of pure normal loading, $N_{t,\max}$ is bearing capacity factor under condition of pure tangential loading, $N_{m,\max}$ is bearing capacity factor under condition of pure moment loading, n, m, p, q are interaction coefficients, Murff et al. (2005) provides recommended values for these interaction coefficients, shown in Table 2.1. c_1, c_2, c_3 are anchor equilibrium coefficients, θ_a is anchor line angle to horizontal at shackle point, θ_f is fluke angle to horizontal, L is fluke length, e_t is distances between the fluke centroid and the shackle measurement in the tangential direction, e_n is distances between the fluke centroid and the shackle measurement in the normal direction, t is fluke thickness, α is adhesion factor.

doi:10.6342/NTU202403515

After inserting the aforementioned coefficients into equation (2.1) and solving for the roots, we obtain the anchor bearing coefficient N_e under combined loading conditions. After determining the value of N_e, it can be plug into equation (2.8) to obtain the bearing capacity of the drag anchor at a specific location.

$$T_a = N_e S_u A_f \tag{2.8}$$

Equation (2.1) does not account for the bearing capacity provided by the shank, which is a reasonable assumption for thinner shanks but may lead to conservative predictions for thicker shanks.

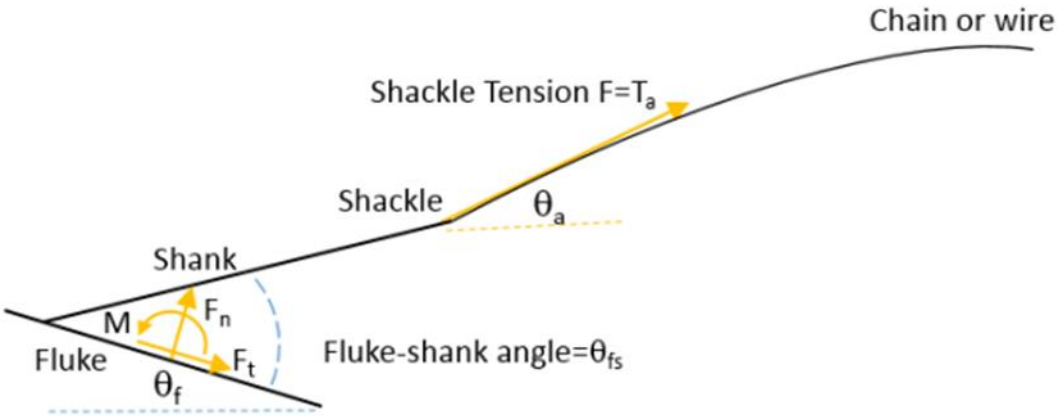

Figure 2. 4 The force situation of the drag anchor (American Bureau of Shipping, 2017)

Table 2.2 Values of interaction coefficient Sources: (Murff et al., 2005)

Exponent	Value
m	1.56
n	4.19
P	1.57
q	4.43

doi:10.6342/NTU202403515

2.2.3 Kinematic behavior

During the embedding process of the drag anchor, its motion involves translation and rotation. To assess the proportion of each motion behavior, the composite motion of the drag anchor is decomposed into tangential (v_t), normal (v_n), and rotational ($\dot{\beta}$) velocity components. These three velocity components are obtained by partial differentiation of Equation (2.1).

$$\dot{\beta} = \lambda \frac{\partial f}{\partial N_m} \tag{2.9}$$

$$v_n = \lambda \frac{\partial f}{\partial N_n} \tag{2.10}$$

$$v_t = \lambda \frac{\partial f}{\partial N_t} \tag{2.11}$$

Where λ is scalar multiplier.

Subsequently, using tangential velocity as a reference, the ratios of rotational motion to tangential motion velocity (R_{rt}) and normal motion to tangential motion velocity (R_{nt}) are established. These two coefficients are used to evaluate the proportion of other motion behaviors when tangential motion occurs. According to Aubeny and Chi (2014), when the fluke-shank angle is less than 60 degrees, the normal direction motion component relative to the tangential direction is very small and can be neglected, shown in Figure 2.5. VLA stands for vertical loaded anchor, and DEA stands for drag embedment anchor. Additionally, rotational motion is a combination of normal and tangential motion, so rotational motion can also be ignored. The movement of the drag anchor in the soil can be considered purely tangential.

doi:10.6342/NTU202403515

$$R_{rt}=\frac{\dot{\beta}L_f}{v_t}=\frac{c_3}{|c_3|}\frac{m}{n}\frac{N_{t,\max}}{N_{m,\max}}\frac{\left(\frac{|N_m|}{N_{m,\max}}\right)^{m-1}}{\left(\frac{|N_t|}{N_{t,\max}}\right)^{n-1}} \tag{2.12}$$

$$R_{nt}=\frac{v_n}{v_t}=\frac{\left(\frac{N_{t,\max}}{N_{n,\max}}\right)\left(\frac{pq}{n}\right)}{\left[\left(\frac{|N_m|}{N_{m,\max}}\right)^m+\left(\frac{|N_t|}{N_{t,\max}}\right)^n\right]^{\frac{1}{p}-1}}\frac{\left(\frac{|N_n|}{N_{n,\max}}\right)^{q-1}}{\left(\frac{|N_t|}{N_{t,\max}}\right)^{n-1}} \tag{2.13}$$

The final step in establishing the drag anchor trajectory prediction model is to establish the relationship between the anchor cable angle variation and the drag anchor's holding capacity. The formula derived by Neubecker and Randolph (1995) is as follows:

$$\mathrm{T}_a\left(\theta_a^{\,2}-\theta_0^{\,2}\right)=2E_nN_cb\left(S_{u0}+k\frac{Z}{2}\right) \tag{2.14}$$

Taking the derivative of Equation (2.14) with respect to depth, it is rewritten as follows:

$$\frac{d\theta_a}{dz}=\frac{\left(\frac{E_nN_cb}{N_eA_f}-\frac{k\left(\theta_a^{\,2}-\theta_0^{\,2}\right)}{2S_u}\right)}{\left(\theta_a-\theta_0\frac{d\theta_0}{d\theta_a}\right)+\frac{1}{N_e}\frac{dN_e}{d\theta_{as}}\frac{\left(\theta_a^{\,2}-\theta_0^{\,2}\right)}{2}\left(1-\frac{d\theta_s}{d\theta_a}\right)} \tag{2.15}$$

According to Aubeny and Chi (2010), during the dragging process, the bearing factor N_e remains constant, and at the initial stage, the angle of the anchor line from the horizontal at the mudline (θ_0) is 0. Therefore, we can rewrite Equation (2.15) as follows:

$$\frac{d\theta_a}{dz}=\frac{1}{\theta_a}\left(\frac{E_nN_cb}{N_eA_f}-\frac{k\left(\theta_a^{\,2}-\theta_0^{\,2}\right)}{2S_u}\right) \tag{2.16}$$

Equation (2.16) can express the relationship between θ_a and depth variation.

doi:10.6342/NTU202403515

T_a is anchor line tension at shackle point, θ_a is anchor line angle from horizontal at shackle point, θ_0 is angle line from horizontal at mudline, E_n is multiplier to be applied to chain bar diameter, N_c is bearing factor for wire anchor line, b is chain bar or wire diameter, S_{u0} is soil undrained shear strength at mudline, k is soil strength gradient with respect to depth, Z is depth of shackle below mudline.

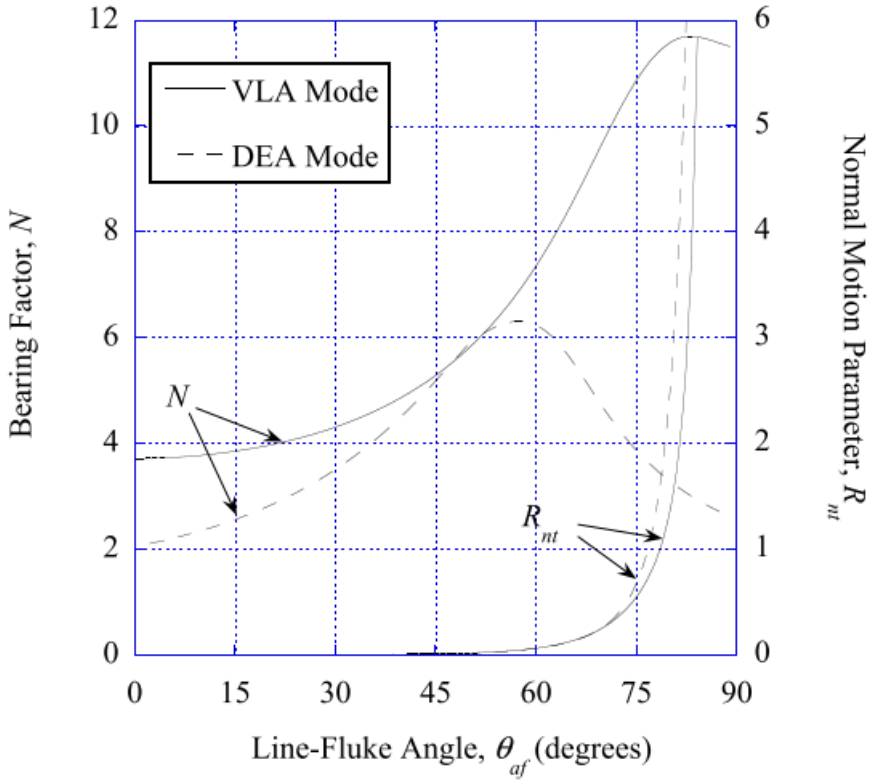

Figure 2. 5 Anchor bearing factor and normal motions (Aubeny & Chi, 2014)

2.2.4 Trajectory Prediction Process

Based on the theoretical equations introduced in the previous sections and referencing the analysis process of the American Bureau of Shipping (2017), the drag anchor's trajectory prediction process can be divided into the following steps:

1. Determining the parameters required during the analysis process, including the dimensions of the DEA, soil parameters, and bearing capacity coefficients.

doi:10.6342/NTU202403515

2. Determining the forward distance parallel to the fluke (Δt) for each iteration of the process and the installation dragging distance ($X_{\max}$).
3. Determining the initial state of the drag anchor, such as the initial burial depth (Z_0), initial anchor line angle to horizontal at shackle point (θ_{a0}), initial fluke angle to horizontal (θ_{f0}).
4. After calculation R_{nt} using Equation (2.13), multiplying R_{nt} by the initially set forward distance Δt provides the forward distance of the vertical fluke (Δn).
5. Calculate the drag anchor's forward distance relative to the seabed horizontally (Δx) and vertically (Δz) using Equation (2.17) and Equation (2.18)

$$\Delta x = \Delta t \cos\theta_f + \Delta n \sin\theta_f \tag{2.17}$$

$$\Delta z = \Delta t \sin\theta_f - \Delta n \cos\theta_f \tag{2.18}$$

6. Multiply the vertical forward distance Δz calculated from Equation (2.18) by Equation (2.16) to obtain the variation value of θ_a, According to the study by Aubeny and Chi (2010), during the dragging process, the rotation of the fluke relative to the shackle is zero. Therefore, the change in θ_f is the negative of the change in θ_a, i.e $d\theta_f = -d\theta_a$.
7. After obtaining the increment for this step, calculate the position of the next step of the drag anchor.
8. Repeat steps 4 to 7 until reaching the installation distance $X_{\max}$ or until θ_f decreases to 0 degrees.

The flowchart of this analysis is shown in Figure 2.6.

doi:10.6342/NTU202403515

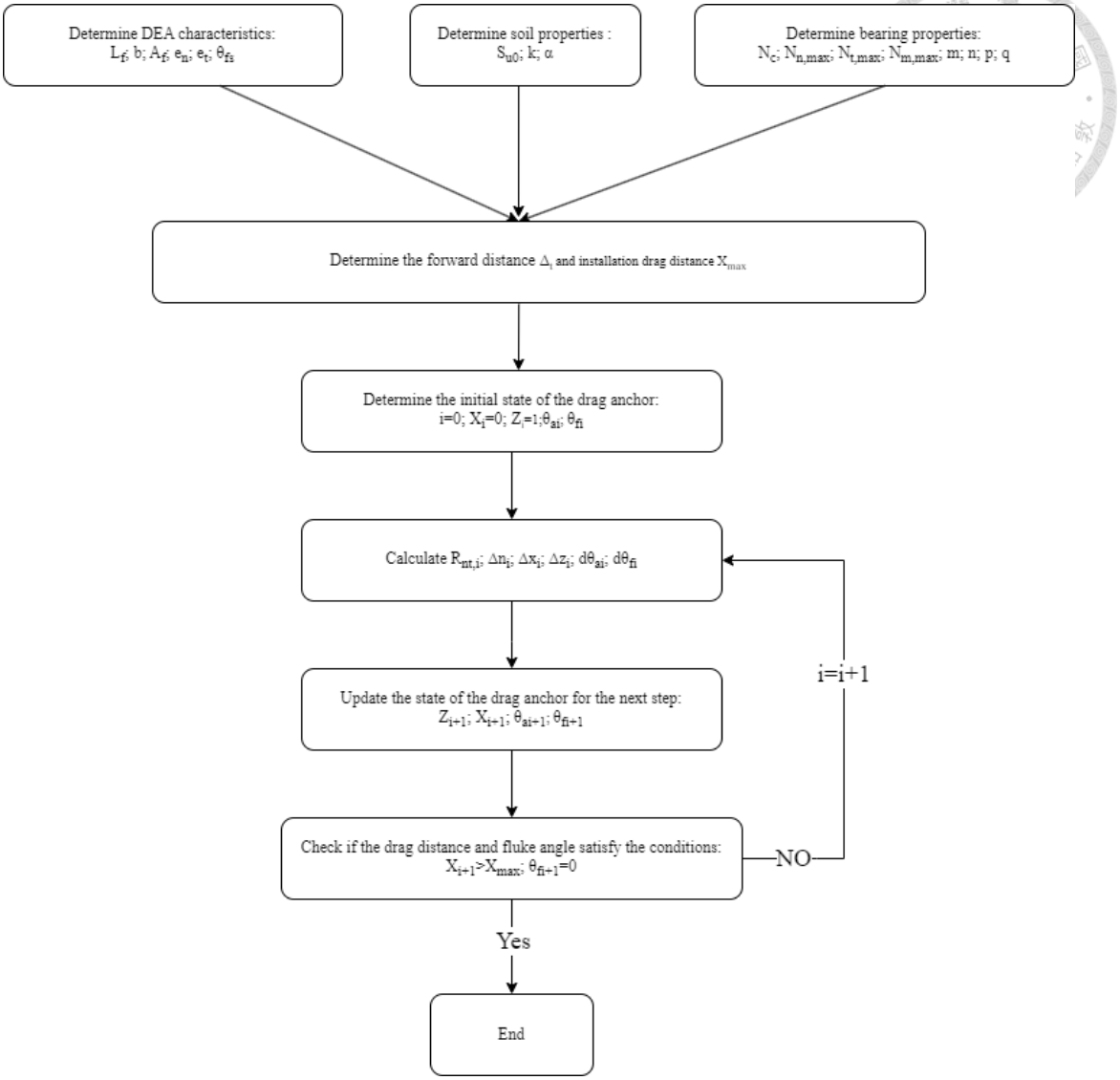

Figure 2. 6 Trajectory prediction process in clay

2.3 Behavior of the Drag Anchor in Sand

Unlike Section 2.1, this section focuses on the behavior of drag anchors in sandy soil. Due to the differing strength characteristics of sand and clay, the behavior of drag anchors when dragged in sand differs from that in clay. There are three methods for studying the drag anchor's trajectory: the limit equilibrium method, the plastic limit method, and the kinematic model. Since the prediction of drag anchor trajectories in sand primarily relies on the kinematic model, which is based on the kinematic behavior of drag

doi:10.6342/NTU202403515

anchors in sand, it cannot provide information on the bearing capacity of the drag anchor. Therefore, this section emphasizes the prediction of drag anchor trajectories.

2.3.1 Movement Direction of Drag Anchor

The movement direction of the drag anchor has a significant impact on trajectory prediction, making it crucial to understand. Liu et al. (2012) provided a clear explanation of movement direction, defining it as the angle between the movement direction of the drag anchor and the top of the fluke when penetrating the soil, shown in Figure 2.7. Perform force equilibrium on the forces acting on the drag anchor according to Figure 2.7, Equation (2.19) is obtained.

$$\mathrm{T}_m + W_m = F_b + F_s \tag{2.19}$$

Where

$$F_b = F_{bs} + F_{bf} = \frac{1}{20}(17K + 3)\gamma z N_q A_b \tag{2.20}$$

$$F_s = F_{ss} + F_{sf} = \frac{1}{20}(3K + 17)\gamma z A_{sm} \tan\delta + K\gamma z A_{sn} \tan\delta \tag{2.21}$$

T_m is component of T_a along the movement direction, W_m is component of W along the movement direction, F_b is total end bearing in the movement direction on the anchor, F_s is total shear force in the movement direction on the anchor, F_{bs}, F_{bf}, F_{ss}, F_{sf} is end bearing in the movement direction on the fluke, shank and shear force in the movement direction on the fluke and shank, K is lateral soil pressure factor, N_q is bearing capacity factors, A_b is effective bearing area of the anchor, which is the total projected area of the anchor on to the plane perpendicular to the movement direction, including the shank and the fluke, A_{sm} is effective shear area of the anchor, including the

doi:10.6342/NTU202403515

fluke and the shank, projected to the primary plane of the fluke, A_{sn} is effective shear area of the anchor, including the fluke and the shank, projected to the plane perpendicular to the primary plane and along the movement direction, δ is angle of interface friction. With reference to Figure 2.7 and Equations 2.19 to 2.21, the tension in the rope at the shackle can be obtained as:

$$T_a = \frac{1}{\cos(\theta_a - \theta_m)}\left[F_b + F_s - W\sin(\theta_0 - \theta_m)\right] \tag{2.22}$$

θ_a is drag angle to the top surface of the fluke at the shackle.

According to Equation 2.22, to determine the tension in the rope, it is necessary to first know the movement direction of the drag anchor. According to Neubecker and Randolph (1995), the minimum work approach proposed can determine the movement direction. If there are many possible movement directions for the anchor, the movement direction that results in penetration is the one where the soil resistance is most easily overcome by the dragging force. In other words, the direction requiring the minimum dragging force to overcome soil resistance is the real movement direction. How to use the minimum work approach to solve for the movement direction, the assumptions, and the process are as follows.

The method for determining the movement direction needs to be used in conjunction with Figure 2.7. Assuming δ_d is a small angular deviation relative to the top surface of the fluke, then the value of the movement direction can only range between $\left[-\delta_{d,}\delta_d\right]$. If δ_d is 0 degrees, it indicates that the movement direction is parallel to the direction of the fluke's top surface, with positive and negative representing clockwise and counterclockwise angular deviations, respectively. If θ is the angle varying between $\left[-\delta_{d,}\delta_d\right]$, then knowing the variation of rope tension with the angle θ allows us to

doi:10.6342/NTU202403515

determine the movement direction. This can be achieved by studying the first derivative of the rope tension, shown in Equation 2.23, The relationship between rope tension and the changing angle θ is expressed in Equation 2.24.

$$\frac{dT_a}{d\theta} = \frac{1}{\cos^2(\theta_a + \theta)} T(\theta) \tag{2.23}$$

$$T_a = \frac{1}{\cos(\theta_{af} + \theta)} [F_b + F_s - W \sin(\theta_0 + \theta)] \tag{2.24}$$

In Equation 2.24, F_b and F_s represent the values of F_b and F_s in the assumed movement direction, calculated as shown in Equation 2.25 and Equation 2.26.

$$\begin{cases} F_b = -A\sin\theta + B\cos\theta + C\sin(\theta_s + \theta) \\ F_s = D\cos\theta - E\sin\theta + F\cos(\theta_s + \theta) + G \end{cases} \quad \text{if } \theta \in [-\delta_d, 0] \tag{2.25}$$

$$\begin{cases} F_b = A\sin\theta + B\cos\theta + C\sin(\theta_s + \theta) \\ F_s = D\cos\theta + E\sin\theta + F\cos(\theta_s + \theta) + G \end{cases} \quad \text{if } \theta \in [0, \delta_d] \tag{2.26}$$

For a rectangular anchor, coefficients A to G are listed in Table 2.2, coefficient K_1, K_2 is shown in Equation 2.27 and Eqution 2.28. For wedge anchors, the coefficients A to G are listed in Liu et al. (2012).

$$K_1 = \frac{1}{20}(17K + 3) \tag{2.27}$$

$$K_2 = \frac{1}{20}(3K + 17)\tan\delta \tag{2.28}$$

To find the minimum value of T_a as it varies within $[-\delta_d, \delta_d]$, we can investigate several specific points, including three types. The first type is points on the boundary, namely $\theta = -\delta_d$ and $\theta = \delta_d$, The second type is where $\frac{dT_a}{d\theta} = 0$, namely points where the first derivative equals zero. The last type is points where the first derivative does not

doi:10.6342/NTU202403515

exist. Based on the derivation above, organize the process to obtain the movement direction:

1. Determine the initial embedment depth Z_0 and the vertical increment distance Δ_n.
2. Determining the soil parameters and the special points that can cause $T_{a,\min}$
3. Using Equation 2.25 and 2.26, calculate the F_b and F_s on the assumed movement direction θ.
4. Substitute the parameters calculated in the first two steps into Equation 2.24 and compare which θ yields the minimum T_a value, the angle cause the smallest T_a is real movement direction in depth Z_i
5. Increase the depth and then repeat steps 2-5 until the assumed vertical penetration depth.

The flowchart of this process is illustrated in Figure 2.8.

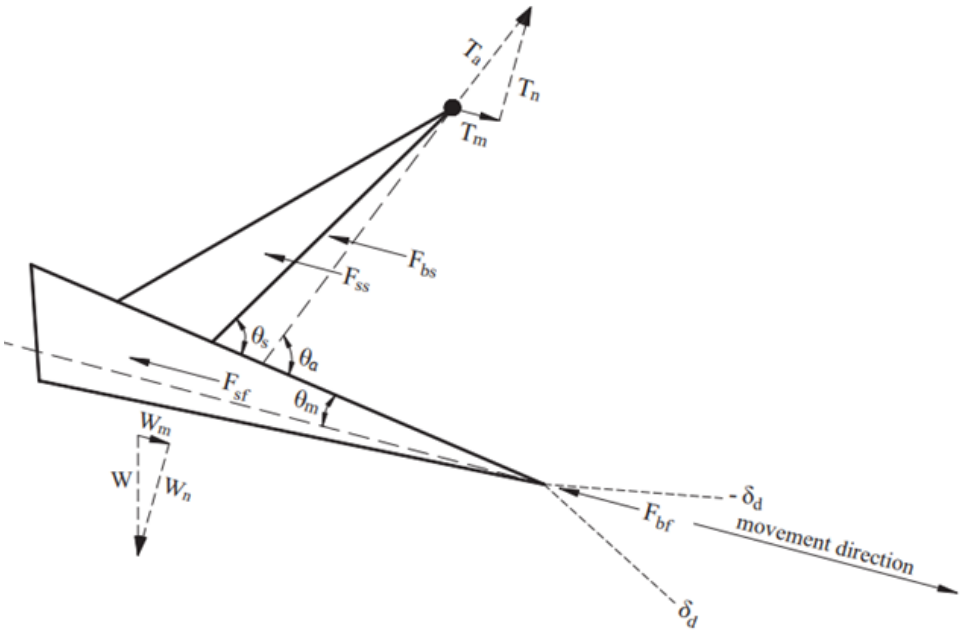

Figure 2. 7 Definition of movement direction (Liu et al., 2012)

doi:10.6342/NTU202403515

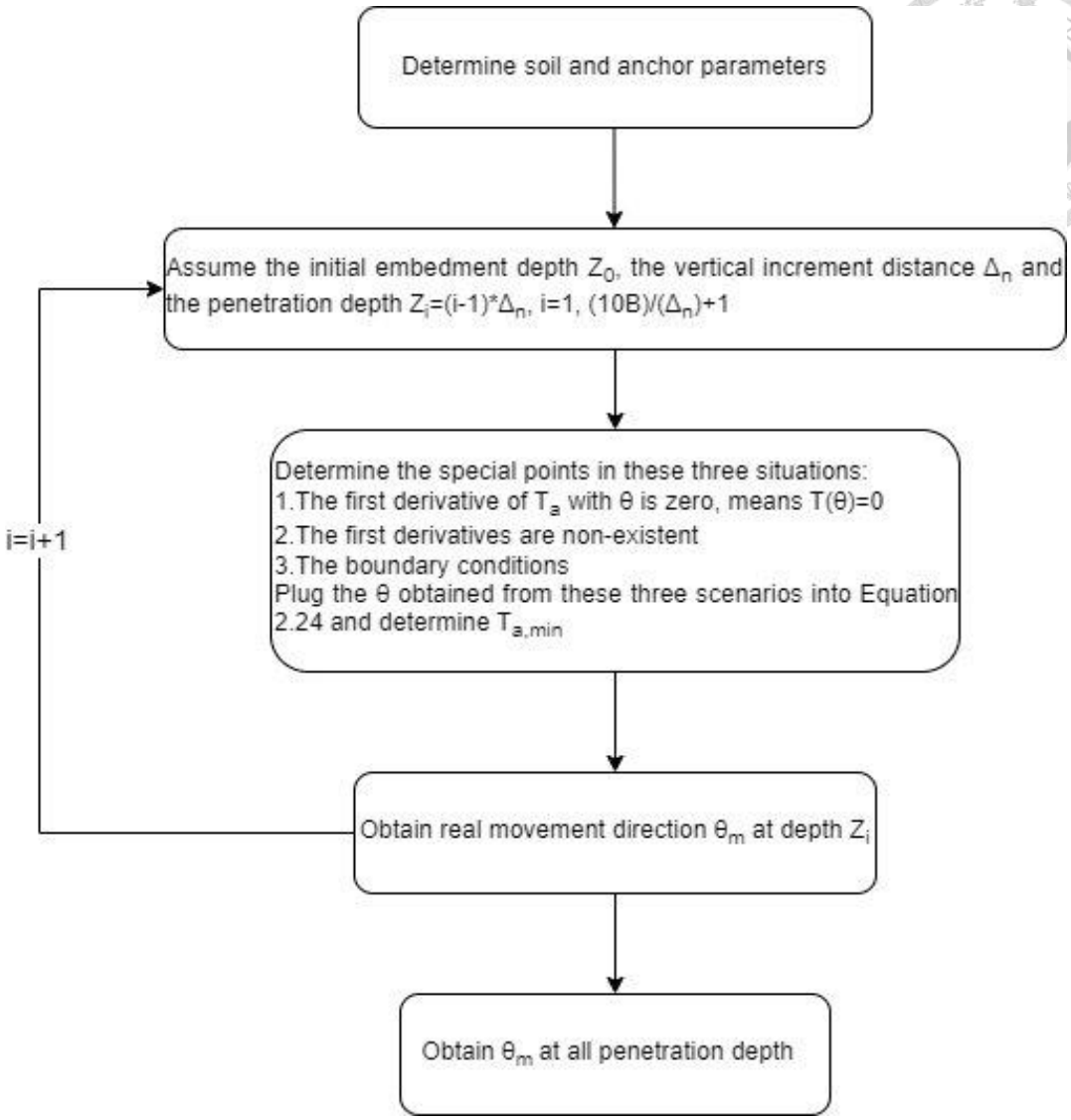

Figure 2. 8 The process flowchart for determining the movement direction.

doi:10.6342/NTU202403515

Table 2.3 Coefficient A to G Sources: (Liu et al., 2012)

Rectangular Anchor		
Coefficient	Clay	Sand
A	$N_c S_u A_{top}$	$K_1 \gamma Z_a N_q A_{top}$
B	$N_c S_u A_n$	$K_1 \gamma Z_a N_q A_n$
C	$N_c S_u A_{bs}$	$K_1 \gamma Z_a N_q A_{bs}$
D	$2\alpha S_u A_{top}$	$2K_2 \gamma Z_a A_{top}$
E	$\alpha S_u A_n$	$K_2 \gamma Z_a A_n$
F	$\alpha S_u A_{sms}$	$K_2 \gamma Z_a A_{sms}$
G	$\alpha S_u A_{sn}$	$K \gamma Z_a A_{sn} \tan\delta$

A_{top} is area of the top surface of the fluke, A_n equal to $width \times thickness$, projected area to the plane perpendicular to the movement direction of the rectangular anchor, A_{bs} is effective bearing area of the shank, A_{sms} is effective shear area of the shank projected to the primary plane of the fluke.

2.3.2 Prediction of Drag Anchor Trajectory

Peng and Liu (2019) and Peng et al. (2021) proposed a set of trajectory prediction equations for predicting the trajectory of drag anchors in sand. Similar to Section 2.2.1, this prediction model is built on the minimum work approach. However, unlike the previous section, this section discusses motion behaviors not only involving diving but also including pulling out and keying. Diving refers to the movement of the anchor along the movement direction of the fluke, pulling out refers to the movement direction perpendicular to the fluke orientation, and keying refers to the rotational motion around the anchor's rotation center, Diving and pulling out are translational motions and do not

doi:10.6342/NTU202403515

involve any rotation, the schematic diagrams for these three motions are shown in Figure 2.9.

Although Peng and Liu (2019) and Peng et al. (2021) proposed a set of drag trajectory formulas applicable to sandy soil, there are some unclear aspects in the literature. For example, in Peng and Liu(2019), it is mentioned that the drag anchor in sand may undergo not only diving but also pulling out and keying. Although the text describes how to determine the current motion state of the anchor, it does not specify the motion increments of the anchor when the latter two motion states occur. Additionally, in Peng et al.(2021), there are differences in the prediction procedure compared to Peng and Liu(2019). In Peng and Liu (2019), the method for determining the actual motion state of the anchor is inferred based on the previous step's state. However, in Peng et al.(2021), the angle change of the anchor is fixed at $\frac{\theta_s}{300}$. Finally, although experiments were conducted to validate the model, the authors believe that the scale of the experiments was too small. While the experimental results may appear to predict well, they only demonstrate good prediction results in the initial stages. As the drag distance increases, based on the predictive trend, the error is expected to increase significantly, shown in Figure 2.10

Taking into account the above points, as there is currently no reliable process for predicting the trajectory of drag anchors in sand, this paper does not develop new trajectory prediction for sand in this study.

doi:10.6342/NTU202403515

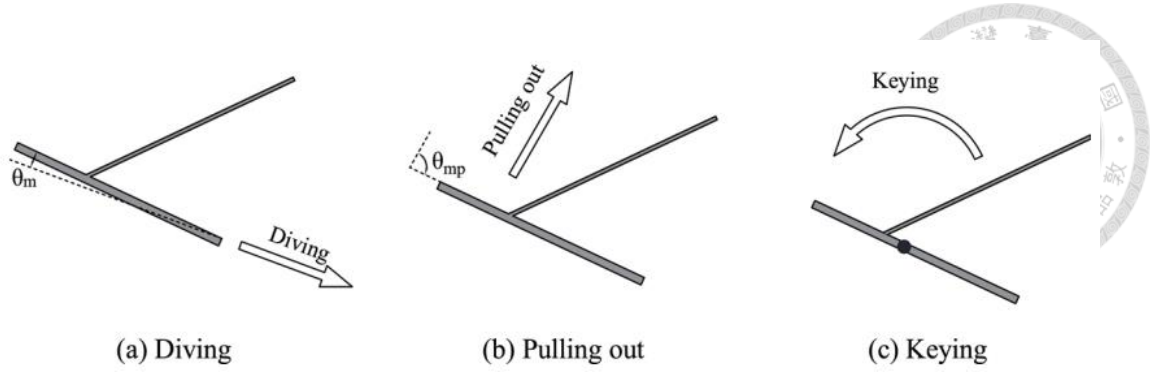

Figure 2. 9 The three motion behaviors of the drag anchor (Peng & Liu, 2019)

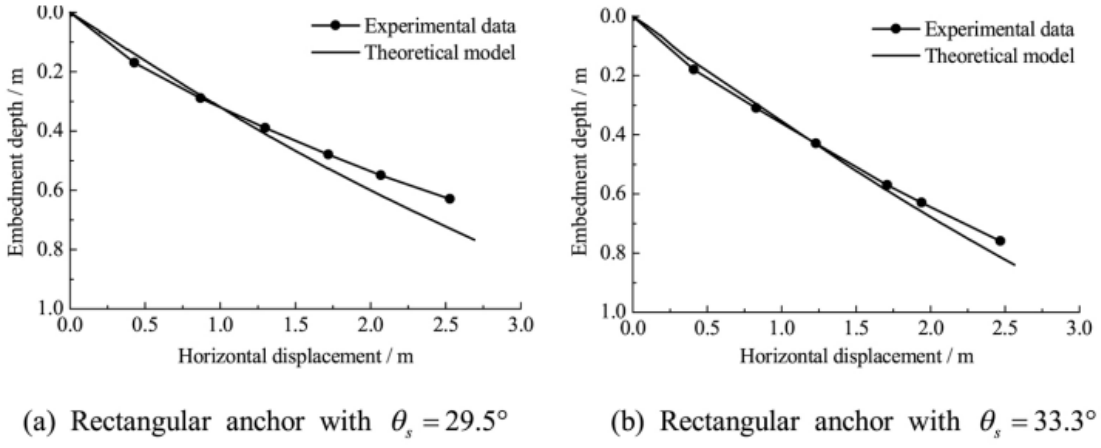

Figure 2. 10 Comparison of Experimental Data with Predictive Theory in sand (Peng & Liu, 2019)

2.4 Cyclic Softening of clay

2.4.1 Calculation of Clay Strength Degradation Without Ground Response Analysis

Under cyclic loading, saturated clay experiences excess pore water pressure buildup, leading to a decrease in soil stiffness and strength, When the number of cycles N=1, the shear modulus is at its maximum value, indicating the maximum shear resistance. As the number of cycles continues to increase, the shear modulus will decrease continuously. as shown in Figure 2.11. Tsai et al. (2014) proposed a simplified method to assess the

doi:10.6342/NTU202403515

strength degradation of saturated clay under cyclic loading. Unlike commonly used liquefaction analysis procedures based on stress methods, the process uses a strain-based approach to estimate the relationship between cyclic softening and strength reduction.

According to Tsai et al.(2014), the extent of strength reduction is related to both the OCR and PI values, where OCR affects the fitted parameters s and r, while the PI value affects the $G/G_{\max}$ curve, as shown in Figure 2.12. When clay undergoes cyclic softening, its softening behavior includes both stiffness degradation and strength reduction. For clay, the modulus degradation index δ_c is the same as the stress softening index δ_τ, as shown in Equation 2.29.

$$\delta_c = \delta_\tau = N_c^{-s(\gamma-\gamma_t)^r} \tag{2.29}$$

The parameter γ_t represents the threshold strain. If the current shear strain exceeds this threshold value, cyclic softening occurs in the clay. The evaluation method is carried out as follows:

1. Finding the earthquake magnitude M_w and maximum ground acceleration PGA
2. Calculate the shear modulus $G_{\max}$ at N=1 using Equation 2.30.

$$\mathrm{G}_{\max} = \rho \times V_s^{\,2} \tag{2.30}$$

3. After obtaining the shear modulus, use Equation 2.31 along with Figure 2.13 to find the corresponding shear strains for each layer.

$$\gamma_{eff}\left(\frac{G_{eff}}{G_{\max}}\right) = 0.65 \times \left(\frac{a_{\max}}{g \times G_{\max}}\right)\sigma_v \times r_d \tag{2.31}$$

4. Using Equation 2.34 to obtain the equivalent number of loading cycles N_c, where the fixed parameters in the equation are shown in Table 2.5. Parameter b

doi:10.6342/NTU202403515

is set to 1, and the calculation methods for T_s and S_1 are as shown in Equation 2.32 and 2.33,

$$T_s = \frac{4Z}{V_s} \tag{2.32}$$

$$S_1 = \frac{S_a(1)}{S_a(0.2)} \tag{2.33}$$

$$\ln N_c = \ln\left[\frac{\exp\left(c_0 + c_1 \ln PGA + c_2 \ln S_1 + c_3 M_w + c_4 \ln b + c_5 b T_s\right) + 0.5}{0.65^{\frac{1}{b}}}\right] \tag{2.34}$$

where S_1 is the spectral ratio between 1.0s spectrum acceleration $S_a(1.0)$ and 0.2 s spectrum acceleration $S_a(0.2)$.

5. Finally, use Equation 2.29 for calculation, where the values of s and r can be obtained from Table 2.3, and the value of γ_t is 0.03%.

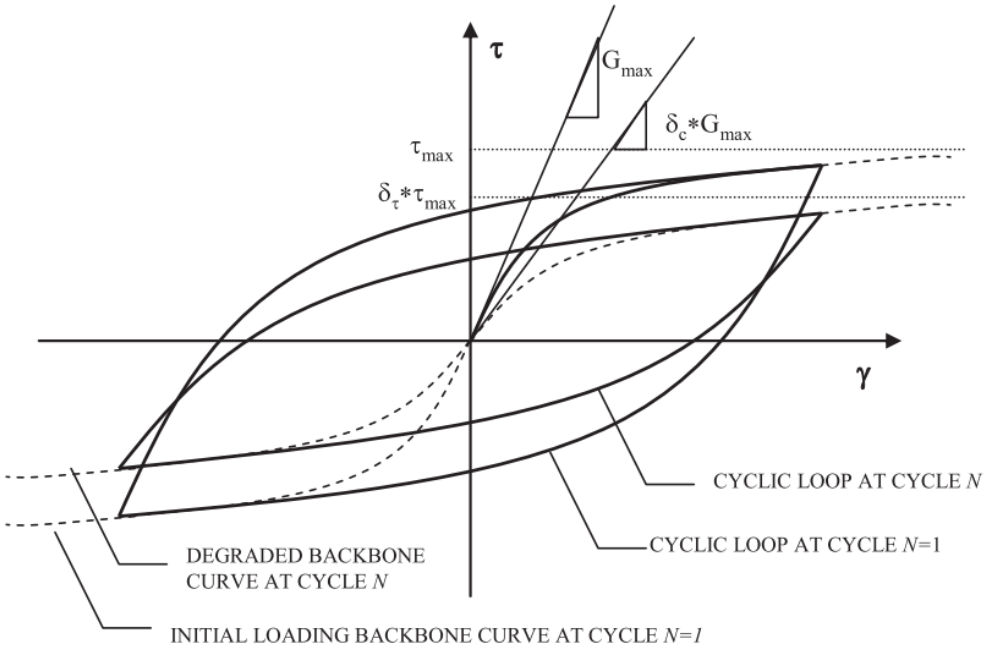

Figure 2. 11 Cyclic loading leads to a decrease in stiffness (Tsai et al., 2014)

doi:10.6342/NTU202403515

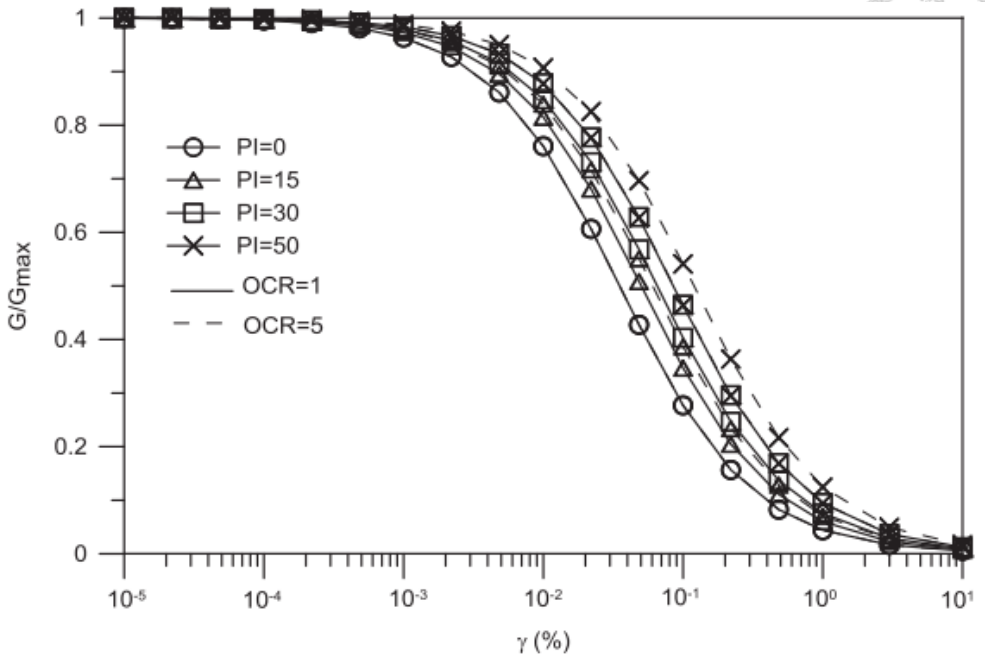

Figure 2. 12 Modulus reduction curve (Tsai et al., 2014)

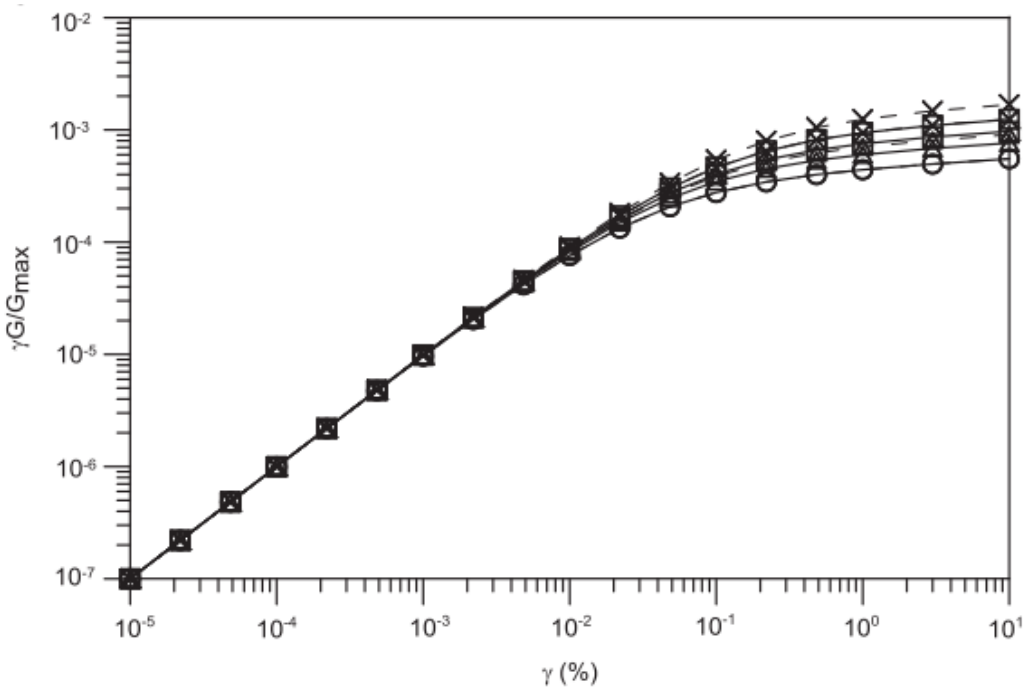

Figure 2. 13 Shear modulus reduction curve with increasing shear strain (Tsai et al., 2014)

doi:10.6342/NTU202403515

Table 2.4 The relation ship between OCR and parameters s and r

OCR	s	r
1	0.075	0.495
1.4	0.064	0.520
2	0.054	0.480
4	0.042	0.423

Sources: (Tsai et al., 2014)

Table 2.5 Converting seismic force irregular amplitude to laboratory equivalent amplitude coefficient.

c_0	-3.43	c_4	1.72
c_1	-0.352	c_5	-1.50
c_2	-0.402	b	1
c_3	0.798		

Sources: (Tsai et al., 2014)

2.4.2 Calculation of Clay Strength Degradation Based on Ground Response Analysis

The method in Section 2.4.1 is based on the calculation approach used when ground response analysis is not performed. As mentioned in Tsai et al. (2014), if ground response analysis is conducted, steps 2 through 4 mentioned in Section 2.4.1 can be skipped, and the N_c and γ values required for equation 2.29 can be obtained directly using the results from the ground response analysis. Kishida and Tsai (2014) proposed a method

doi:10.6342/NTU202403515

for converting irregular seismic waves into equivalent cycles for laboratory testing. The calculation formula is shown in Equation 2.35

$$N_c = \frac{1}{2}\sum_{i=1}^{m}\left(\frac{K_i}{K_{ref}}\right)^{1/b} \quad (2.35)$$

where K_i = peak amplitude of the seismic coefficient for each half-cycle and K_{ref} =reference seismic coefficient. The calculation method for K_{ref} is shown in Equation 2.36. Tsai et al. (2014) mentioned that in Kishida and Tsai (2014), the model was initially derived for b values between 0.05 and 0.5. To verify whether the model could be extended to b = 1, Tsai et al. (2014) compared the ln(Nc) values calculated using Equation 2.35 with those calculated using Equation 2.34 for b values ranging from 0.1 to 1. The results showed that the model proposed by Kishida and Tsai (2014) can indeed be extended to b = 1. Additionally, since the b value used in Section 2.4.1 is 1, to compare the difference in softening indices calculated with and without ground response analysis, the b value in Equation 2.35 will also be set to 1.

$$K_{ref} = r_e K_{\max} \quad (2.36)$$

where 0.65 is selected as the value of r_e.

After obtaining the N_c and γ values using this method, they can be substituted into Equation 2.29 to calculate the clay's strength degradation.

doi:10.6342/NTU202403515

2.5 Numerical Modeling

2.5.1 Drag Anchor Model

Qiao et al. (2020) proposed a numerical model for simulating the bearing capacity of drag anchors. Shown in Figure 2.14. To reduce boundary effects, a 10 times fluke length was adopted as the model width and length. Detailed discussions on the dimensions of the ABAQUS model will be provided in Chapter 3. The material of the anchor is steel, with a Poisson's ratio of 0.3 and a Young's modulus of 2.1×10^{11} Pa.

According Qiao et al.(2020); Zhao and Liu (2014); The elastic-plastic model obeying the Von-Mises yield criterion is adopted, so the yield stress in Mohr-Coulomb model can be calculated using the $\sqrt{3}S_u$, the soil is assumed to be undrained, therefore the Poisson's ratio is 0.49. Additionally, in the proposed model, Coulomb friction contact is employed, and the calculation of shear stress τ between two contact surfaces is as shown in Equation 2.37, in which σ is the normal contact pressure, μ is friction coefficient, the value of μ is varies in range (0.1, 0.3).

$$\tau = \mu\sigma \tag{2.37}$$

In Figure 2.14, as shown, in the numerical simulation, the bearing capacity moves a distance Δt along the tangent direction. In Qiao et al.(2020), Δt is assumed to be 1 meters, the relationship between holding capacity and displacement after dragging completion is depicted in Figure 2.15. After dragging completion, the last point on the curve is considered as the holding capacity for the current tangential displacement. For Qiao et al. (2020) comparing with Ruinen (2004) field test, the numerical model result is 958.02 kN/m, which differs by 4.9% from the field test result of 913.7 kN/m, demonstrating the feasibility of this numerical model.

doi:10.6342/NTU202403515

Furthermore, Qiao et al. (2020) observed in the curve of holding capacity versus displacement at a burial depth of 10m that the curve can be divided into three parts. Firstly, as the penetration displacement increases, the holding capacity exhibits a linear increase. This indicates that the soil surrounding the anchor is in the stage of elastic deformation, without undergoing plastic deformation. Secondly, the holding capacity shows a nonlinear increase. At this point, the soil surrounding the anchor undergoes plastic deformation. Lastly, as the penetration distance continues to increase, the holding capacity tends to stabilize, indicating that the soil surrounding the anchor reaches its limit state. At this point, the holding capacity represents the ultimate holding capacity at that burial depth, the discussion regarding this segment needs to be accompanied by Figure 2.16.

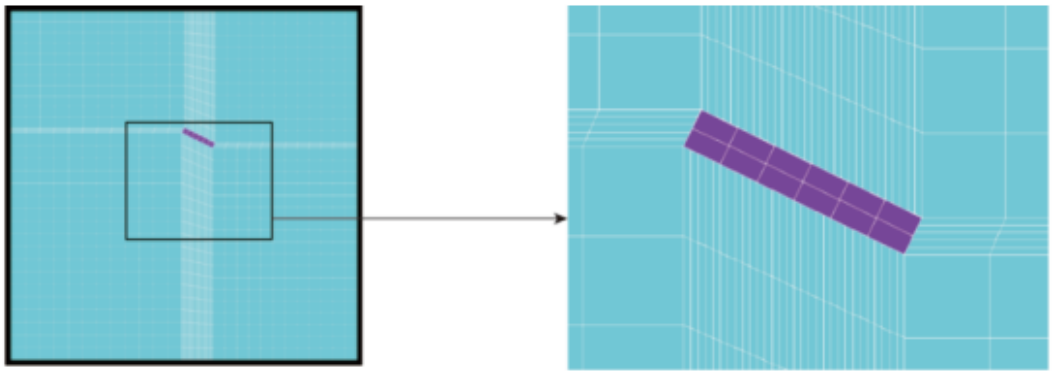

Figure 2. 14 Numerical model schematic of drag anchor (Qiao et al., 2020)

doi:10.6342/NTU202403515

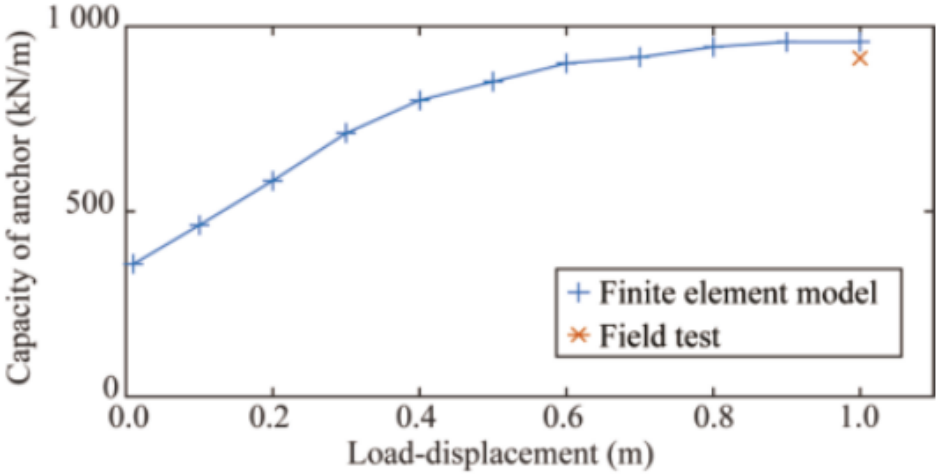

Figure 2. 15 Holding capacity versus displacement for model validation (Qiao et al., 2020)

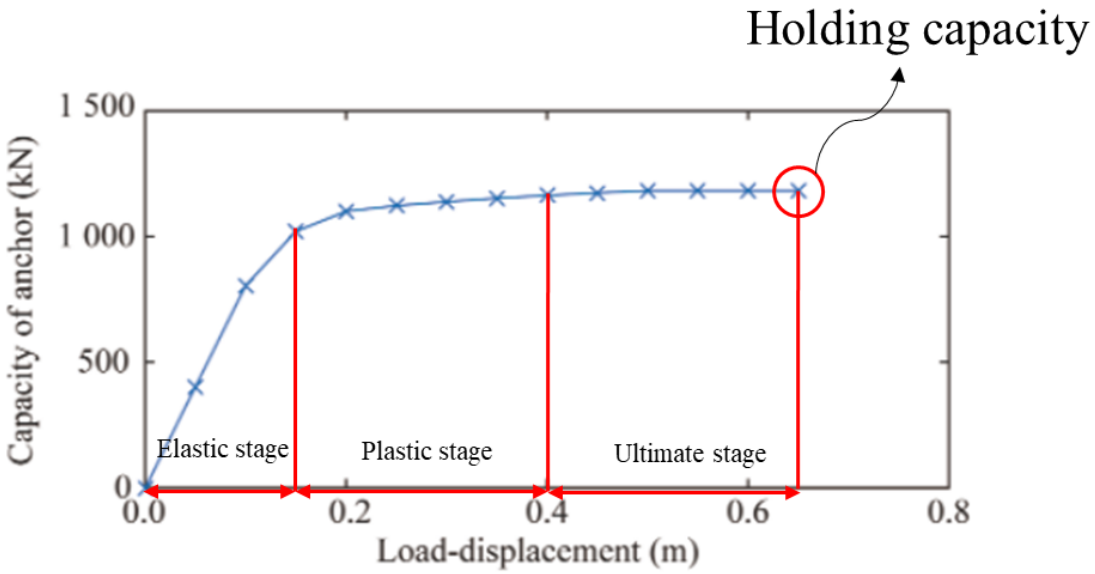

Figure 2. 16 Holding capacity versus displacement depth=10m (Qiao et al., 2020)

2.5.2 SNKH Model

Considering the seismic response of structures in cohesive soils and their susceptibility to damage, it is necessary to understand the post-seismic response of structures on the seabed. Mucciacciaro and Sica (2018); Zhang et al.(2021); Soleimanian et al. (2023) employed the kinematic hardening constitutive soil model to simulate the

doi:10.6342/NTU202403515

nonlinear behavior of soils. This section will provide a detailed introduction to this constitutive soil model.

This model is a modification of the Von Mises failure criterion, incorporating isotropic and kinematic hardening, the evolution of the yield surface in stress space is related to two components: isotropic hardening component and kinematic hardening component. For the isotropic hardening component, this component controls the size of the yield surface σ^0 based on the plastic strain $\bar{\varepsilon}^{pl}$, while for the kinematic hardening component, it describes the translation of the yield surface. The isotropic hardening component is represented by Equation 2.38,

$$\sigma^0 = \sigma\big|_0 + Q_\infty \left(1 - e^{-b\bar{\varepsilon}^{pl}}\right) \tag{2.38}$$

where $\sigma\big|_0$ is stress at zero plastic strain, Q_∞ and b respectively define the maximum variation size of the yield surface and the rate at which this yield surface changes with plastic strain. If $Q_\infty = 0$, it indicates that the size of the yield surface remains unchanged, representing $\sigma^0 = \sigma\big|_0$, and the model simplifies to a pure kinematic hardening model. For the kinematic hardening component, its expression is given by Equation 2.39,

$$\dot{\alpha} = C\frac{1}{\sigma^0}(\sigma - \alpha)\dot{\bar{\varepsilon}}^{pl} - \gamma_{kh}\alpha\dot{\bar{\varepsilon}}^{pl} \tag{2.39}$$

where α is backstress, C represents the initial kinematic hardening modulus, and C equals Young's modulus, γ_{kh} is an internal parameter determines the rate of hardening decrease with plastic strain accumulation.

Anastasopoulos et al. (2011) proposed simple correlations to define the main parameters of this constitutive model, such as: the maximum yield stress σ_y, which defines the size of the yield surface, The parameter γ_{kh} controls the kinematic hardening

doi:10.6342/NTU202403515

of the soil. The conversion formulas for these two parameters are shown in Equations 2.40 and 2.41,

$$\sigma_y = \frac{\sigma|_0}{\lambda} \tag{2.40}$$

$$\gamma_{kh} = \frac{C}{(\sigma_y - \sigma|_0)} \tag{2.41}$$

where the empirical value of λ is 0.1-0.3.

Because seismic forces involve rapid loading, and the Von Mises failure criterion can be applied to undrained conditions of clay, the undrained shear strength S_u can be defined using $\sigma_y = \sqrt{3}S_u$. After completing the parameter calculations, Mucciacciaro and Sica (2018); Zhang et al.(2021); Soleimanian et al. (2023) all successfully simulated the nonlinear behavior of soil by fitting a target shear modulus reduction curve using this constitutive model, as shown in Figure 2.17 and Figure 2.18.

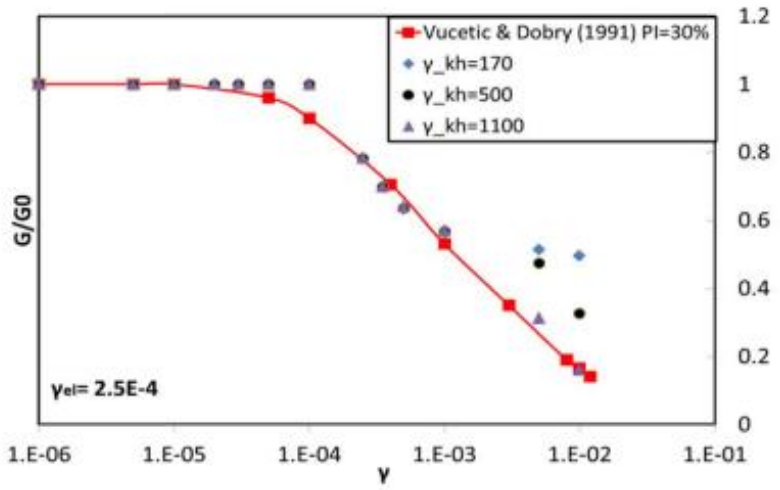

Figure 2. 17 Validation of shear modulus reduction curve the nonlinear kinematic hardening model (Mucciacciaro and Sica, 2018)

doi:10.6342/NTU202403515

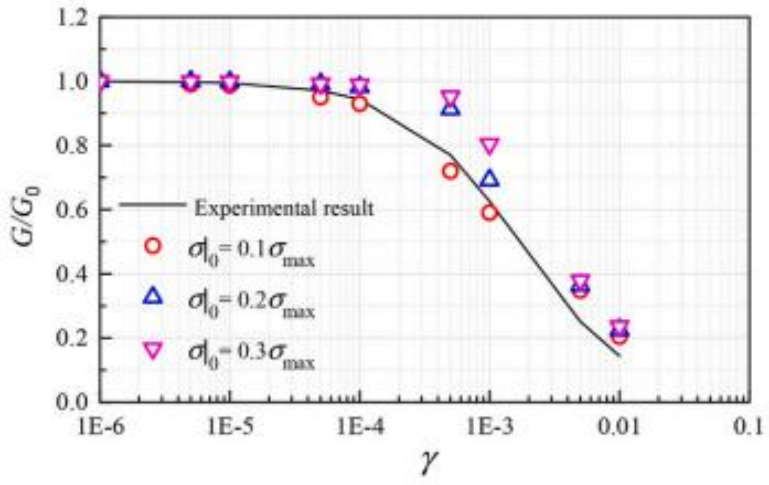

Figure 2. 18 Validation of shear modulus reduction curve the nonlinear kinematic hardening model (Zhang et al., 2021)

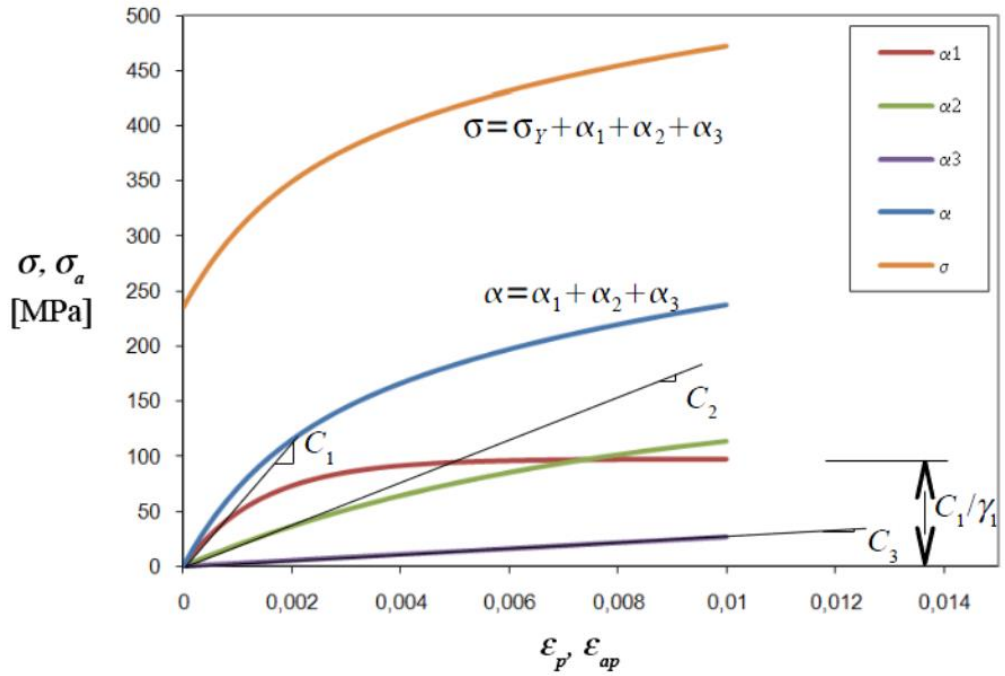

Figure 2. 19 The relationship between backstress and the target stress-strain curve (Halama et al., 2012)

doi:10.6342/NTU202403515

Chapter 3 Methodology

3.1 Trajectory Prediction

3.1.1 Prediction in Clay

According to the literature review in Section 2.1, a predictive model was reconstructed based on the procedure outlined by the American Bureau of Shipping(2017). The parameters used are shown in Table 3.1, the increment of tangential displacement Δt is assumed 0.2m. The comparison between the predictive results of the reconstructed model and those of the American Bureau of Shipping (2017) is shown in Figure 3.1-3.3. The results indicate that the accuracy of the reconstructed model is good. Therefore, the predictive model will be used for the trajectory prediction of drag anchors in clay in the future.

This study employs the soil parameters from borehole BH04 data in the western offshore of Taiwan for numerical simulations. Due to the softness of the soil in the surface layer of the seabed, the measured shear wave velocity is too low. This low wave velocity can lead to excessively high deformation velocities in dynamic analyses, and it can also significantly reduce the Peak Ground Acceleration (PGA), resulting in less obvious strength degradation of the soil. Therefore, to investigate the cyclic softening behavior of clay, we selected the parameters from the fourth layer of soil in BH04 for analysis. Before constructing the numerical simulation, it is necessary to know the state of the anchor in the soil layers. The soil parameters from this borehole are shown in Table 3.2, and the predicted results are illustrated in Figure 3.4-3.6. Based on the soil parameters in Table 3.2, two scenarios were predicted: one using the mean undrained shear strength for prediction (k=0), and the other assuming that the undrained shear strength changes with

doi:10.6342/NTU202403515

depth at a rate of 1.5 kN/m (k=1.5). The predicted results are shown in Figures 3.4 to 3.6. For k=0 and k=1.5, the ultimate depths are 7.4m and 7.73m, respectively, with a fluke angle of 3.61 degrees in both cases. The holding capacities are 16,628 kN and 18,531 kN, respectively. Since the prediction of holding capacity is related to undrained shear strength, as per Equation 2.8, the holding capacity remains constant at k=0 and increases with depth at k=1.5.

It should be noted that the dimensions of the anchor (length, width, and height) used for prediction with the BH04 borehole are different from those of the ABS anchor. Detailed explanations of the anchor parameters used with the BH04 borehole are provided in Section 3.3.1.

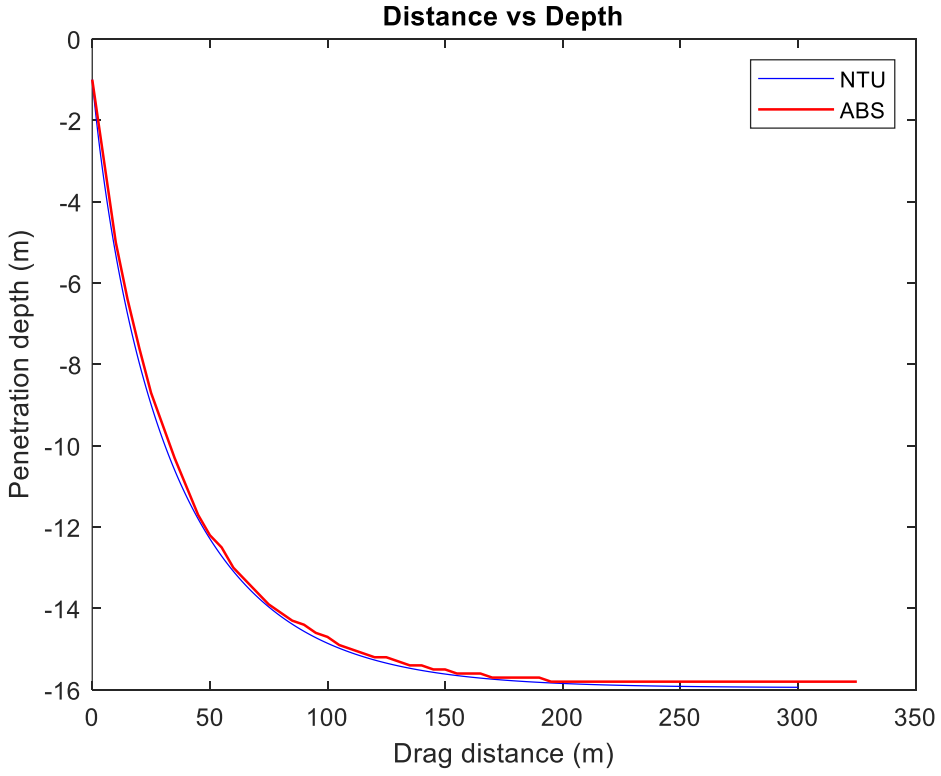

Figure 3. 1 Embedment depth vs drag distance (ABS)

doi:10.6342/NTU202403515

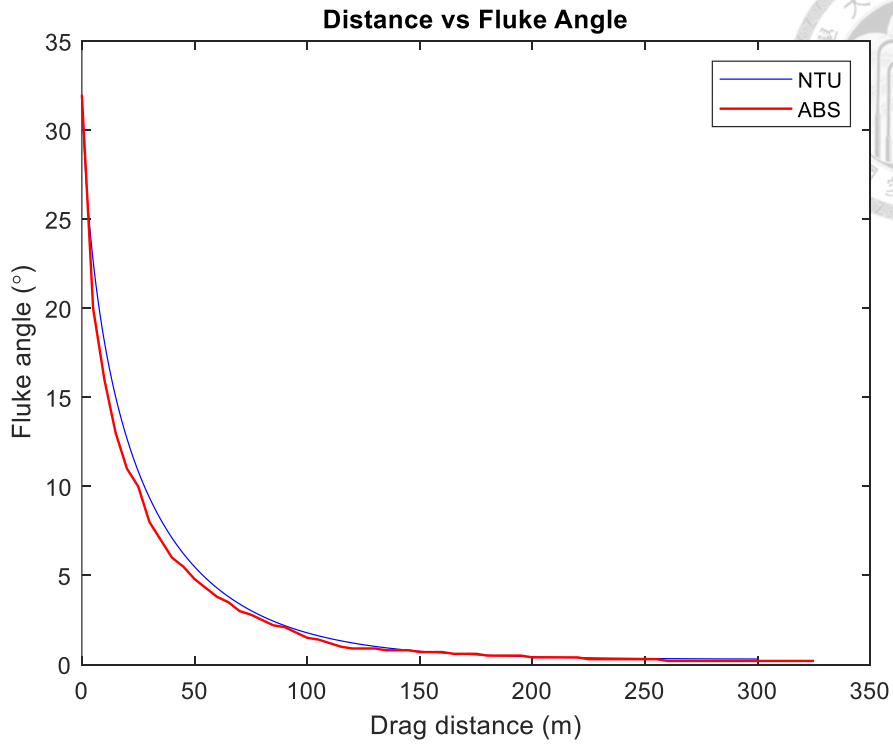

Figure 3. 2 Embedment depth vs fluke angle (ABS)

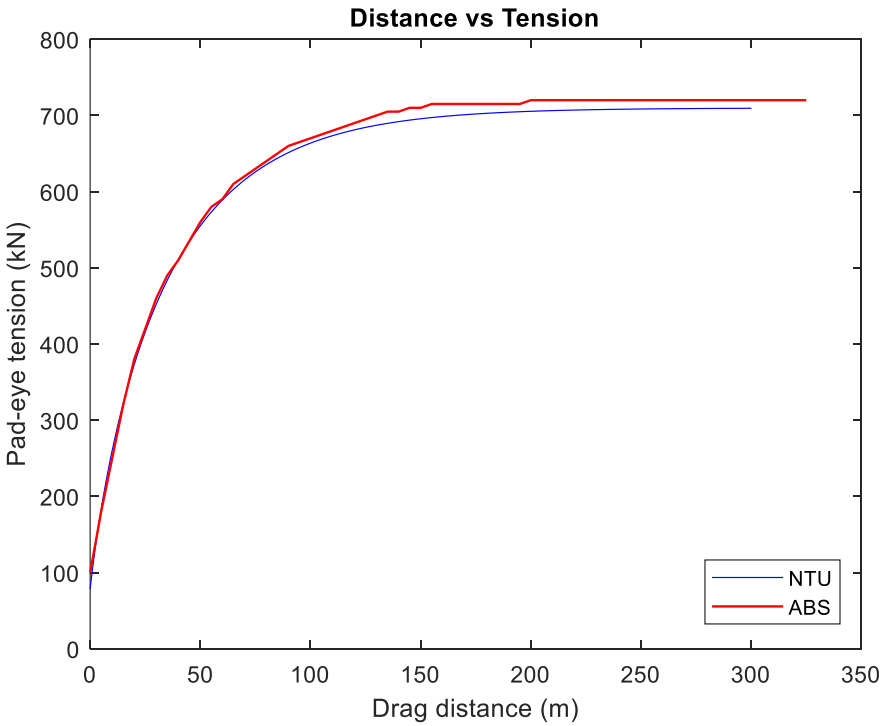

Figure 3. 3 Embedment depth vs pad-eye tension (ABS)

doi:10.6342/NTU202403515

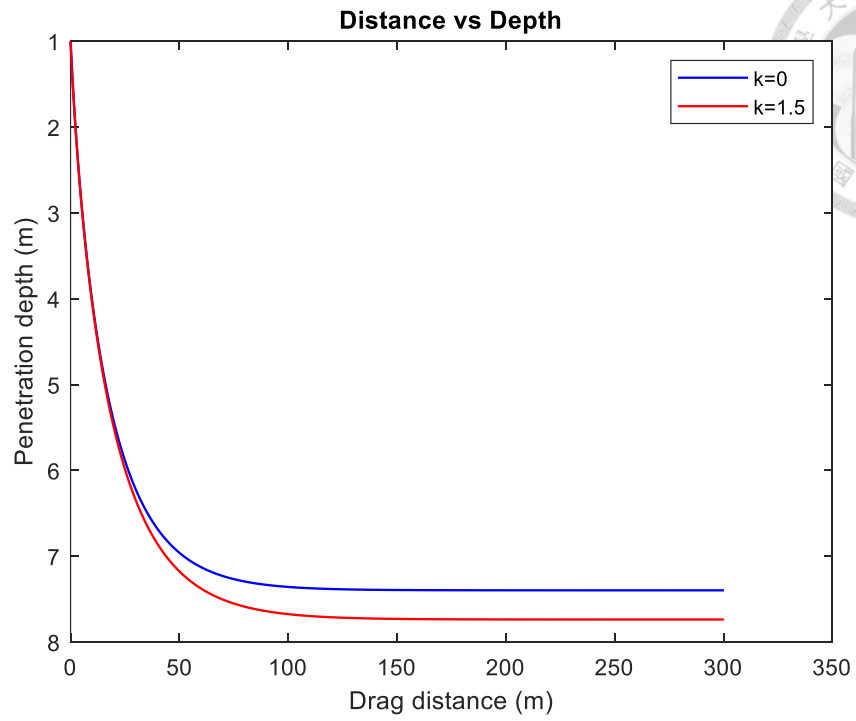

Figure 3. 4 Embedment depth vs drag distance (BH04)

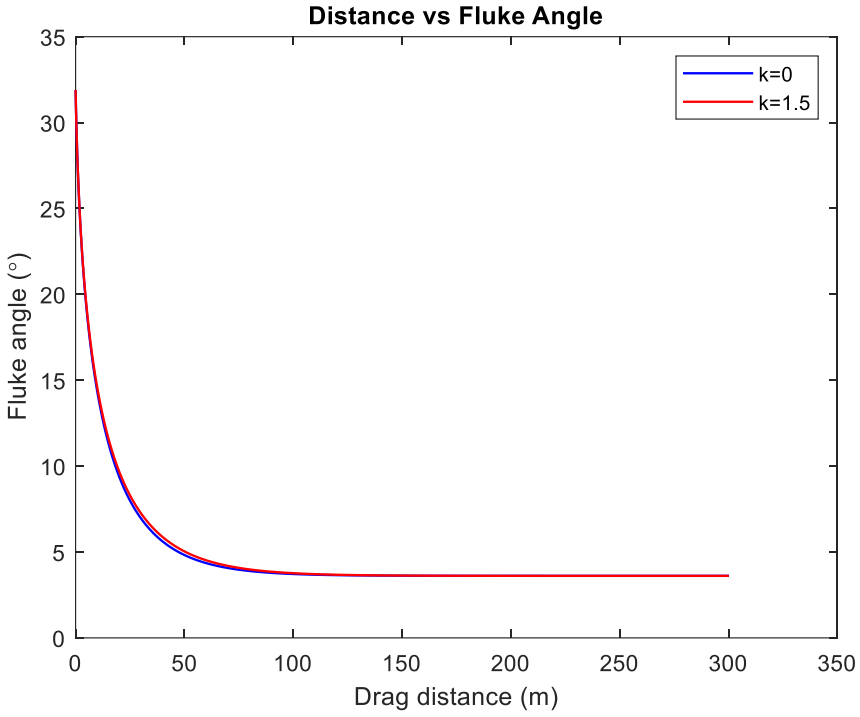

Figure 3. 5 Embedment depth vs fluke angle (BH04)

doi:10.6342/NTU202403515

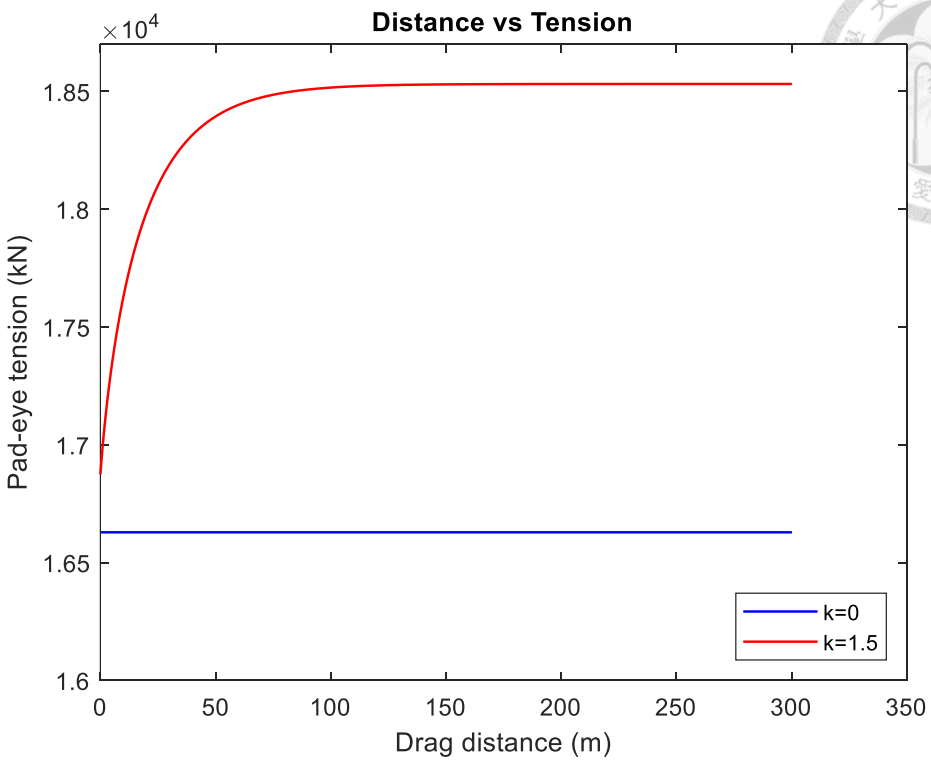

Figure 3. 6 Embedment depth vs pad-eye tension (BH04)

doi:10.6342/NTU202403515

Table 3.1 Parameters for drag anchor trajectory prediction

Category	Parameter	Symbol	Units	Value
Anchor/chain	Fluke area	A_f	m^2	6
	Fluke length	L	m	2
	Fluke thickness	T	m	0.3
	Line diameter	b	m	0.073
	Fluke-shank angle	θ_{fs}	◦	45
	Chain multiplier	E_n	---	1
Bearing factor	Line bearing factor	N_c	---	12
	Tangential bearing factor	$N_{t,\max}$	---	2.9
	Normal bearing factor	$N_{n,\max}$	---	11.6
	Moment bearing factor	$N_{m,\max}$	---	1.6
Combined loading interaction coefficient	Interaction coefficient	m	---	1.56
	Interaction coefficient	n	---	4.19
	Interaction coefficient	p	---	1.57
	Interaction coefficient	q	---	4.43
Soil	Mudline strength	S_{u0}	kPa	1.5
	Strength gradient	k	kPa/m	1.75
	Adhesion factor	α	---	0.3
Initial condition	Initial embedment	Z_0	m	1
	Initial position	X_0	m	0
	Installation mudline angle	θ_0	◦	0

doi:10.6342/NTU202403515

Table 3.2 BH04 drilling soil parameters

Depth	S_u (kPa)	Submerge unit weight (kN/m^3)	V_s (m/s)	G (MPa)	E (MPa)	ν
0~12m	6.9~145.8 (45.1)	4.8	88.6	13	33.9	0.3038
12~19.6m	33.5~353.7 (97.5)	7.3	162.8	47.9	124.6	0.3006
19.6~24.9m	67.4~447.6 (244.2)	7	184.6	59.3	154.3	0.3010
24.9~27.7m	36.2~356.1 (101.4)	7.6	189.6	66.1	171.8	0.2995

Sources: (Taiwan Power Company, 2018)

3.2 Numerical Simulations on Drag Embedment Anchor

3.2.1 Dynamic Explicit Analysis

The ABAQUS/Explicit module in ABAQUS applies central difference integration rule to perform explicit time integration of the motion equations, computing the dynamic conditions of the next incremental step using the dynamic conditions of the previous step. As the drag anchor is embedded in the soil and dragged within it, the dragging process involves highly discontinuous contact. ABAQUS/Explicit adopts an explicit time integration scheme, which, compared to the implicit method, enhances convergence during analysis of nonlinear problems such as interface contact by eliminating the need for iterative computations. The workflow of the dynamic explicit analysis method is as follows:

1. Dynamic equilibrium equations

doi:10.6342/NTU202403515

$$M\ddot{u}=P-I \tag{3.1}$$

2. Calculate the acceleration at the start of the current increment.

$$\ddot{u}\Big|_{(t)} = \left(M\right)^{-1} \cdot \left(P-I\right)\Big|_{(t)} \tag{3.2}$$

3. Explicit time integration over time

$$\dot{u}_{(t+\frac{\Delta t}{2})} = \dot{u}_{(t-\frac{\Delta t}{2})} + \frac{(\Delta t_{(t+\Delta t)} + \Delta t_{(t)}}{2}\ddot{u} \tag{3.3}$$

$$u_{(t+\Delta t)} = u_{(t)} + \Delta t_{(t+\Delta t)}\dot{u}_{(t+\frac{\Delta t}{2})} \tag{3.4}$$

4. Based on strain rate $\dot{\varepsilon}$, calculate the element strain increment $\Delta\varepsilon$.

5. Calculate the stress σ based on the material constitutive law

$$\sigma_{(t+\Delta t)} = f(\sigma_{(t)}, \Delta\varepsilon) \tag{3.5}$$

6. Internal nodal forces $I_{(t+\Delta t)}$

7. Set time t increase to $t+\Delta t$, Return to step two

Due to the significant contact discontinuities and large deformations present in the numerical model established in this study, non-convergence issues may occur when using implicit analysis. As explicit analysis only requires the current known state to solve for future states without iteration, the ABAQUS/Explicit solver was chosen for simulations in this study.

doi:10.6342/NTU202403515

3.2.2 Anchor's True and Simplified Models

This section introduces the anchor models that will be used in the subsequent simulations. The True Model uses the MK6 model from STEVPRIS company, while the Simplified Model is obtained by equivalent projection area of the MK6 model, and the equivalent process will be demonstrated in this section.

Since American Bureau of Shipping (2017) mentions that the shank's influence is not considered during the analysis process, in our numerical model, we will only include the fluke. Therefore, the simulation results will be more conservative. After obtaining the projection area of the anchor, dividing it by the true fluke length of the MK6 model will give the length and width of the simplified model. As shown in Figures 3.8 to 3.11, after obtaining a projected area of $23m^2$, dividing $23m^2$ by the fluke length of 4.52 m yields an equivalent fluke width of 5.08 m. Figure 3.11 represents the simplified anchor model used in the half analysis, so the width is only 2.54 m, the above models will be used in conjunction with the soil parameters from the BH04 borehole for prediction and simulation. Regarding the ABS case numerical simulation, the model dimensions of the anchor will be based on the parameters mentioned in Table 3.1.

doi:10.6342/NTU202403515

Figure 3. 7 STEVPRIS MK6 anchor (STEVPRIS Company)

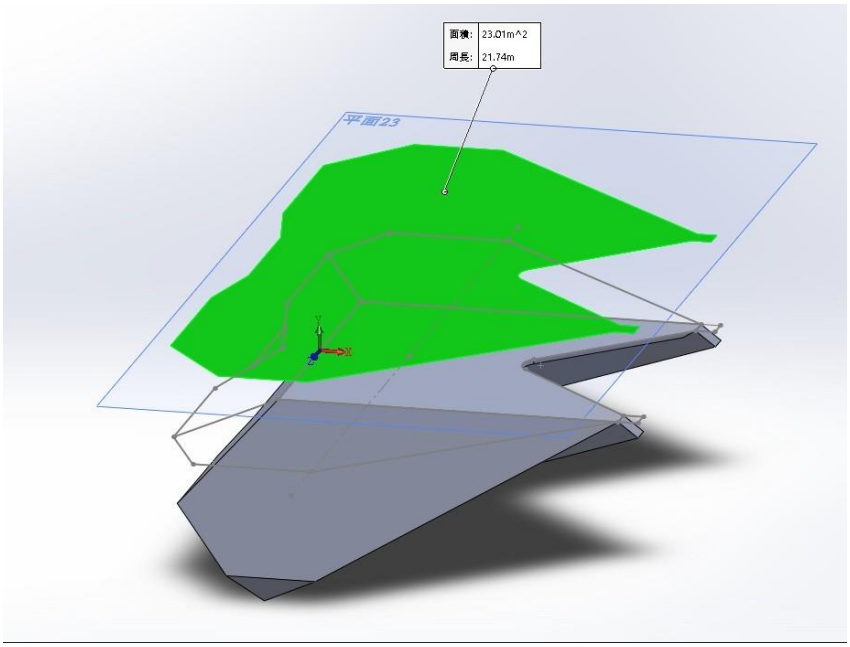

Figure 3. 8 The projection area of the MK6 model

doi:10.6342/NTU202403515

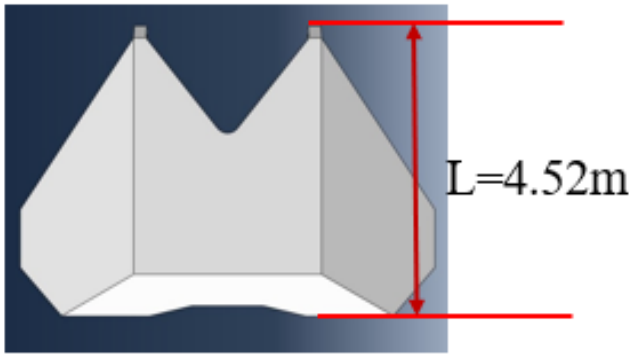

Figure 3. 9 The fluke length of the MK6 model

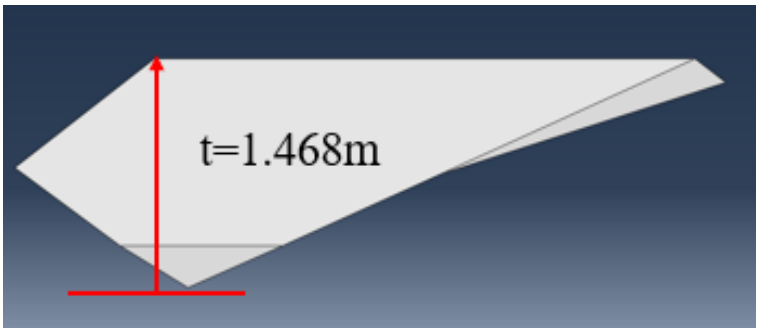

Figure 3. 10 The thickness of the MK6 model

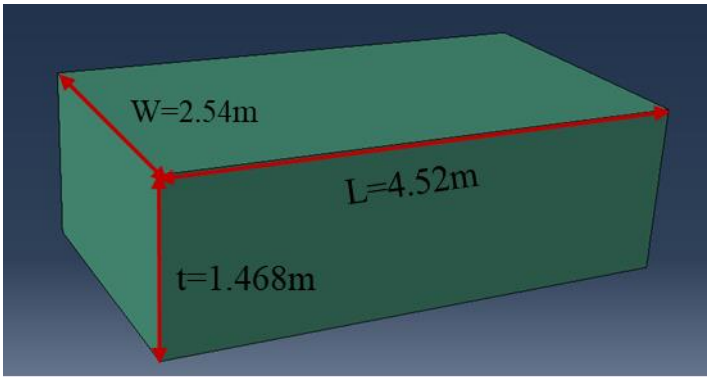

Figure 3. 11 The length and width of the half simplified model

doi:10.6342/NTU202403515

3.2.3 Model Size

To reduce the influence of boundary size on simulation results, different model sizes were used in this section, and the differences in holding capacity during simulation were compared. We set the model sizes to be 3 times, 5 times, 8 times, and 10 times the length and width of the anchor, with a depth of 30 meters, model is shown in Figure 3.12, the hole in the middle represents the position of the anchor in the soil. The soil and the anchor are two separate parts.

Using the soil parameters from BH04 for model size testing, the predicted results are shown in Section 3.1.1. The results of the model size testing are depicted in Figures 3.13 to 3.15. The results indicate that when the burial depth is deep, the results from a model size of 3 times differ from those of other sizes, but the results from sizes larger than 5 times tend to converge. However, Qiao et al.(2020) used a model size of 10 times the fluke length in their numerical simulations of drag anchor behavior. For safety reasons, this study follows the same approach as Qiao et al. (2020) and selects a size 10 times larger for the model. Therefore, the final model dimensions are determined to be 50m*25m*30m.

doi:10.6342/NTU202403515

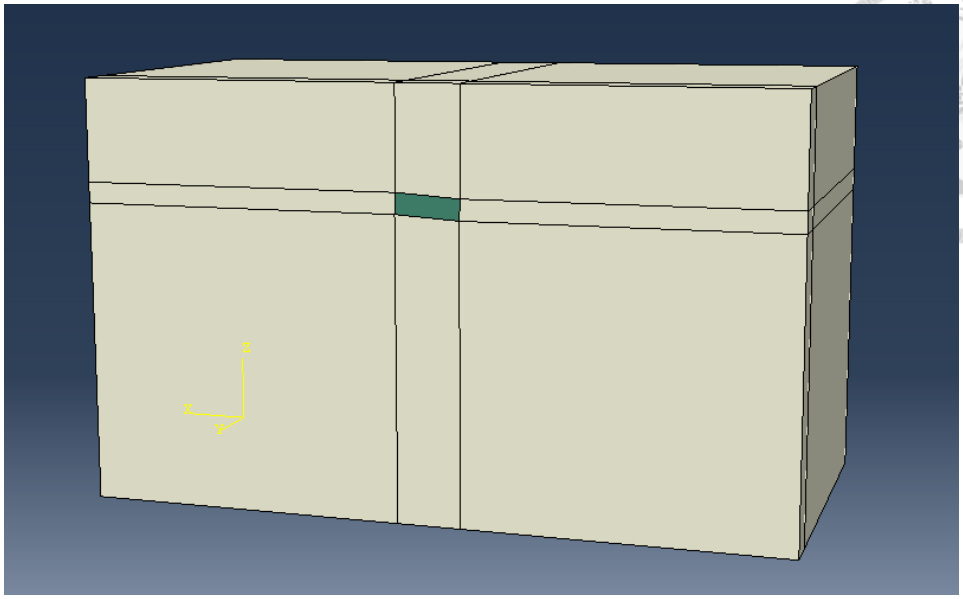

Figure 3. 12 schematic diagram of the model with dimensions 10 times the length and width of the anchor

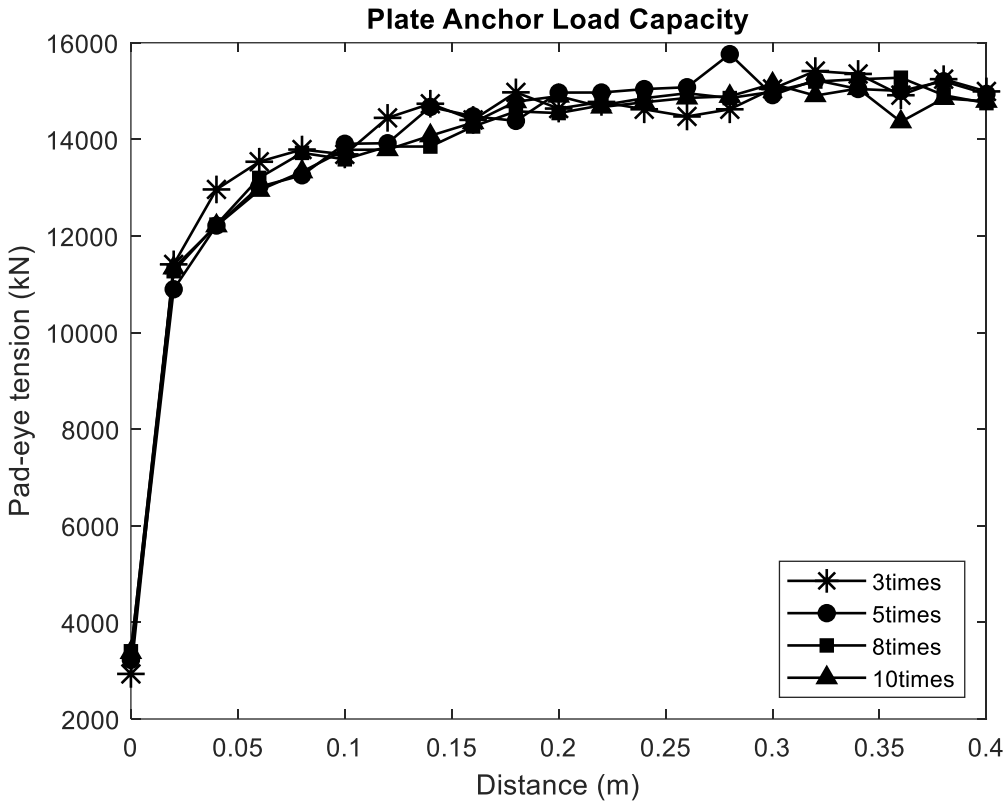

Figure 3. 13 Model size testing with a burial depth of 2 meters

doi:10.6342/NTU202403515

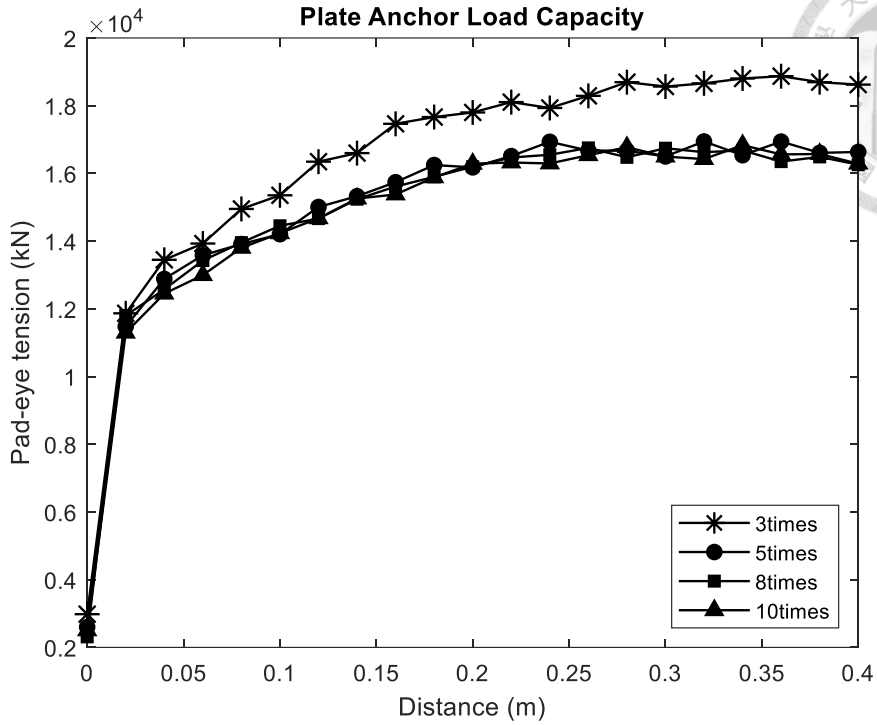

Figure 3. 14 Model size testing with a burial depth of 5 meters

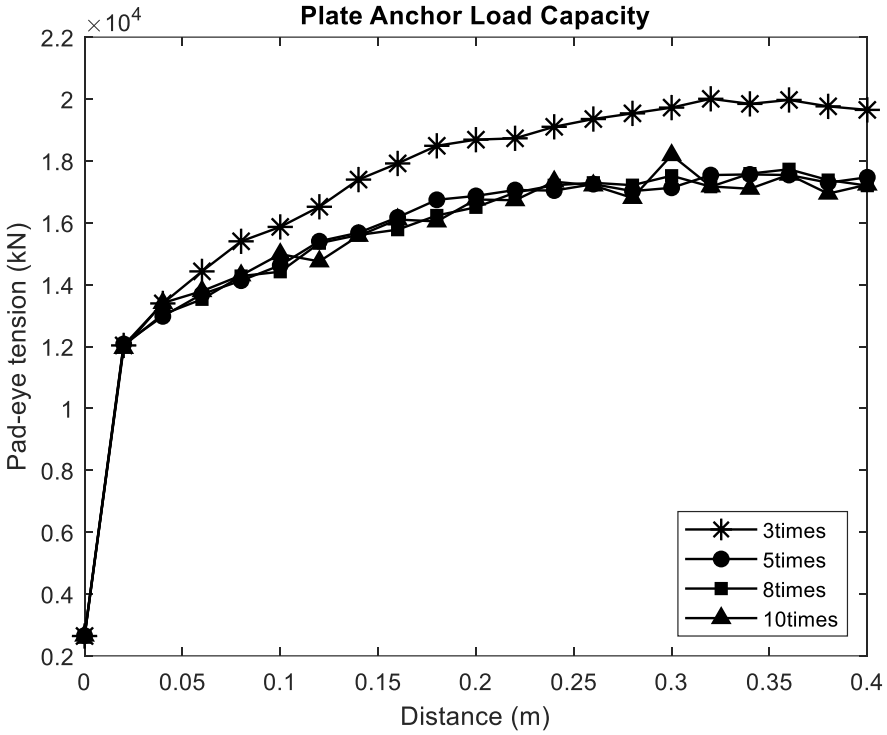

Figure 3. 15 Model size testing with a burial depth of 7.4 meters

doi:10.6342/NTU202403515

3.2.4 Material

This section will introduce the material settings in the numerical model, including the anchor, clay, and sand. The material for the anchor is steel, while both clay and sand are simulated using the Mohr-Coulomb failure criterion.

In the drag anchor analysis, the clay is considered to be saturated and undrained, hence the friction angle is set to 0 degrees. The Poisson's ratio is defined as 0.49, and the Mohr-Coulomb model is degenerated to the Tresca model, resulting in $\sigma_y = \sqrt{3}S_u$. For the sand, a small cohesion value 6kPa needs to be set in the model to stabilize the numerical simulation. Failure to set this value may lead to convergence difficulties. All other parameters are set according to the existing data. In the simulation, the clay material uses the soil parameters of BH04 fourth layer soil and the parameters of American Bureau of Shipping (2017). For the material setup according to the American Bureau of Shipping(2017), soil parameters are assigned for each meter of soil depth. Since the undrained shear strength varies with depth, the undrained shear strength is taken as the value at the midpoint of each soil layer. The details of these soil parameter settings are listed in Table 3.3. while the sand material parameters are listed in Table 3.5.

For the anchor, steel material properties are used, including only the unit weight and elastic properties, with no plastic properties set. The parameters are shown in Table 3.6.

doi:10.6342/NTU202403515

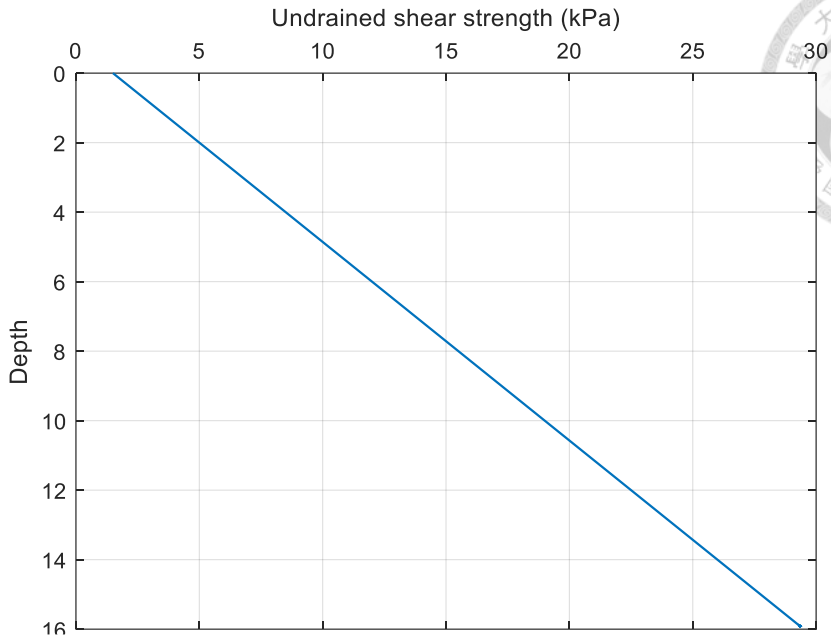

Figure 3. 16 Undrained shear strength increase linearly

Table 3.3 The parameters of clay using in ABAQUS

Depth (m)	Density (kg/m^3)	S_u (kPa)	Yield stress (Pa)	E (Pa)
0~1	1600	2.375	4113.62067	1187500
1~2	1600	4.125	7144.70958	2062500
2~3	1600	5.875	10175.7985	2937500
3~4	1600	7.625	13206.8874	3812500
4~5	1600	9.375	16237.9763	4687500
5~6	1600	11.125	19269.0652	5562500
6~7	1600	12.875	22300.1541	6437500
7~8	1600	14.625	25331.2431	7312500
8~9	1600	16.375	28362.332	8187500
9~10	1600	18.125	31393.4209	9062500
10~11	1600	19.875	34424.5098	9937500

doi:10.6342/NTU202403515

Table 3.4 The parameters of clay using in ABAQUS (BH04 fourth layer soil)

Depth (m)	Density (kg/m^3)	S_u (kPa)	Yield stress (kPa)	E (MPa)	V_s (m/s)	G (MPa)
0~30m	1775.33	101.4	175.456	171.8	189.6	66.1

Table 3.5 The parameters of sand using in ABAQUS (BH04) Sources: Taiwan Power Company (2018)

Soil description	Relative density (%)	Friction angle (°)	Submerge unit weight (kN/m^3)
Loose sand	40.5	30	9
V_s (m/s)	G (MPa)	E (MPa)	ν
258.5	129.4	336.5	0.3002

Table 3.6 The parameters of steel

Material	Unit weight (kg/m^3)	E (MPa)	ν
Steel	7850	2.1×10^5	0.3

3.2.5 Contact Property

Since the soil and anchor are two separate parts, there is an interface contact between them. We use a "penalty" method to simulate the tangential behavior at the interface. According to the American Bureau of Shipping (2017), the holding capacity of the drag anchor mainly comes from the soil resistance encountered by the front end of the anchor when penetrating the soil. The influence of friction on the holding capacity is minimal. Therefore, a friction coefficient of 0.1 is chosen for the interface between the soil and anchor. For the normal behavior between contact surfaces, we use hard contact definition,

doi:10.6342/NTU202403515

which means there is no contact force generated when the two contact surfaces separate. If the contact surfaces come into contact again, contact forces will be generated at that instant. Therefore, when the contact condition changes from separation to contact, there will be a sharp change in contact forces, as shown in Figure 3.17.

According to the American Bureau of Shipping (2017), the analysis process is not consider the influence by shank. Therefore, in the numerical model, we will extract the contact force on the fluke to represent the holding capacity, as shown in Figure 3.18. Since the rope tension is a two-dimensional force, we will only extract the contact force in the advance direction and take the resultant force as the holding capacity. As shown in Figure 3.18, the anchor's advancement direction is a combination of the x and z directions. Therefore, when outputting the contact force, we only need to output the contact forces in these two directions and calculate the resultant force.

After outputting the data and calculating the holding capacity, Using the "movemean" command in MATLAB for data smoothing, after processing, a curve like Figure 3.19 will be obtained, where the blue line represents the raw data and the orange line represents the smoothed result. Calculate the slope of the smoothed curve. When the slope of the smoothed curve drops below 0.1, average the unsmoothed data points from that time point forward to obtain the holding capacity.

doi:10.6342/NTU202403515

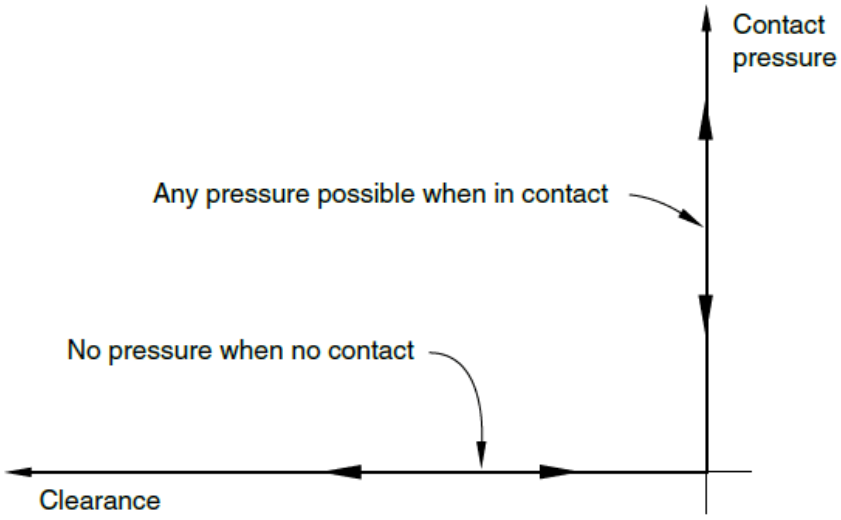

Figure 3. 17 Hard contact property (ABAQUS, 2022)

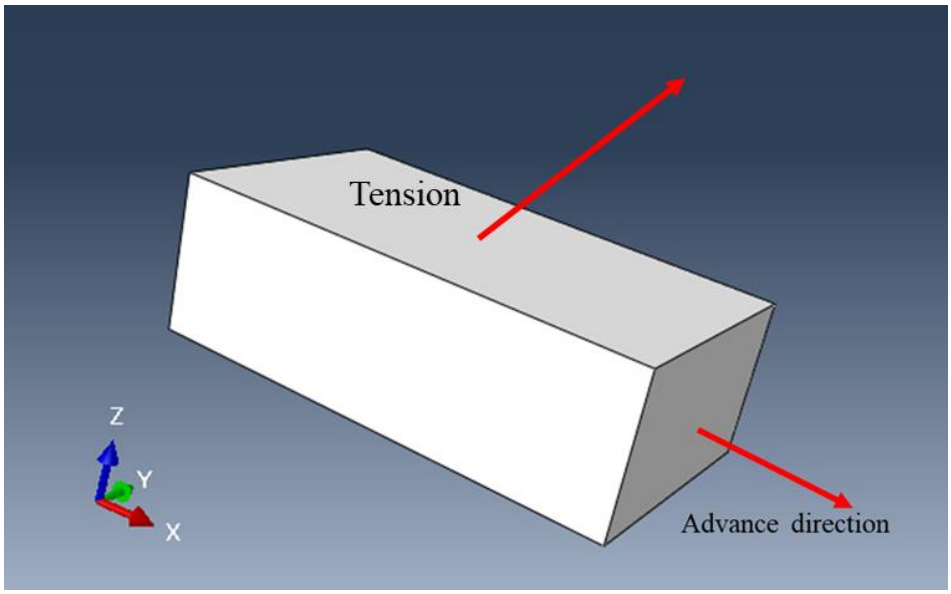

Figure 3. 18 The advancement direction of the drag anchor

doi:10.6342/NTU202403515

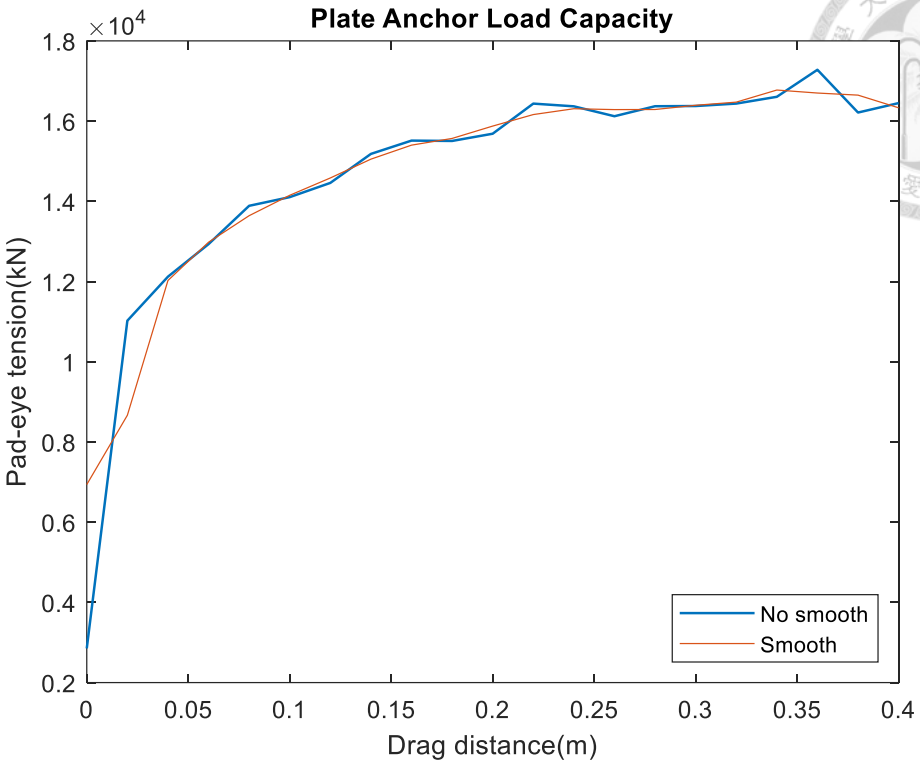

Figure 3. 19 Raw data and smoothed data

3.2.6 Boundary Conditions and loads

In terms of boundary conditions, to prevent the soil from collapsing sideways due to gravity, we fix the vertical direction of the model surfaces, as shown in Figure 3.20 to Figure 3.22. For the anchor part, displacement control is used to move the anchor along the tangent direction by a specified distance. According to the review in Section 2.4.1, to achieve the steady-state stage of bearing capacity, the anchor needs to be pulled forward until the soil reaches its limit state. Therefore, the soil strength will affect the distance of this pulling. If the soil strength is stronger, the anchor needs to be pulled a longer distance, and vice versa. One thing to note is that if the forward distance is changed, the iteration forward distance in our prediction procedure must also be adjusted accordingly. Figures 3.25 to 3.27 demonstrate the impact of changing the iteration distance on the prediction results, indicating that there is no difference in the predicted results between 0.2m and

doi:10.6342/NTU202403515

1m. In addition, regardless of the dragging distance setting, the dragging speed is set to 0.1 m/sec. As shown in Figure 3.24, the anchor is embedded in the soil with a specified penetration distance controlled by displacement.

For the loading conditions, a gravity of 9.81 m/sec² is applied to the entire model, and a uniform load is used at the top to simulate water pressure, as shown in Figures 2.23.

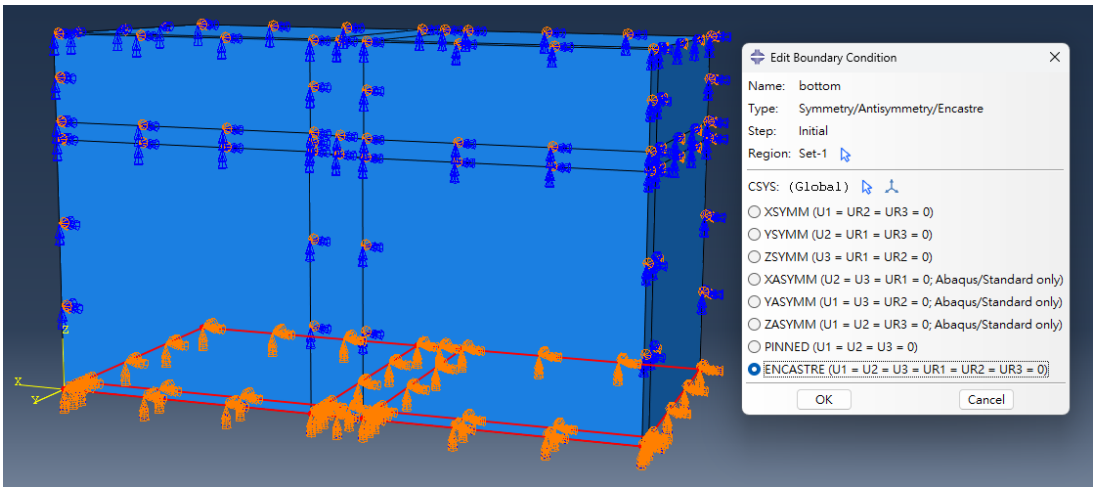

Figure 3. 20 The fixed direction at the bottom of the model

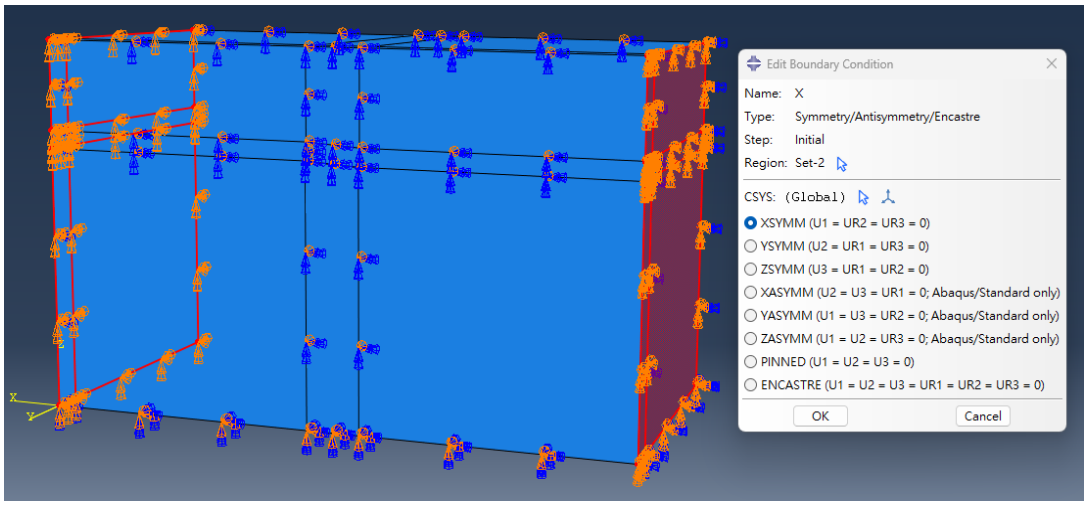

Figure 3. 21 The fixed direction at the side of the model

doi:10.6342/NTU202403515

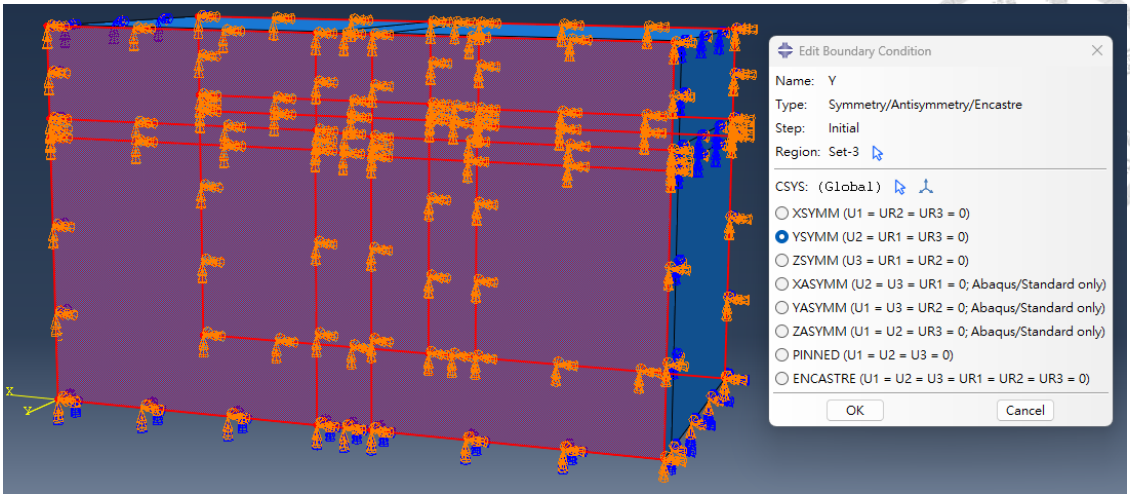

Figure 3. 22 The fixed direction at the front and rear of the model

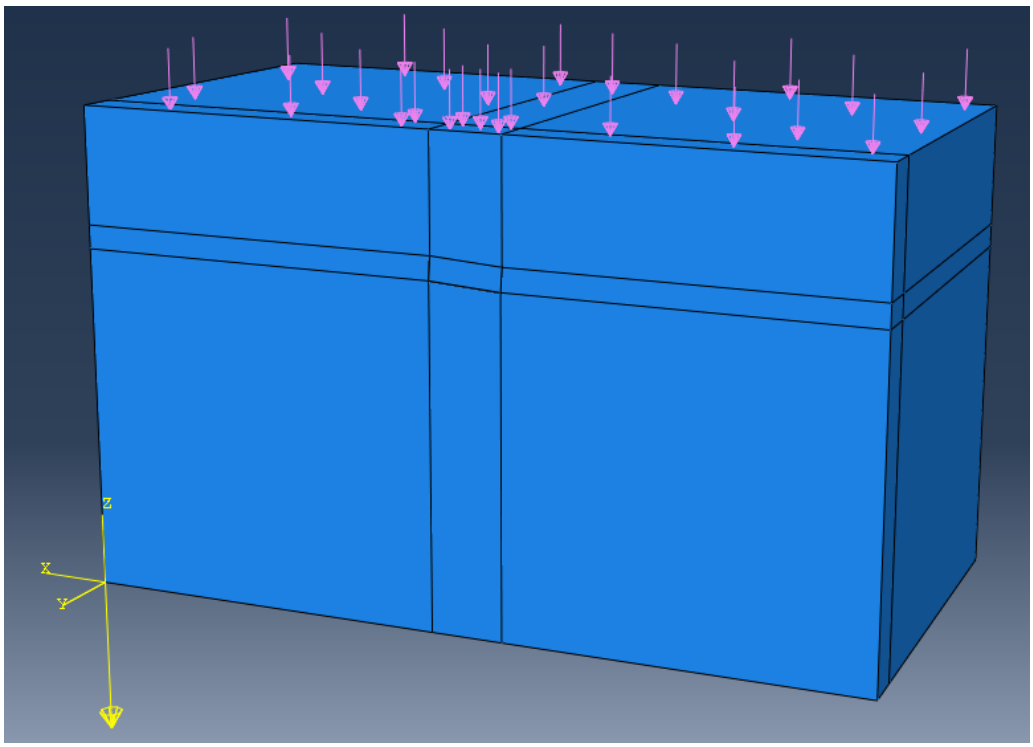

Figure 3. 23 Water pressure at the top and gravity

doi:10.6342/NTU202403515

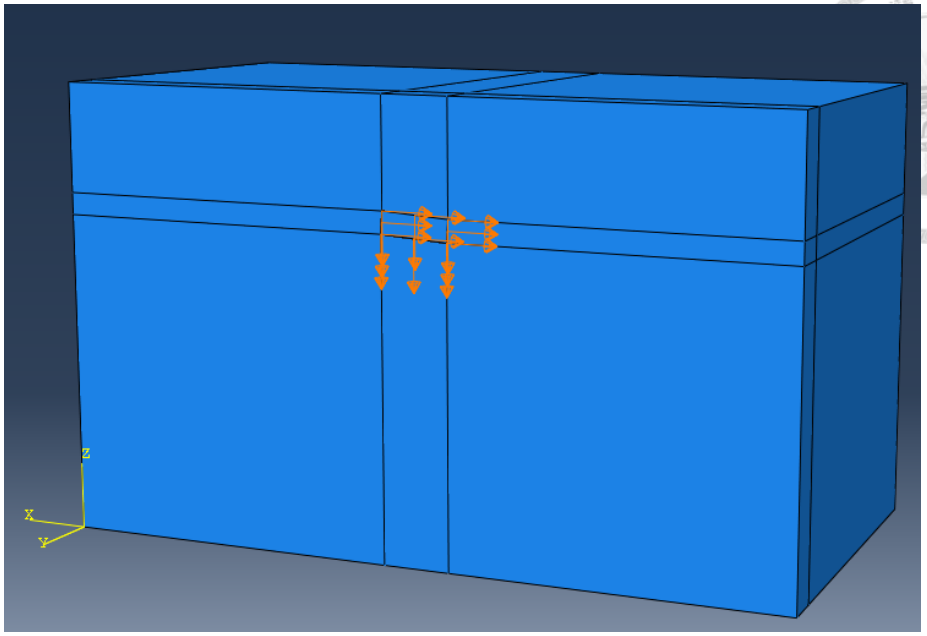

Figure 3. 24 Specify the displacement distance of the drag anchor

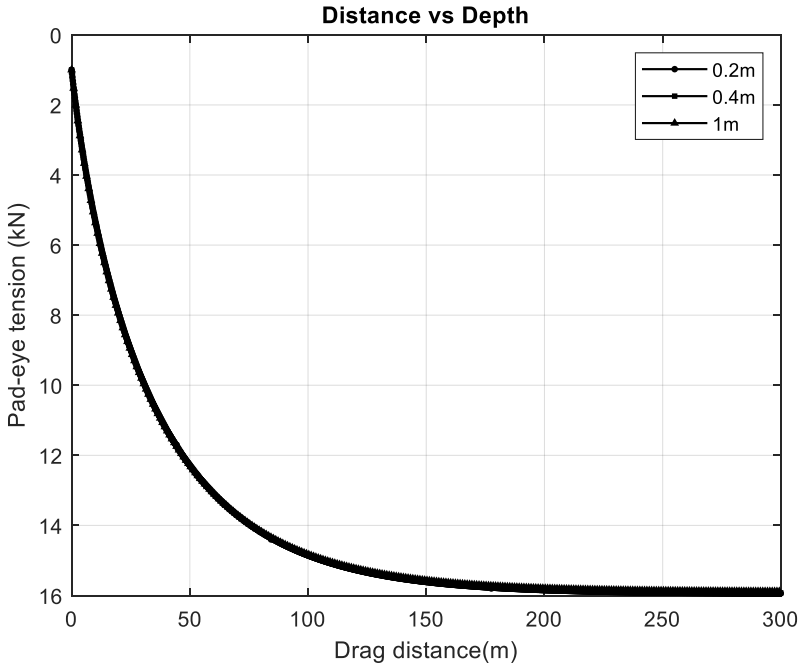

Figure 3. 25 Prediction of dragging distance and embedment depth under different iteration distances

doi:10.6342/NTU202403515

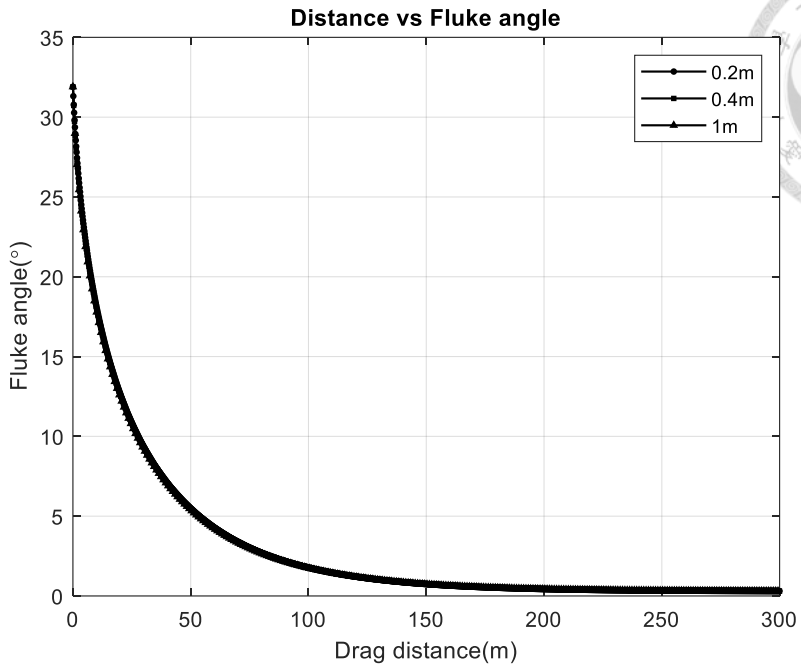

Figure 3. 26 Prediction of dragging distance and fluke angle under different iteration distances

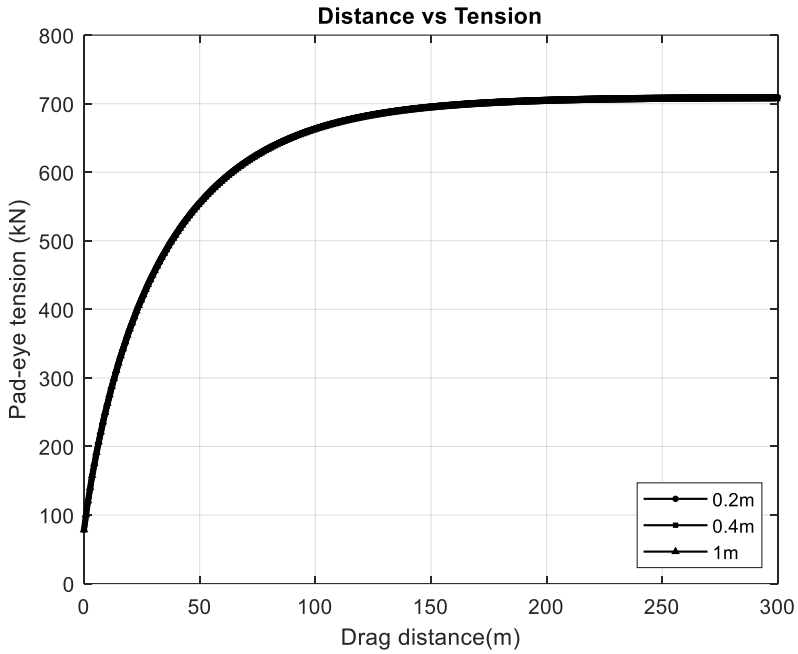

Figure 3. 27 Prediction of dragging distance and pad-eye tension under different iteration distances

doi:10.6342/NTU202403515

3.2.7 Mesh Size and Elements

Due to the significant impact of the geometry of the anchor and soil on mesh generation, which in turn affects the selection of element types, this section will introduce the types of mesh and elements used in the simulation.

For the simplified model and the surrounding soil model, due to their relatively simple geometry, ABAQUS's built-in geometric partitioning tool can be used to divide the model into multiple hexahedrons. Therefore, hexahedral mesh is employed for meshing, and C3D8R elements are used for analysis. The illustrations of the meshing and element types are shown in Figures 3.28 and 3.29. The mesh size for both the anchor and the surrounding soil is 0.2 meters. For the non-critical areas of the soil, the built-in mesh size reduction tool is used to generate the mesh. The size reduction area spans from the soil boundary to the anchor boundary, with the mesh size decreasing from 2.5 meters to 0.2 meters.

For the true model and the surrounding soil, due to their complex geometry, it is not possible to divide the model into hexahedrons, thus hexahedral meshing cannot be used. Instead, tetrahedral meshing is employed. In this study, because there are extensive contact calculations, C3D10 elements are used for the simulation. The illustrations of the meshing and element types are shown in Figures 3.30 to 3.32. The mesh size for the anchor and the surrounding soil is 0.25 meters. For the non-critical areas of the soil, a mesh size of 1.5 meters is used.

doi:10.6342/NTU202403515

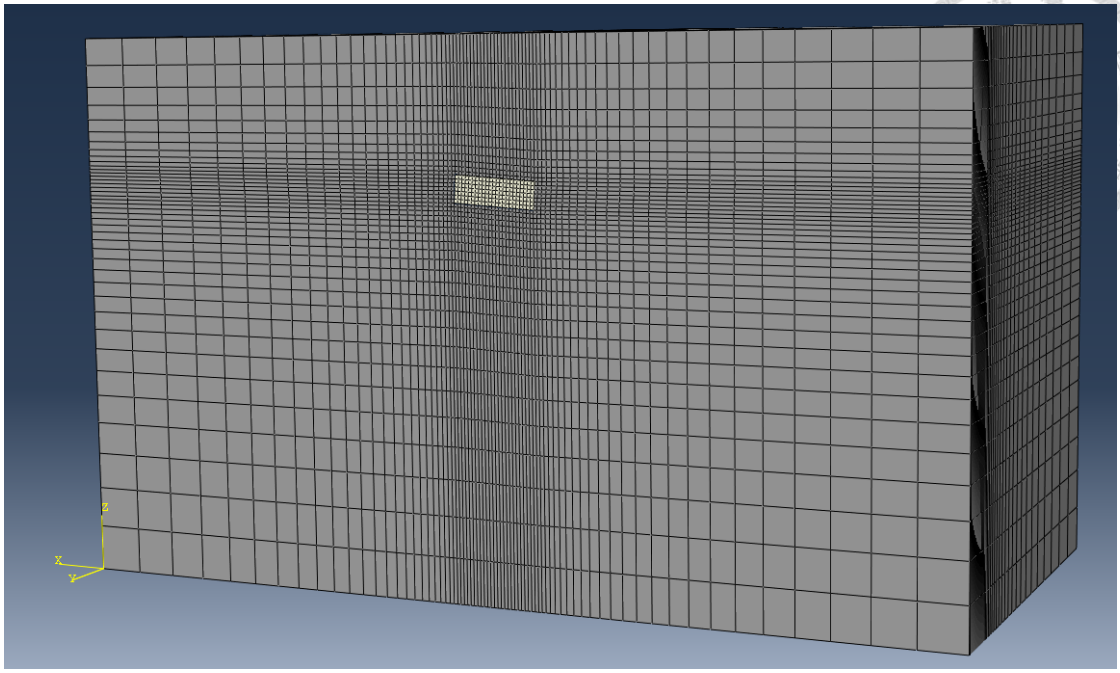

Figure 3. 28 Mesh of the simplified model and its surrounding soil

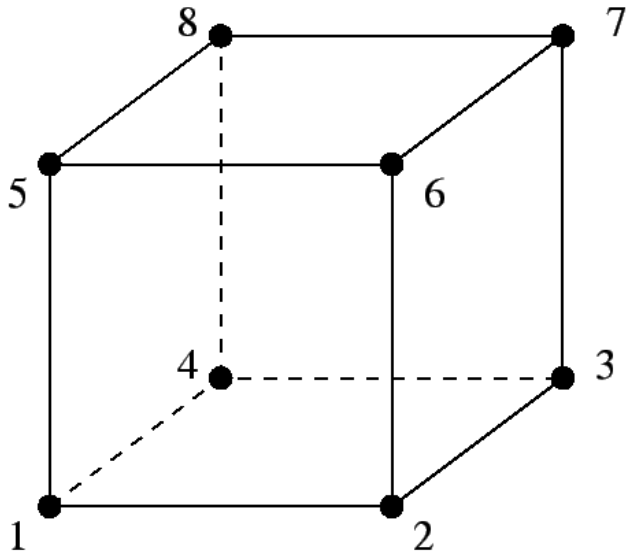

Figure 3. 29 C3D8R elements (Abaqus, 2022)

doi:10.6342/NTU202403515

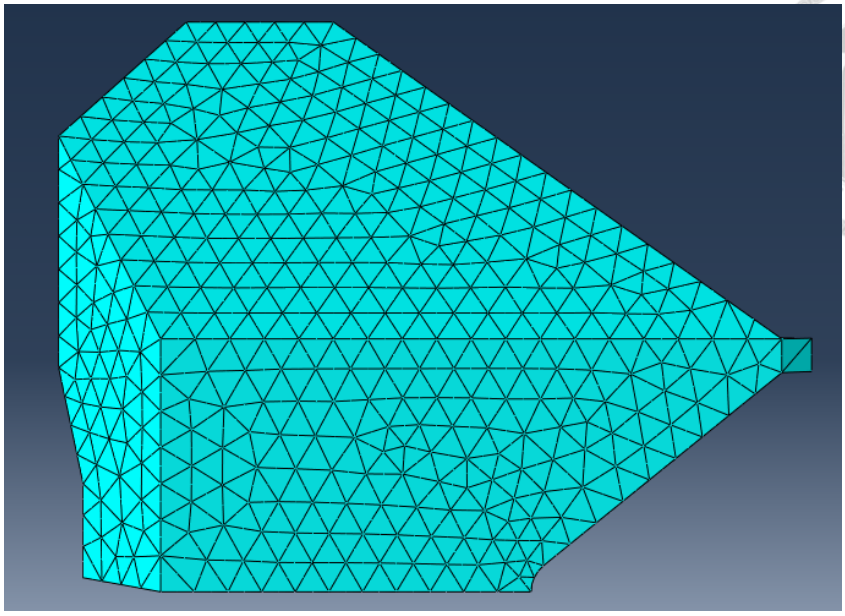

Figure 3. 30 Mesh of true model

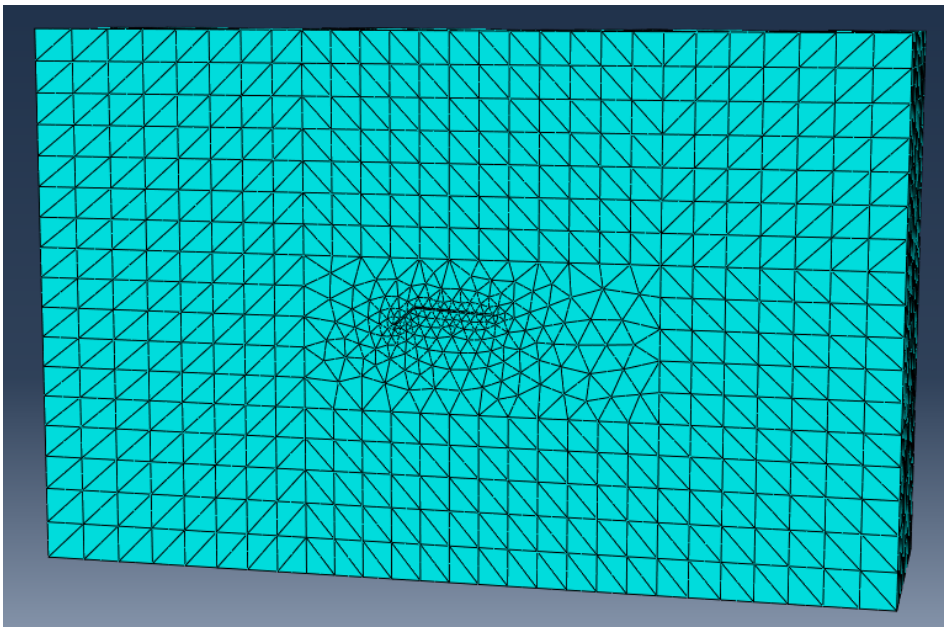

Figure 3. 31 Mesh of the simplified model and its surrounding soil

doi:10.6342/NTU202403515

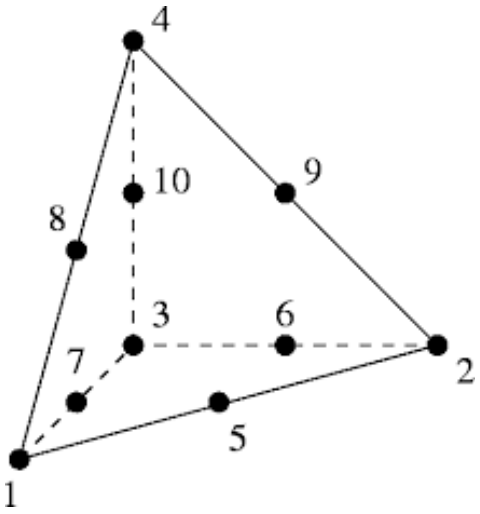

Figure 3. 32 C3D10 elements (Abaqus, 2022)

3.3 Earthquake Analysis

3.3.1 Model Calibration

Unlike Section 3.2, the focus of this section is on applying seismic forces after the completion of anchor dragging and observing the variation of holding capacity during the earthquake. Due to the presence of seismic waves in the model, both the model and mesh sizes need to be reconsidered and cannot be directly adopted from Section 3.2. In this section, we will introduce the modeling process for dynamic analysis, including considerations for model size, mesh size, and boundary condition settings.

According to Su (2021), when analyzing three-dimensional dynamic problems, the length and width of the model should be four times the maximum wavelength. The material parameters used in the model are listed in Table 3.4. Using these material parameters, the shear wave velocity and wavelength are calculated using Equation 3.6 and Equation 3.7. Taking frequencies from 1Hz to 10Hz as the primary frequency range for our seismic analysis, the longest wavelength will occur at 1Hz. According to Equation 3.6, the calculated shear wave velocity is 189.6 m/sec. Using Equation 3.7, the longest wavelength is determined to be 189.6 meters, making the length and width of the model

doi:10.6342/NTU202403515

758.4 meters. For the model height, according to Su (2021), it should be four times the highest wave velocity. In this study, the soil material used includes Rayleigh damping, which significantly increases computational time compared to materials without damping. Adopting a height four times the wave velocity would consume a considerable amount of analysis time. Therefore, at the bottom part of the model, the built-in "rigid couple" feature of ABAQUS is utilized, treating the model bottom as a rigid body. This setup allows disregarding the limitation imposed by wave velocity magnitude. Eventually, a model height of 30 meters was chosen for this study.

$$G = \rho V_S^2 \tag{3.6}$$

$$V_S = \lambda f \tag{3.7}$$

In terms of mesh size, Kuhlemeyer and Lysmer (1973) suggest that the mesh size for dynamic analysis should be smaller than $\frac{1}{10}$ of the shortest wavelength. Therefore, in this model, the maximum mesh size is set to 1.896 meters. The mesh size decreases from non-essential areas towards the vertical and horizontal directions where the anchor is located, ensuring the accuracy of the anchor's response to seismic waves while reducing the number of elements. To absorb and dissipate the energy of seismic waves, infinite elements are used around the model. Since infinite elements already provide a "quiet boundary," no boundary conditions need to be set for the boundaries with infinite elements. However, since infinite elements are not used at the bottom, all normal motion degrees of freedom need to be fixed (U3=UR1=UR2=0). Subsequently, acceleration is applied to the rigid body at the bottom for earthquake analysis.

After the model setup, model validation was performed, assuming no consideration of soil nonlinearity, only verifying wave propagation effects. The simulation results, as

doi:10.6342/NTU202403515

shown in Figure 3.35, were compared with DEEPSOIL's results, indicating good wave propagation results and confirming the adequacy of the boundary conditions.

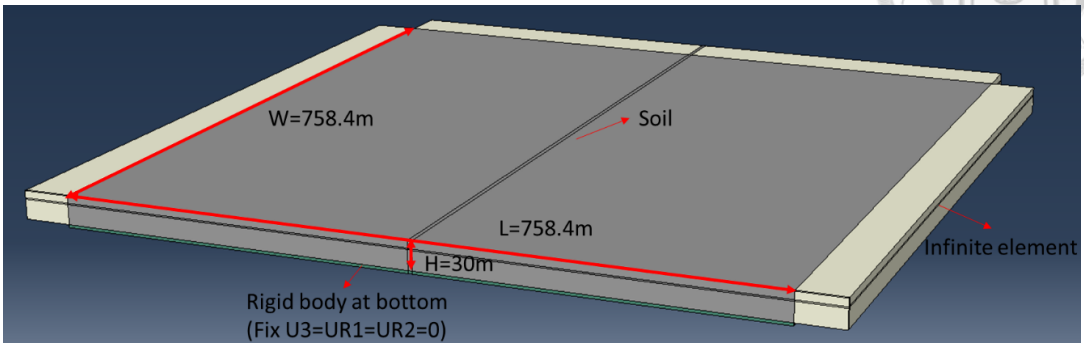

Figure 3. 33 Model size for earthquake analysis

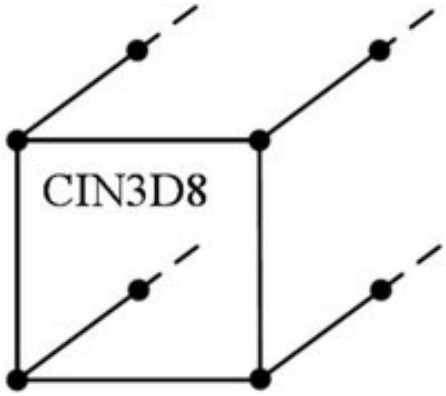

Figure 3. 34 Infinite element (Abaqus, 2022)

doi:10.6342/NTU202403515

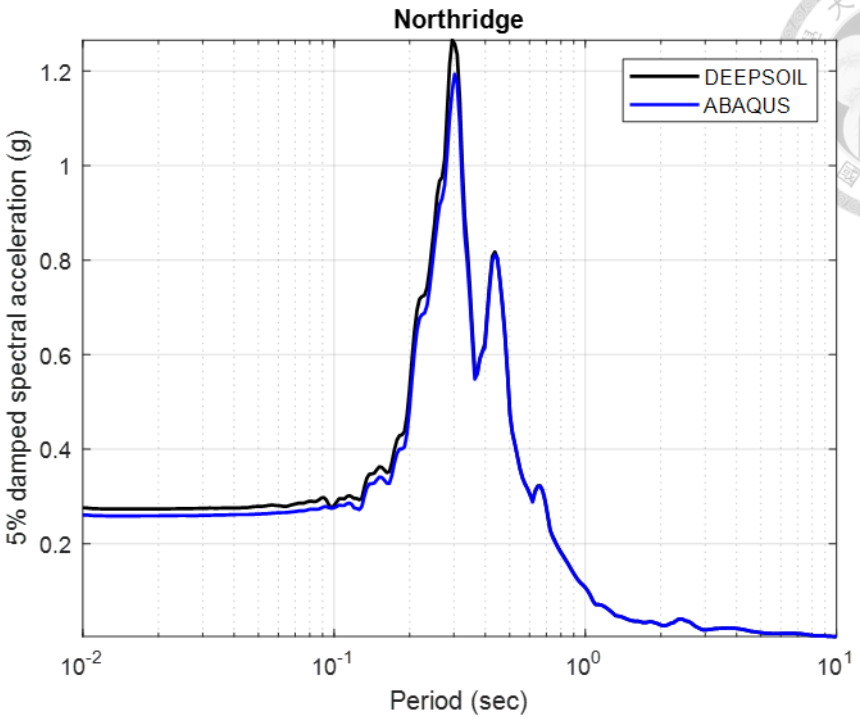

Figure 3. 35 Comparison of wave propagation analysis results between ABAQUS and DEEPSOIL

3.3.2 Material and Element Test

In this section, the soil parameters from Table 3.4 are used for earthquake analysis. Unlike Section 3.2.4, to simulate the nonlinear behavior of soil during an earthquake, the Mohr-Coulomb model is replaced by a simplified nonlinear kinematic (SNKH) model as the constitutive model for the soil. According to Equations 2.38 and 2.39, the calculated parameters are shown in Table 3.7. These parameters are input into ABAQUS for fitting the shear modulus reduction curve, as shown in Figure 3.36.

After determining the input parameters in ABAQUS, a element test will be conducted to fit the soil's shear modulus reduction curve. The boundary conditions and input motion for the element test are shown in Figures 3.37 and 3.38. As shown in Figure 3.37 and Figure 3.38, the bottom of the model is fixed in all three displacement degrees of freedom (U1=U2=U3). A horizontal displacement control is applied at the top. It is

doi:10.6342/NTU202403515

important to note that the non-shear direction displacement degrees of freedom at the top should be fixed (U1=1; U2=U3=0). After completing the shear test, the shear stress (S12) at the peak is output and the G/G_{max} value at that shear strain is calculated. The comparison between the fitted data points and the target curve is shown in Figure 3.39. The target curve is based on Vucetic and Dobry (1991) with PI=30. The fitting is less accurate at small shear strains compared to high shear strains, but the overall results are still quite satisfactory. Finally, a one-dimensional ground response analysis was conducted using the Northridge earthquake, and its response spectrum was compared, as shown in Figure 3.40. Overall, these results demonstrate the feasibility of using the SNKH model to simulate the nonlinear behavior of soil.

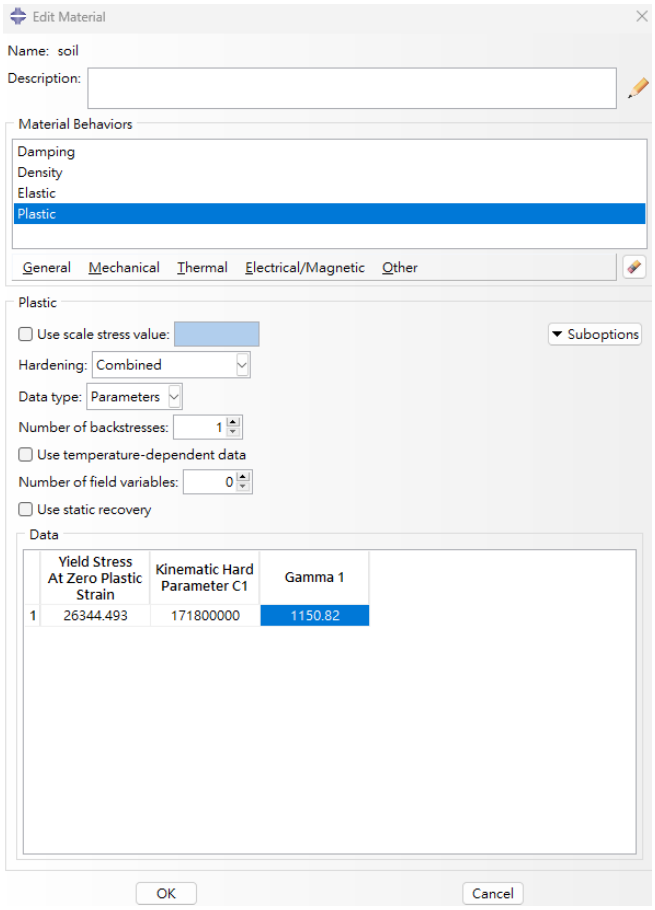

Figure 3. 36 Input parameters in ABAQUS

doi:10.6342/NTU202403515

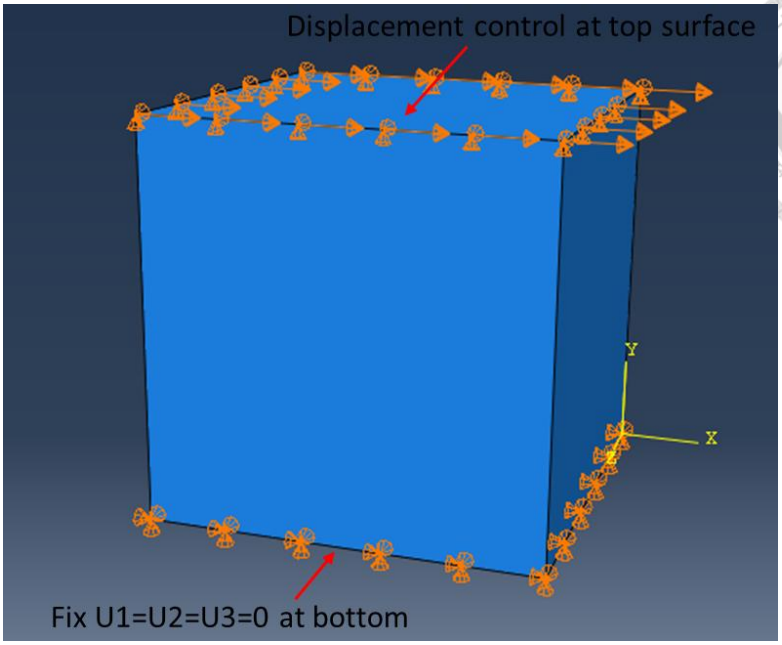

Figure 3. 37 Element test

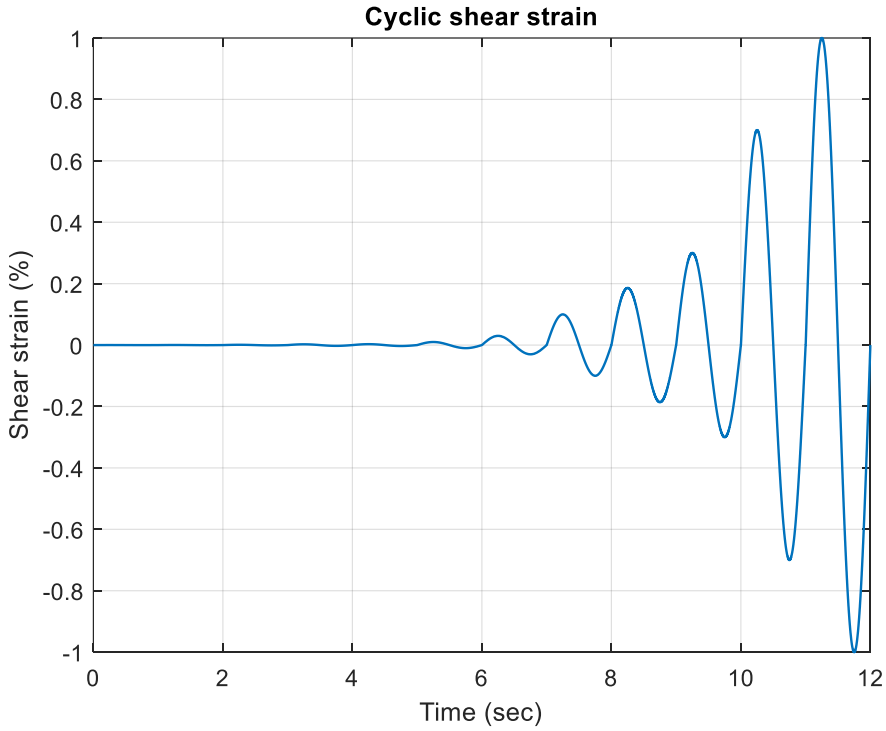

Figure 3. 38 Input motion for the element test

doi:10.6342/NTU202403515

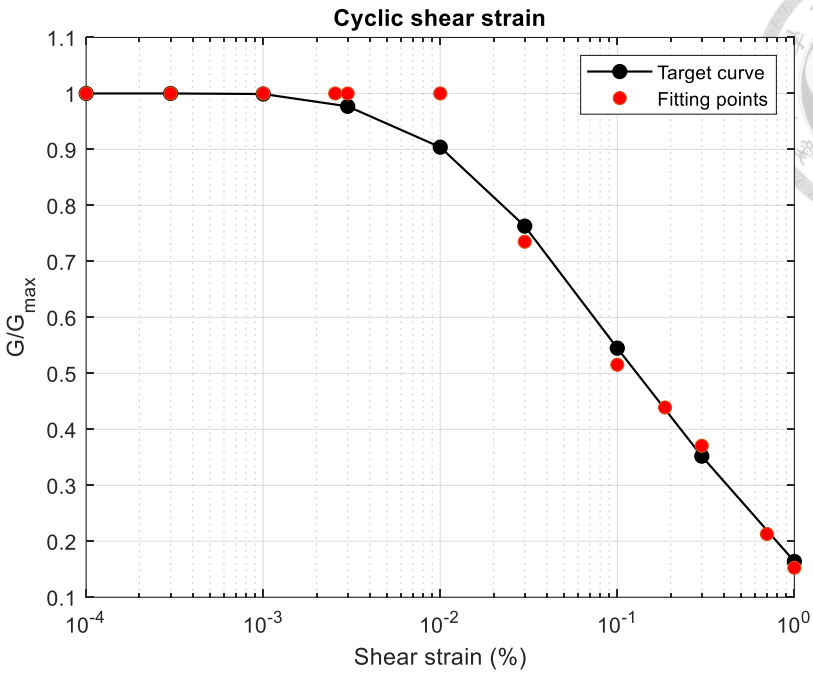

Figure 3. 39 The comparison between the G/Gmax obtained from the SNKH model and the target curve

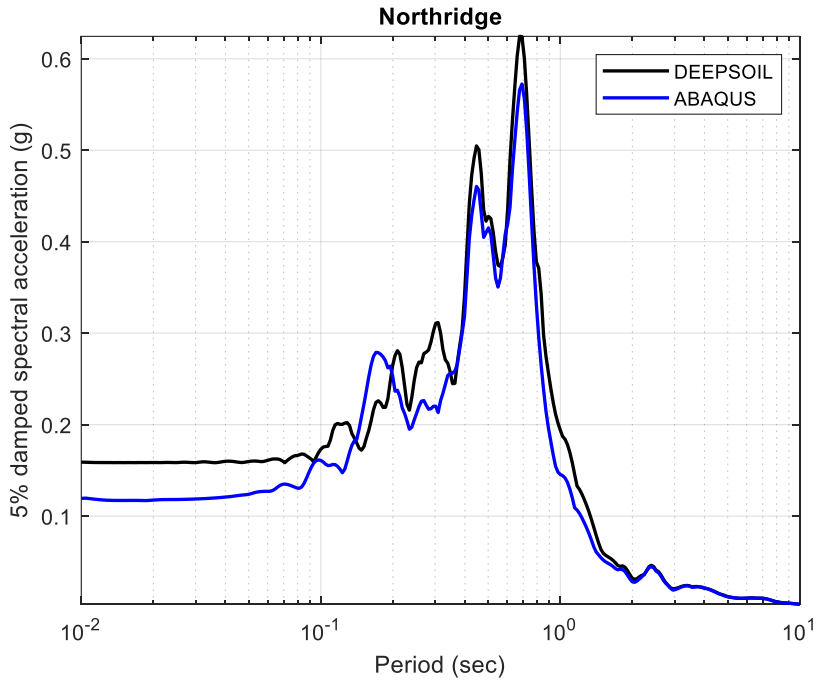

Figure 3. 40 The comparison of the response spectrum obtained from the SNKH model simulation and the response spectrum from DEEPSOIL

doi:10.6342/NTU202403515

Table 3.7 The parameters of SNKH model

σ_y (Pa)	λ (0.1-0.3)	$\sigma\|_0$ (Pa)	C (Pa)	γ_{kh}
175629.952	0.15	26344.493	171800000	1150.82

3.4 Estimation of Stress Softening Index

3.4.1 Earthquakes and Stations Used for Calculating the Softening Index (Without Ground Response Analysis)

In this study, we will investigate the impact of different PGA on the softening index and the effect of earthquakes with varying periods on the softening index. When examining the differences in PGA, we used the ChiChi and Kobe earthquakes for comparison, and we also compared the calculation differences between records from different stations. When exploring the effects of earthquakes with different periods, we compared the ChiChi and Kocaeli earthquakes.

When investigating the differences between different PGA and stations, we used the earthquake records from DEEPSOIL and the data from the maximum acceleration stations in the PEER database for our calculations. Figure 3.41 and Figure 3.42 show the acceleration time histories from DEEPSOIL, while Figure 3.43 and Figure 3.44 present the acceleration time histories from the PEER database. Figures 3.45 to 3.46 show the acceleration time histories at the top of the soil obtained from one-dimensional site response analyses using the acceleration time histories from DEEPSOIL. Figures 3.47 to 3.48 show the acceleration time histories at the top of the soil obtained from one-dimensional site response analyses using the acceleration time histories from the PEER database. Figures 3.49 and 3.50 show the surface response spectra obtained using the

doi:10.6342/NTU202403515

DEEPSOIL station and the station with the maximum earthquake record, respectively. These are used for subsequent cyclic softening calculations.

When investigating the impact of earthquakes with different periods, the ChiChi, and Kocaeli earthquakes represent long, and short-period earthquakes, respectively. Using the input motion from the ChiChi earthquake in the PEER database as a reference, the PSA of the Kocaeli earthquake was amplified to match the ChiChi earthquake's PSA of 3.5g. Additionally, scenarios with both PSAs set to 2.66g were explored. Figures 3.51 and 3.52 show the response spectra for PSAs of 3.5g and 2.66g, respectively. Figures 3.53 and 3.54 show the ground surface response spectra for PSAs of 3.5g and 2.66g, respectively. These figures are used for subsequent cyclic softening calculations.

Tables 3.8 to 3.10 present the information and calculation results for the ChiChi and Kobe earthquakes, including earthquake magnitude, PGA, and spectral accelerations at periods of 1 second and 0.2 seconds. Table 3.11 lists the scaled factors and corresponding results for earthquakes of different periods. The Nc and gamma values in Table 3.10 and Table 3.11 were not obtained through ground response analysis. Section 3.4.3 will introduce how to obtain Nc and gamma using the results of ground response analysis.

doi:10.6342/NTU202403515

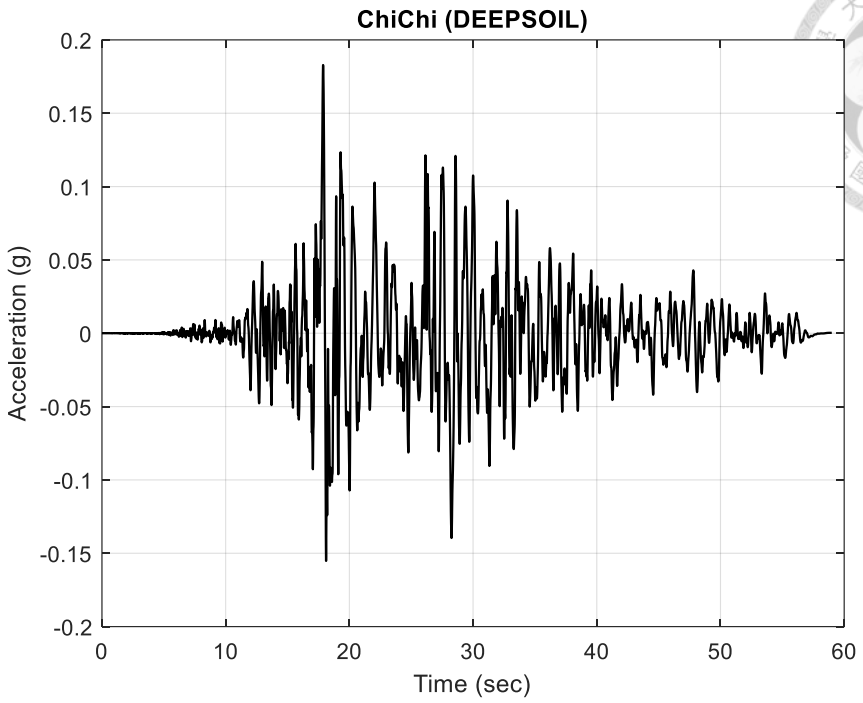

Figure 3. 41 Acceleration time history of the ChiChi earthquake (DEEPSOIL)

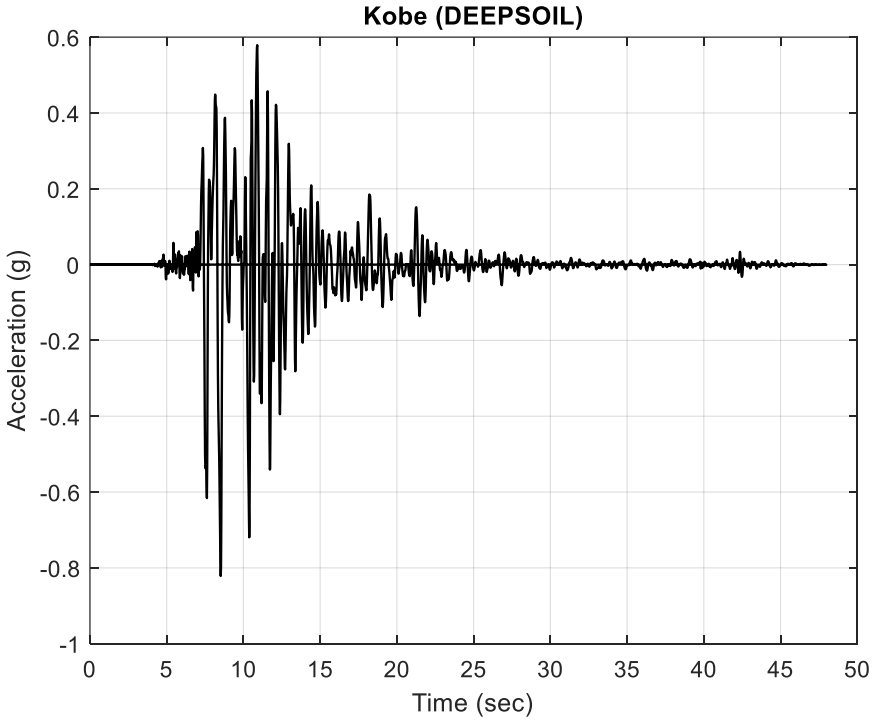

Figure 3. 42 Acceleration time history of the Kobe earthquake (DEEPSOIL)

doi:10.6342/NTU202403515

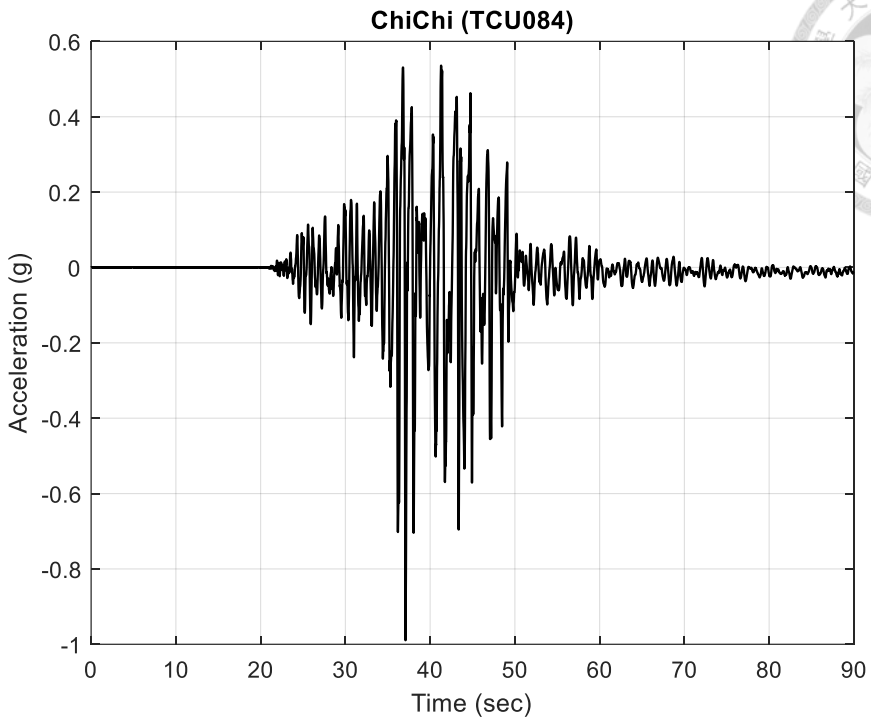

Figure 3. 43 Acceleration time history of the ChiChi earthquake (TCU084)

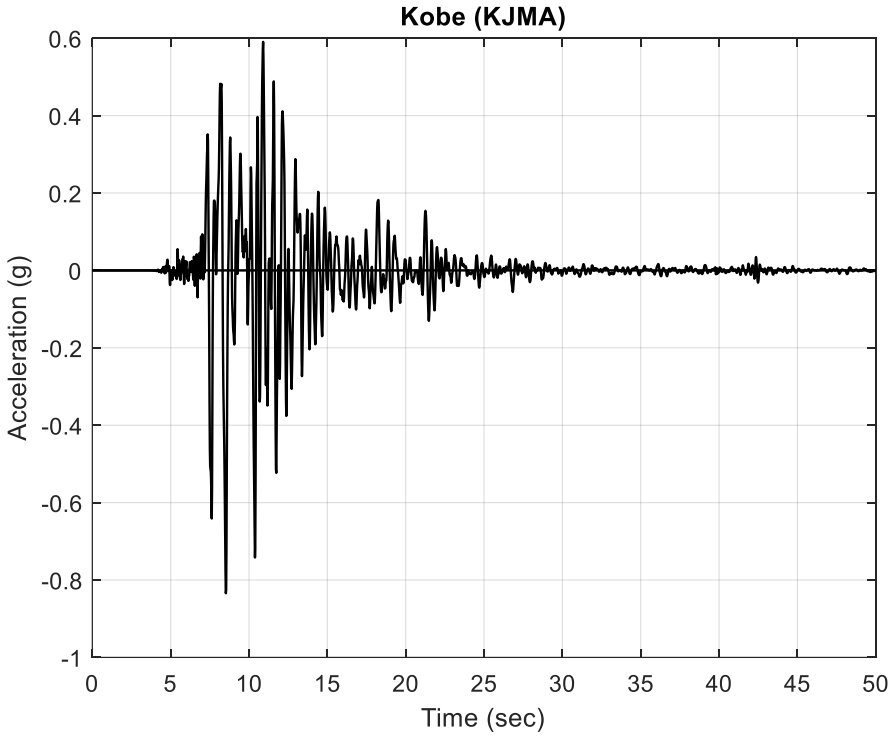

Figure 3. 44 Acceleration time history of the Kobe earthquake (KJMA)

doi:10.6342/NTU202403515

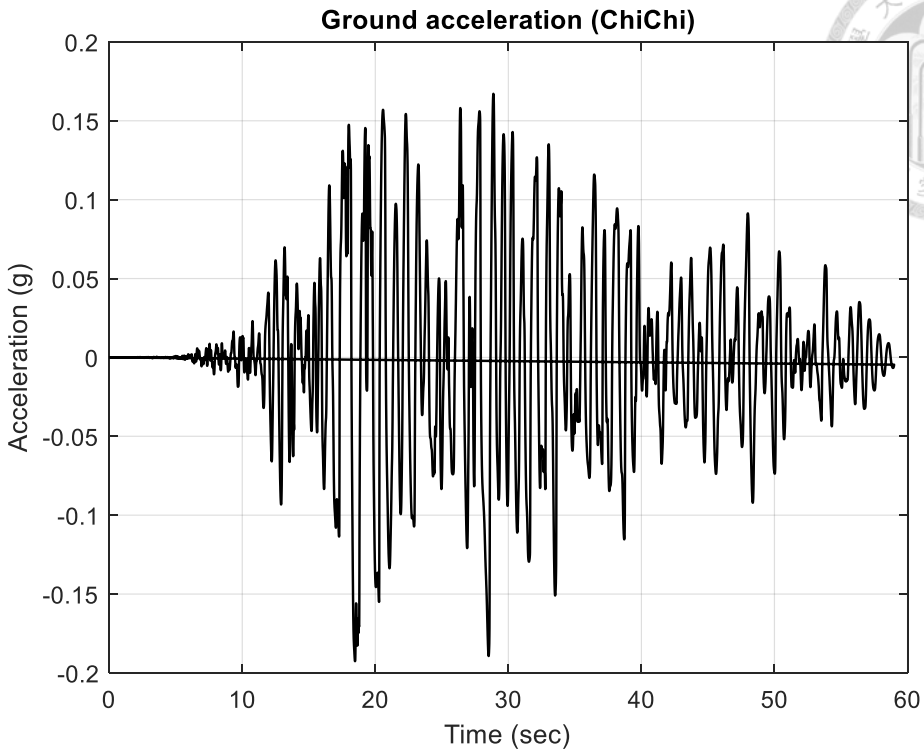

Figure 3. 45 The ground acceleration of the ChiChi earthquake (DEEPSOIL)

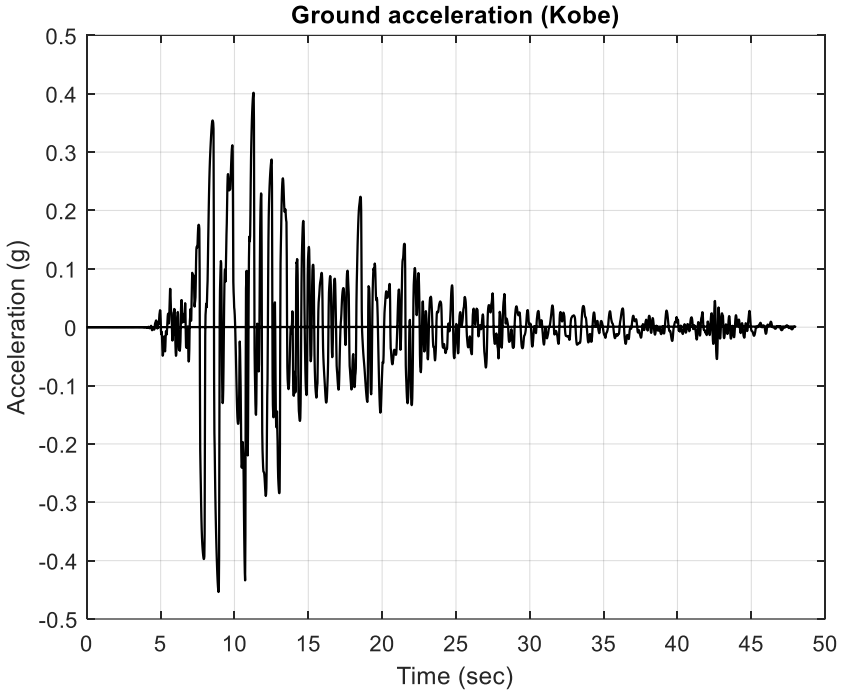

Figure 3. 46 The ground acceleration of the Kobe earthquake (DEEPSOIL)

doi:10.6342/NTU202403515

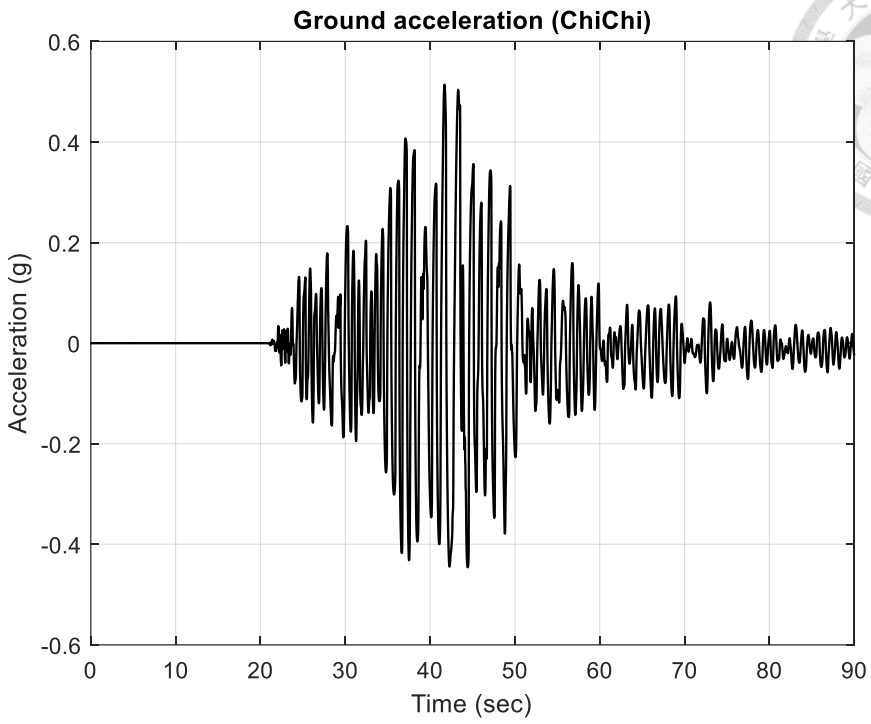

Figure 3. 47 The ground acceleration of the ChiChi earthquake (TCU084)

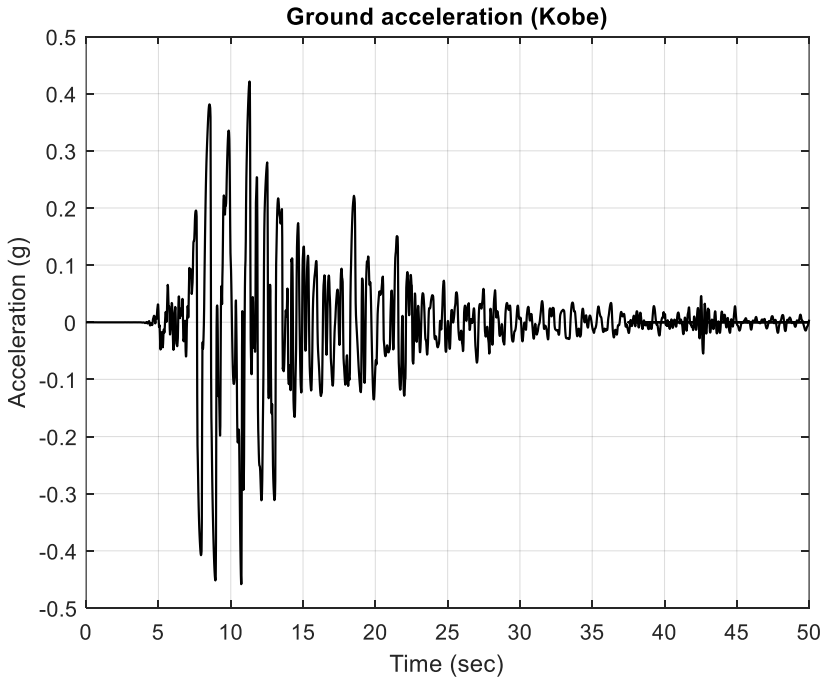

Figure 3. 48 The ground acceleration of the Kobe earthquake (KJMA)

doi:10.6342/NTU202403515

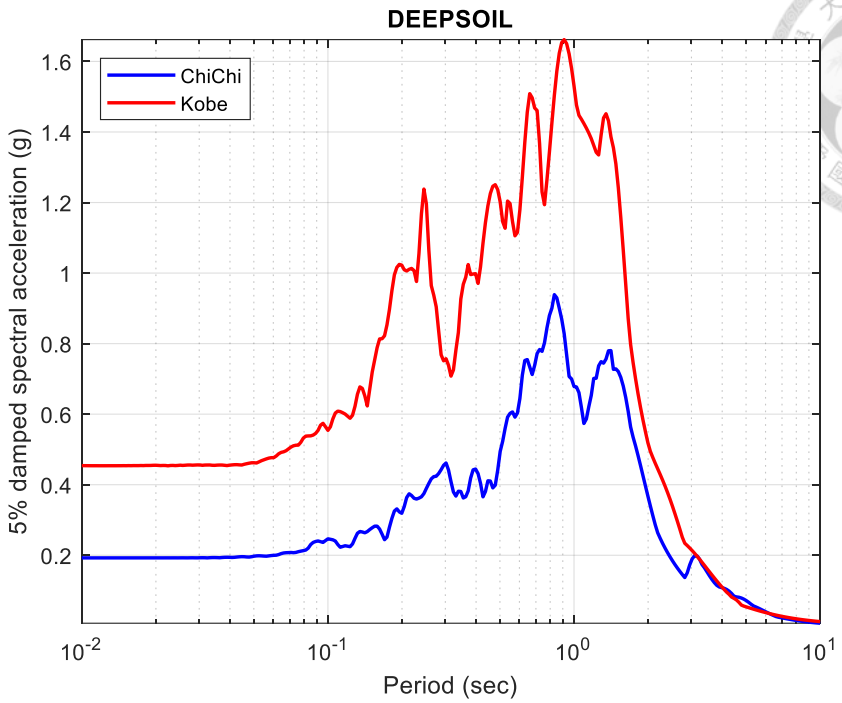

Figure 3. 49 Response spectrum of the earthquake used for cyclic softening calculations (DEEPSOIL)

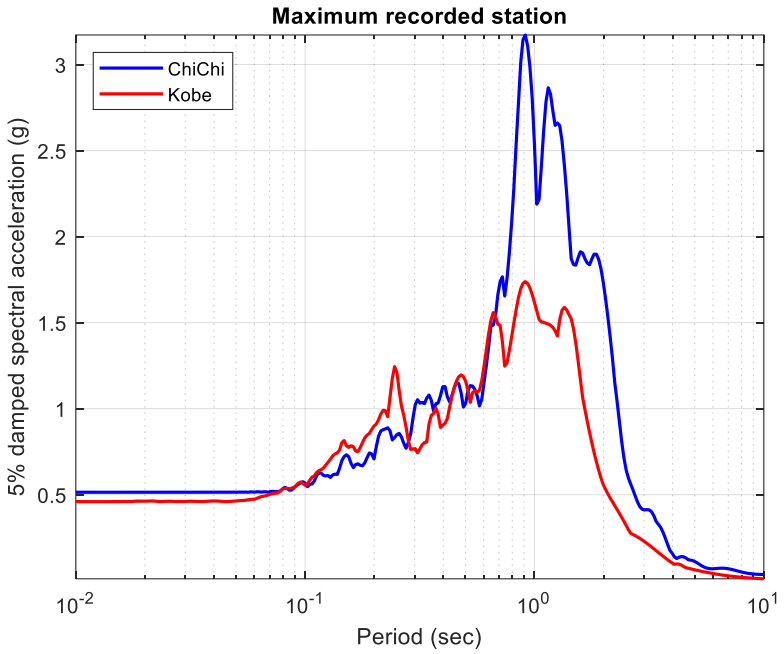

Figure 3. 50 Response spectrum of the Kobe earthquake used for cyclic softening calculations (PEER)

doi:10.6342/NTU202403515

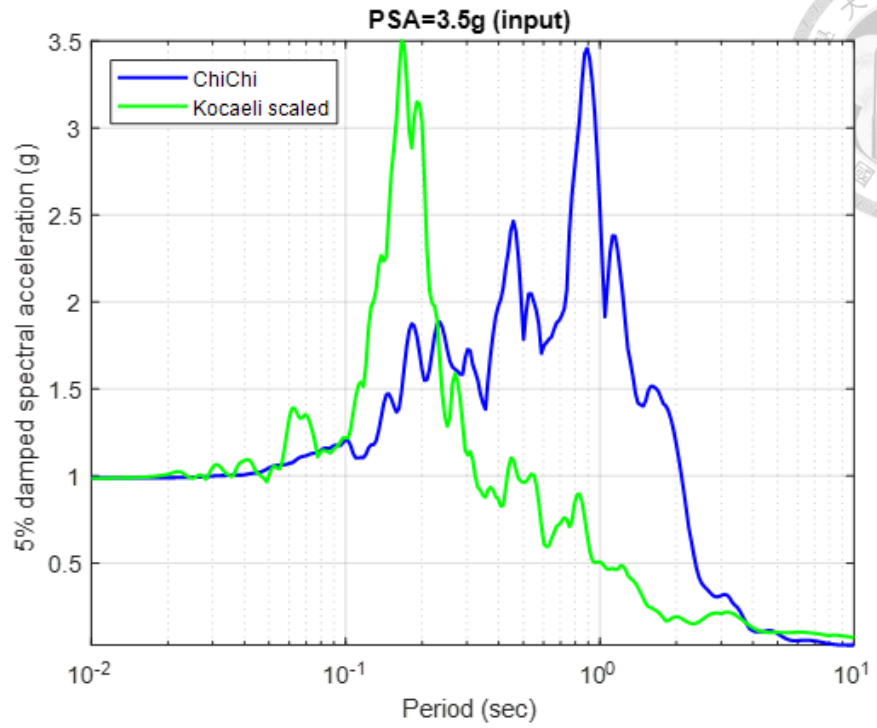

Figure 3. 51 The response spectrum when PSA=3.5 (input motion)

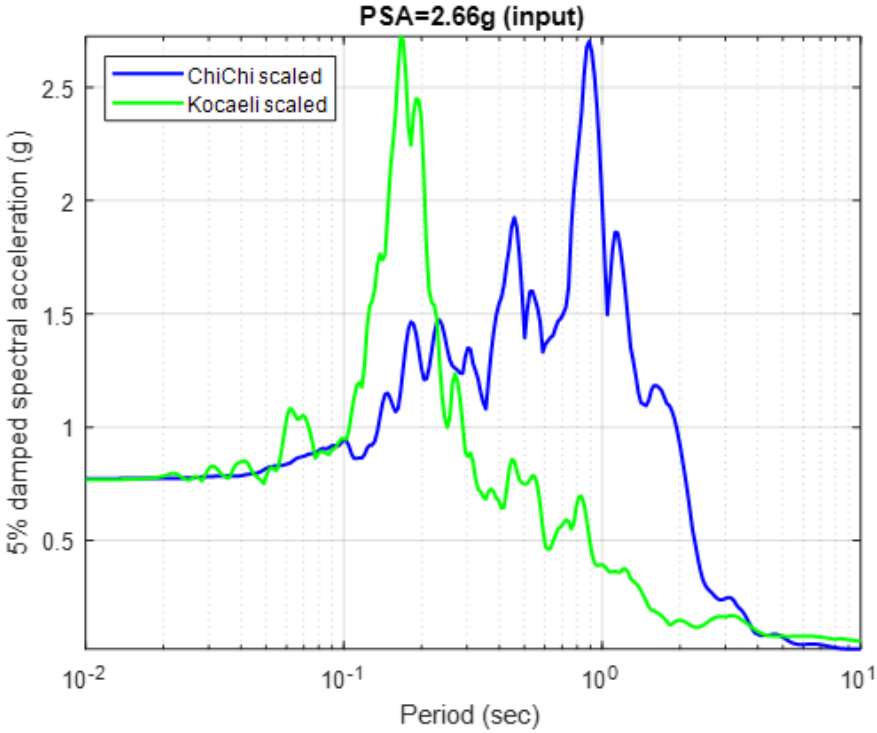

Figure 3. 52 The response spectrum when PSA=2.66 (input motion)

doi:10.6342/NTU202403515

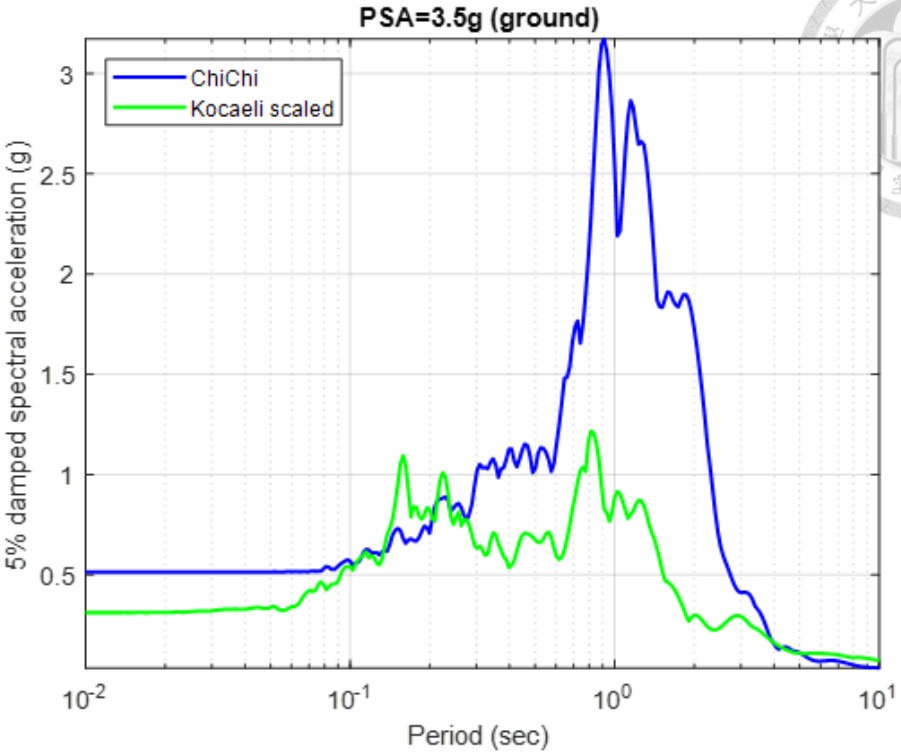

Figure 3. 53 The response spectrum when PSA=3.5 (ground)

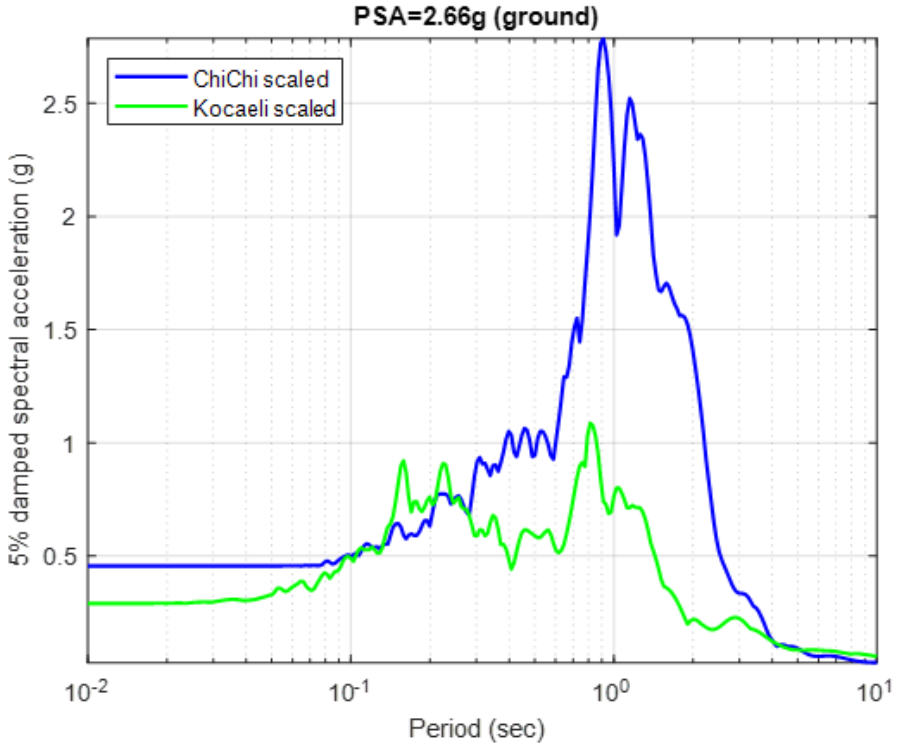

Figure 3. 54 The response spectrum when PSA=2.66 (ground)

doi:10.6342/NTU202403515

Table 3.8 Different earthquake sources and PGA

Earthquake	Station	Magnitude (M_w)	PGA (g)
ChiChi	DEEPSOIL	7.7	0.193
Kobe	DEEPSOIL	6.9	0.454
ChiChi	TCU084	7.7	0.514
Kobe	KJMA	6.9	0.458

Table 3.9 The accelerations corresponding to the periods of the response spectra

Earthquake	Station	$S_a(1)$	$S_a(0.2)$	S1
ChiChi	DEEPSOIL	0.695	0.315	2.2063
Kobe	DEEPSOIL	1.59	1.01	1.519
ChiChi	TCU084	2.7	0.65	4.154
Kobe	KJMA	1.62	0.9	1.8

Table 3.10 The proportion of degradation caused by the earthquake loading

Earthquake	Station	Softening Index	Percentage decrease (%)
ChiChi	DEEPSOIL	0.97	3
Kobe	DEEPSOIL	0.91	9
ChiChi	TCU084	0.851	14.9
Kobe	KJMA	0.9	10

doi:10.6342/NTU202403515

Table 3.11 The proportion of degradation caused by different predominant period earthquake

Earthquake	PGA (g)	Scaled factor	Softening index	PSA (g)	Percent decrease (%)
ChiChi (TCU084)	0.514	-	0.851	3.5	14.9
Kocaeli (scaled)	0.311	4.5	0.917	3.5	8.3
ChiChi (scaled)	0.455	0.78	0.87	2.66	13
Kocaeli (scaled)	0.29	3.5	0.93	2.66	7

3.4.2 Calculation Process of Stress Softening Index (Without Ground Response Analysis)

As clay undergoes cyclic shear movements like earthquakes, it can experience softening. During this process, both the strength and stiffness of clay decrease, leading to a reduction in holding capacity. Therefore, this section analyzes the strength degradation of clay after cyclic loading and integrates the reduced strength into the model for another drag anchor analysis to determine the softened holding capacity. The simplified assessment method proposed by Tsai et al. (2014) relates the extent of strength degradation to the Over-Consolidation Ratio (OCR) and Plasticity Index (PI) values. In this method, OCR influences the parameters s and r used in the fitting process, while PI values also impact the corresponding shear modulus reduction curve calculation.

1. Determine the seismic magnitude and Peak Ground Acceleration (PGA) as shown in Table 3.8 and Table 3.11.

doi:10.6342/NTU202403515

2. The $G_{\max}$ values of the soil are obtained from Table 3.4.

3. Calculate $\gamma_{eff} = \frac{G}{G_{\max}}$ using Equation 2.31, and then use Figure 2.12 to find the corresponding shear strain for the soil. For Equation 2.31, r_d is calculated using Seed et al.(2003) Equation 2.

4. Use Equation 2.34 to convert the irregular amplitudes of the earthquake into an equivalent number of uniform amplitude cycles for laboratory testing. The response spectrum of the ChiChi, Kobe and Kocaeli are shown in Figures 3.49 to 3.54

5. Finally, using Equation 2.29, we calculate the softening index. Since OCR=1, we use s=0.075, r=0.495, and γ_t =0.03 for the calculations.

doi:10.6342/NTU202403515

3.4.3 Earthquakes and Stations Used for Calculating the Softening Index (Based on Ground Response Analysis)

In this section, earthquake cases analyzed using ground response analysis will be introduced.

When performing Ground Response Analysis using DEEPSOIL, a soil column height of 30 meters was used. The soil parameters are shown in Table 3.4. The shear modulus curve used was from Darendeli (2001) for PI=15 and OCR=K0=1, with Rayleigh damping set at 5%. Since the anchor's ultimate depth is 7.4 meters, the ground response analysis results at a depth of 7.5 meters were used for the calculation. The selected results include the shear stress history and stress-strain curve.

The DEEPSOIL built-in ChiChi and Kobe earthquakes, as well as the maximum recorded ChiChi and Kobe earthquakes from the PEER database, were used for ground response analysis. Detailed information about these earthquakes is shown in Figures 3.41 to 3.44 and Table 3.8. According to Equations 2.35 and 2.36, the calculation of the K value requires the shear stress history of the target depth. As Kishida and Tsai (2014) mentioned, the calculation of the K value requires using the peak shear stress for each half-cycle. However, it is not clearly stated whether the half-cycle needs to pass through a shear stress of zero. Therefore, this analysis will use two methods for the calculation: the first method involves removing histories where the shear stress does not pass through zero and only using the peak values from cycles that do pass through zero. The second method involves including the peak values from the entire history, regardless of whether the shear stress passes through zero. As shown in Figures 3.55 to 3.58, the red lines represent shear stress values of zero. If the shear stress history is reduced, only the history to the left of the blue line is used for calculation.

doi:10.6342/NTU202403515

In addition to comparing different methods for selecting shear stress history, this study also discusses two different approaches for determining γ. The first approach converts the maximum shear stress of irregular earthquakes into an equivalent uniform average shear stress (τ_{avg}), and then uses the stress-strain curve of the target soil layer to obtain the shear strain under this equivalent uniform average shear stress, as shown in Figure 3.59. The second approach involves directly multiplying the maximum shear strain experienced by the target soil layer by 0.65 and then using this value in Equation 2.29 for calculation. The factor 0.65 is used as a reference coefficient for converting the irregular earthquake shear stress history into equivalent uniform average shear stress.

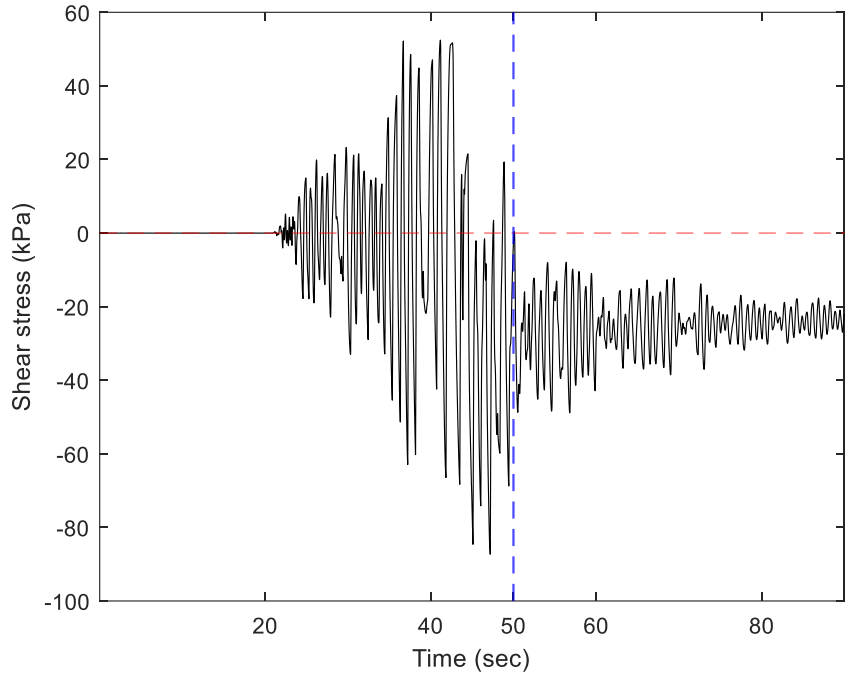

Figure 3. 55 The shear stress history at the target depth (ChiChi-TCU084)

doi:10.6342/NTU202403515

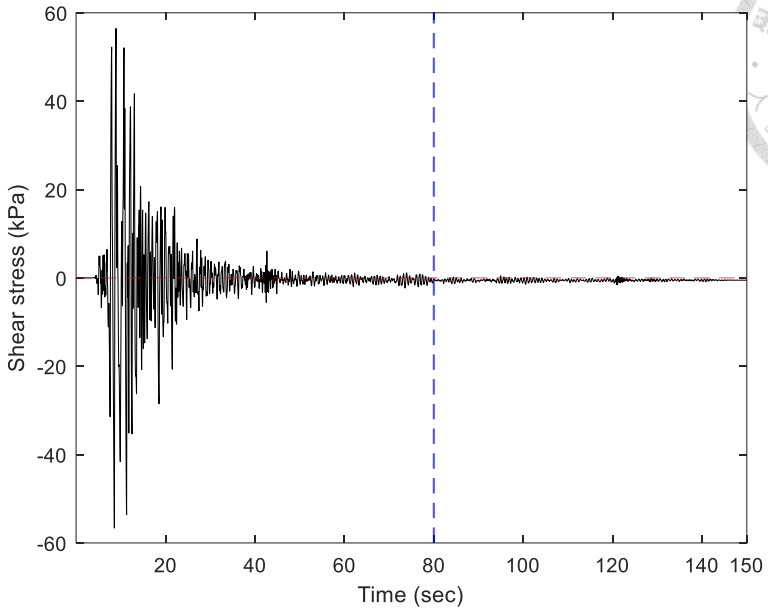

Figure 3. 56 The shear stress history at the target depth (Kobe-KJMA)

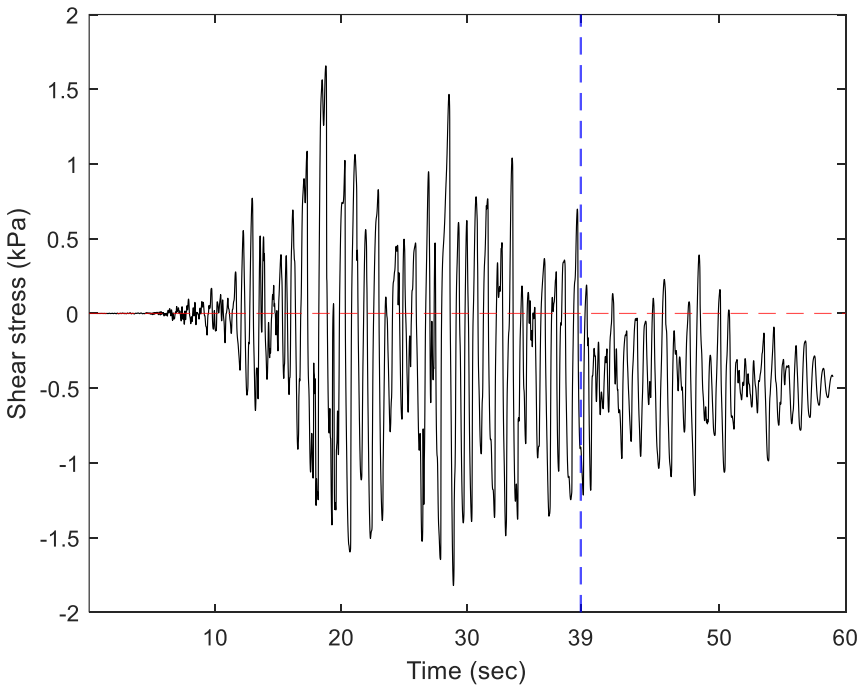

Figure 3. 57 The shear stress history at the target depth (ChiChi-DEEPSOIL)

doi:10.6342/NTU202403515

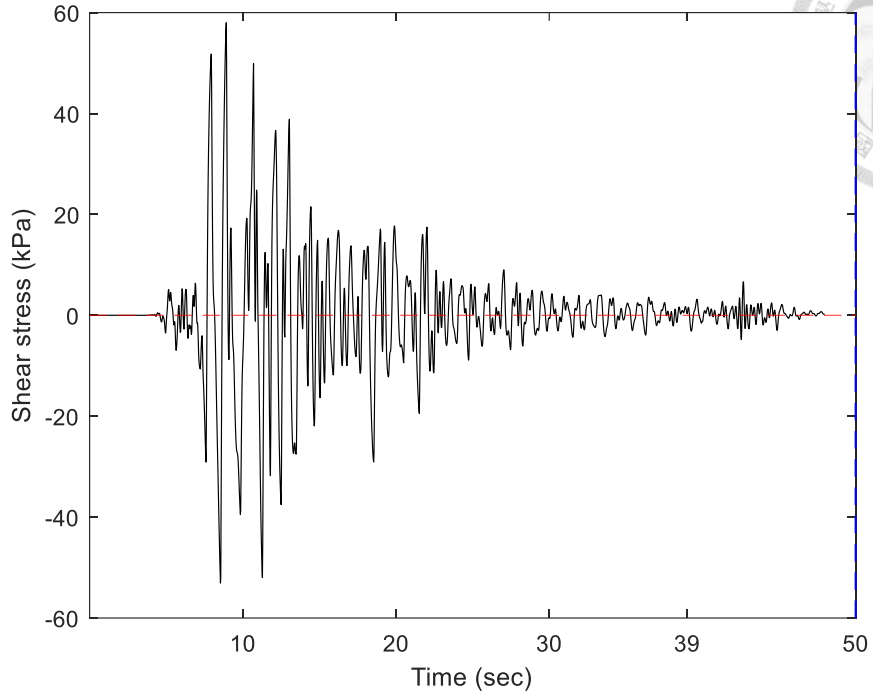

Figure 3. 58 The shear stress history at the target depth (Kobe-DEEPSOIL)

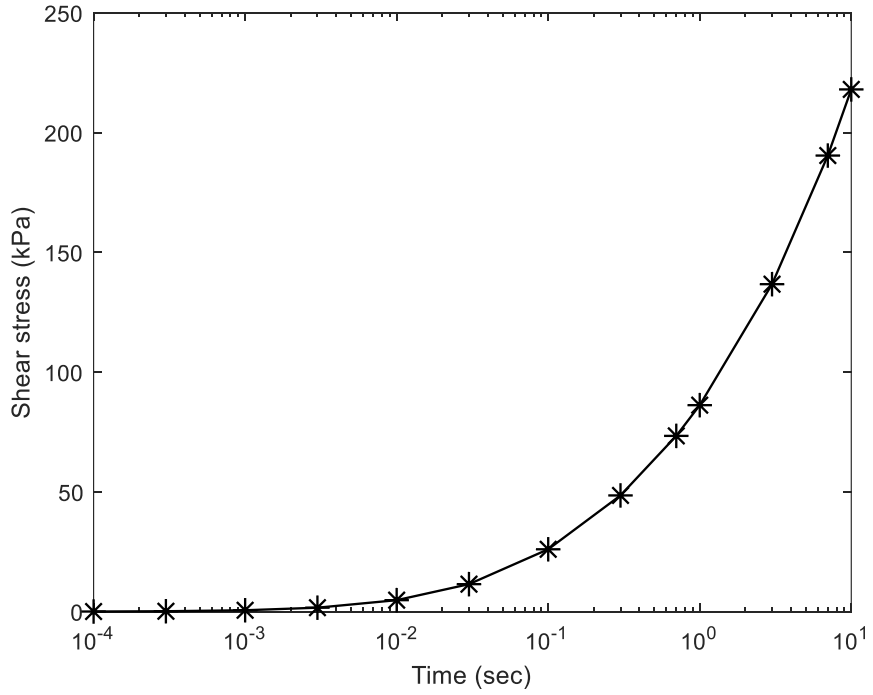

Figure 3. 59 The stress-strain curve of the target soil layer

doi:10.6342/NTU202403515

3.4.4 Calculation Result of Stress Softening Index (Based on Ground Response Analysis)

This section will present the calculation of the softening index according to the method introduced in Section 3.4.3, with the results shown in Tables 3.12 to 3.14.

The results show that the Softening index calculated by the method in Section 3.4.1 and the method in Section 3.4.3 differ only slightly. Additionally, when calculating the N_c value using the results from ground response analysis, the N_c value is significantly larger than the N_c value estimated by the empirical formula. The author believes that this difference is mainly because the empirical formula (Equation 2.34) does not account for the contribution of each peak value to the N_c value as Equation 2.35 does. Therefore, using Equation 2.35 for estimating the N_c value results in a larger value. Additionally, the N_c value calculated using the entire shear stress history is greater than the value calculated using only a portion of the history. This is because when fewer portions of the history are used, fewer peak values are accumulated, leading to a smaller overall value.

Additionally, the results show that the γ_{eff} obtained by comparing τ_{avg} with the stress-strain curve at the target depth is smaller than the value obtained by directly using $0.65\gamma_{\max}$. Therefore, under the same N_c, the reduction calculated using the γ_{eff} method derived from τ_{avg} will be smaller than the reduction calculated by directly using $0.65\gamma_{\max}$.

doi:10.6342/NTU202403515

Table 3.12 The calculation results of softening index (without ground response analysis)

Earthquake	Station	N_c	γ (%)	Softening Index	Percentage decrease (%)
ChiChi	DEEPSOIL	24.628	0.045	0.97	3
Kobe	DEEPSOIL	11.4489	0.305	0.91	9
ChiChi	TCU084	13.8745	0.7	0.851	14.9
Kobe	KJMA	10.8576	0.4	0.9	10

Table 3.13 The calculation results of softening index (use whole shear stress history)

Use $\tau_{avg} = 0.65\tau_{\max}$ then find γ_{eff}					
Earthquake	Station	N_c	γ (%)	Softening Index	Percentage decrease (%)
ChiChi	DEEPSOIL	54.83	0.051	0.957	4.3
Kobe	DEEPSOIL	22.585	0.204	0.906	9.4
ChiChi	TCU084	46.641	0.43	0.833	16.7
Kobe	KJMA	29.2	0.196	0.9	10
Use $\gamma_{eff} = 0.65\gamma_{\max}$					
Earthquake	Station	N_c	γ (%)	Softening Index	Percentage decrease (%)
ChiChi	DEEPSOIL	54.83	0.059	0.949	5.1
Kobe	DEEPSOIL	22.585	0.276	0.89	11
ChiChi	TCU084	46.641	067	0.794	20.6
Kobe	KJMA	29.2	0.27	0.88	12

doi:10.6342/NTU202403515

Table 3.14 The calculation results of softening index (use partial shear stress history)

Use $\tau_{avg} = 0.65\tau_{\max}$ then find γ_{eff}					
Earthquake	Station	N_c	γ (%)	Softening Index	Percentage decrease (%)
ChiChi	DEEPSOIL	37.13	0.051	0.961	3.9
Kobe	DEEPSOIL	22.585	0.204	0.906	9.4
ChiChi	TCU084	17.838	0.43	0.872	12.8
Kobe	KJMA	25.8	0.196	0.9	10
Use $\gamma_{eff} = 0.65\gamma_{\max}$					
Earthquake	Station	N_c	γ (%)	Softening Index	Percentage decrease (%)
ChiChi	DEEPSOIL	37.13	0.059	0.954	4.6
Kobe	DEEPSOIL	22.585	0.276	0.89	11
ChiChi	TCU084	17.838	067	0.841	15.9
Kobe	KJMA	25.8	0.27	0.89	11

doi:10.6342/NTU202403515

Chapter 4 Simulation Results and Discussions

4.1 Drag Anchor Model in Clay

In Section 4.1, the numerical simulation results of dragging drag anchor in clay will be presented. The model is divided into simplified model and true model, simulations were conducted using the parameters outlined in Section 3.3.4. The simulation results will be presented in the following subsections.

4.1.1 Simplified Model

In Section 4.1.1, we will present the simulation results for two types of soil parameters: the American Bureau of Shipping (2017) and the BH04 soil parameters. First, we will present the simulation results for the American Bureau of Shipping (2017). Based on the prediction results in Section 3.1.1, we selected depths of 3m, 6m, and 9m for the analysis. The fluke angles at these depths are 24.018, 16.53, and 10.85 degrees, respectively. Simulations were conducted using the parameters outlined in Section 3.3.4.

The simulation results are shown in Figures 4.1 to 4.3. The holding capacity is taken as the average value during the more stable phase at the end of the curve. The comparison of the simulation results and difference for each depth is provided in Table 4.1. As shown in Table 4.1, the difference for the three depths are 12%, 9.4%, and 7.4%, respectively. The similarity between the simulation and predicted results demonstrates the feasibility of this numerical model. Therefore, the same modeling approach will be used for subsequent numerical analyses.

After validating the feasibility of the numerical model, a numerical simulation was conducted using the soil parameters from Table 3.4. The simulation analyzed both the k=0 and k=1.5 cases. The results are shown in Figures 4.5 to 4.7. For the k=1.5 case, the

doi:10.6342/NTU202403515

holding capacity is greater than that of the k=0 case, which is attributed to the higher undrained shear strength in the k=1.5 scenario. The difference for the k=1.5 case is larger than for the k=0 case. The author believes the main reason is that the initial undrained shear strength of the soil layer used was already the average value from in-situ borehole data, which should have already accounted for the depth's influence on undrained shear strength. Adding a k=1.5 variation value on top of this average value results in the simulated values being significantly higher than the predicted values. The simulation results are similar to those of Qiao et al.(2020), with the holding capacity curve divided into three distinct segments. From Figures 4.5 to 4.7, it can be observed that the curve initially shows a linear increase, indicating that the soil has not yet entered the plastic phase. Next, the curve starts to exhibit a nonlinear increase, signifying that the soil is undergoing plastic deformation. Finally, the curve stabilizes, indicating that the soil has reached its ultimate strength. For Figures 4.1 to 4.3, due to the soil's low undrained shear strength, the soil quickly enters the plastic and ultimate states, making these three stages less distinct on the curve.

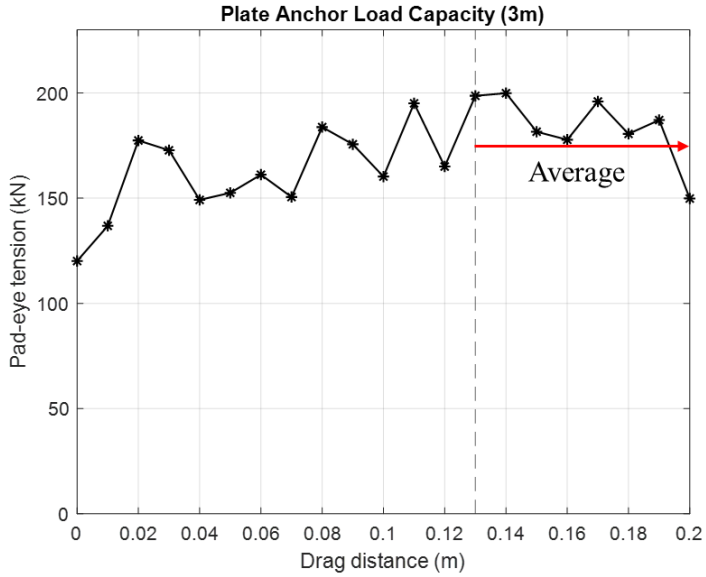

Figure 4. 1 Bearing capacity simulation results for a depth of three meters (ABS)

doi:10.6342/NTU202403515

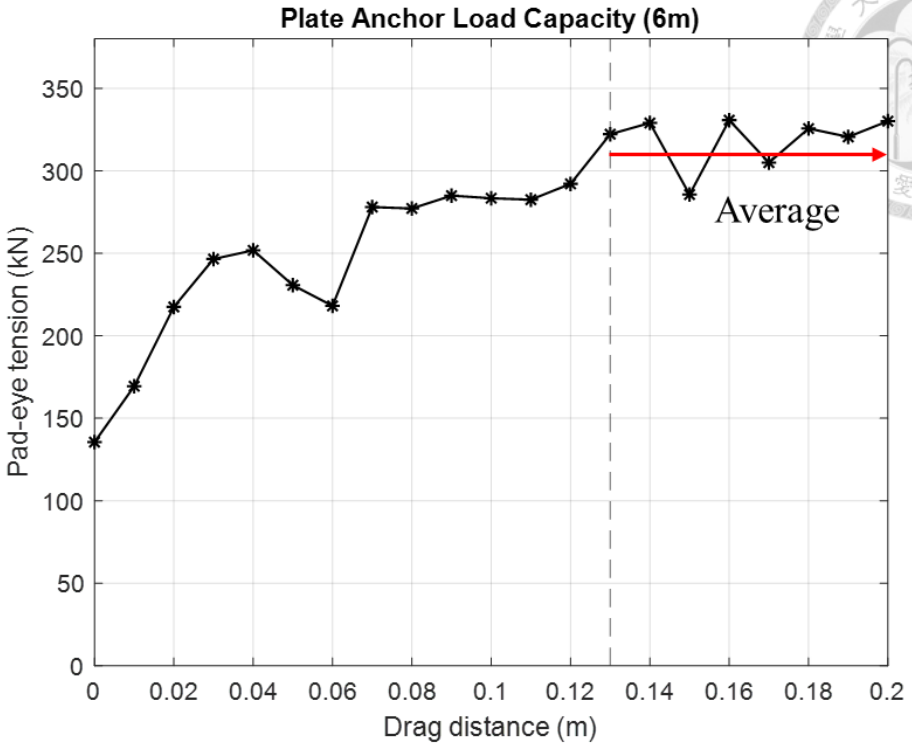

Figure 4. 2 Bearing capacity simulation results for a depth of six meters (ABS)

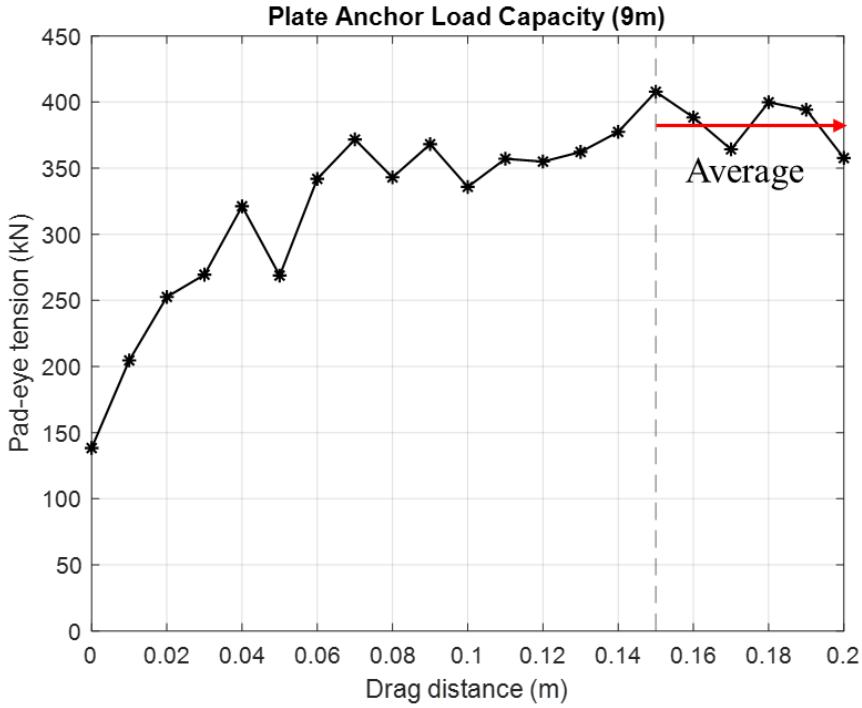

Figure 4. 3 Bearing capacity simulation results for a depth of nine meters (ABS)

doi:10.6342/NTU202403515

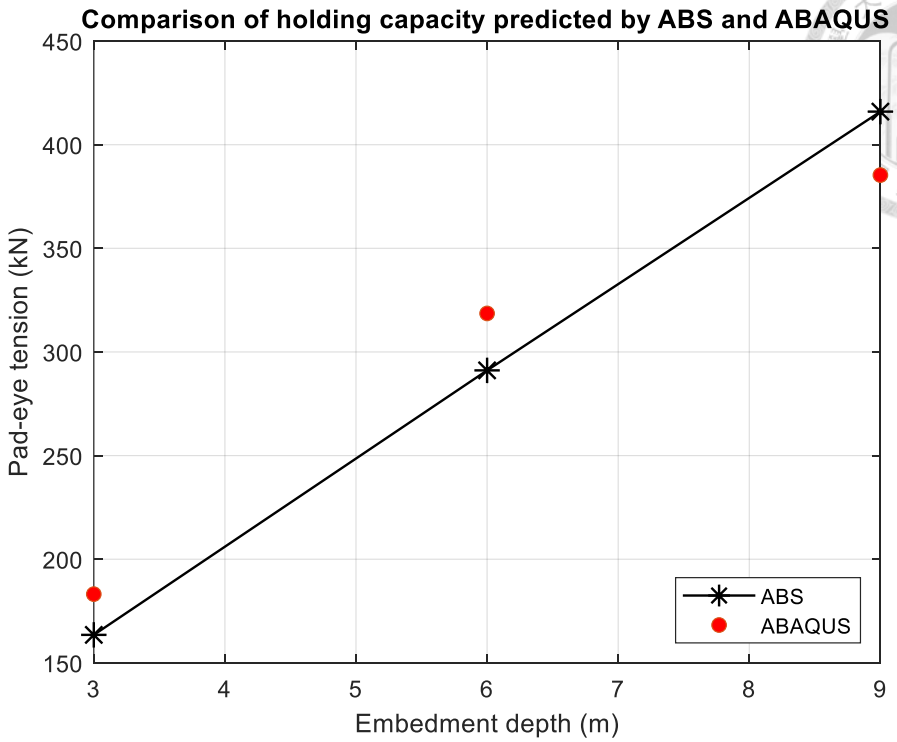

Figure 4. 4 Comparison of holding capacity predicted by ABS and ABAQUS

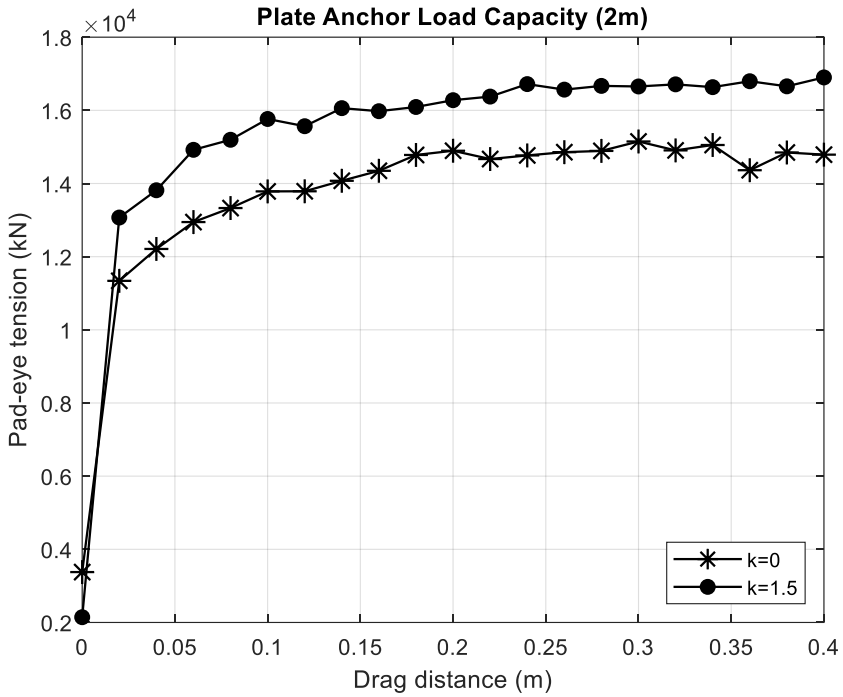

Figure 4. 5 Bearing capacity simulation results for a depth of 2 meters (BH04 4th layer)

doi:10.6342/NTU202403515

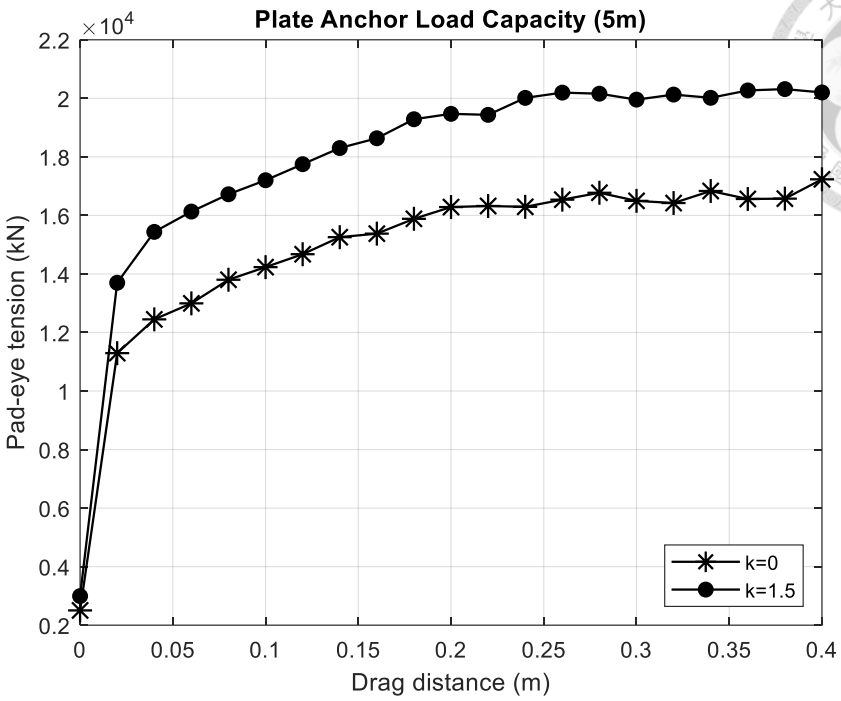

Figure 4. 6 Bearing capacity simulation results for a depth of 5 meters (BH04 4th layer)

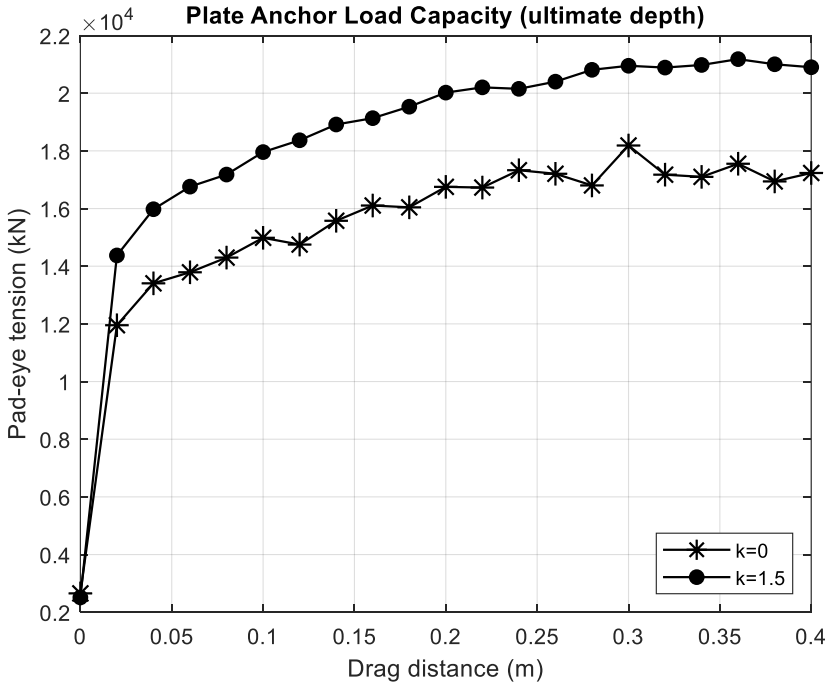

Figure 4. 7 Bearing capacity simulation results for a depth of 7.4 meters (BH04 4th layer)

doi:10.6342/NTU202403515

Table 4.1 Comparison of errors between prediction value and simulation results at different depths

Depth (m)	ABAQUS (kN)	ABS (kN)	Difference (%)
3	183.1475	163.4987	12
6	318.5896	291.1082	9.4
9	385.3339	415.9672	7.4
Depth (m)	Simulation (kN)	Prediction (kN)	Difference (%)
2	14830.68	16628	-
5	16489.43	16628	-
7.4	17224.94	16628	-
Depth (m)	Simulation (kN)	Prediction (kN)	Difference (%)
2	16696.7172	17133	2.5
5	20134.02	17856	14.4
7.73	20965.28	18531	13

4.1.2 True Model

In this section, the simulation results using the true model will be presented. The simulations are conducted using the parameters from Table 3.4, and the results are compared with the simplified model. The simulation results are shown in Figure 4.8. The holding capacity simulated using the True model is 19,961.78 kN, which differs by 15.89% from the simplified model. The author believes that this is because the internal irregularities of the true model provide additional holding capacity, which cannot be effectively accounted for in the simplification process, as shown in Figures 4.9 to 4.11.

doi:10.6342/NTU202403515

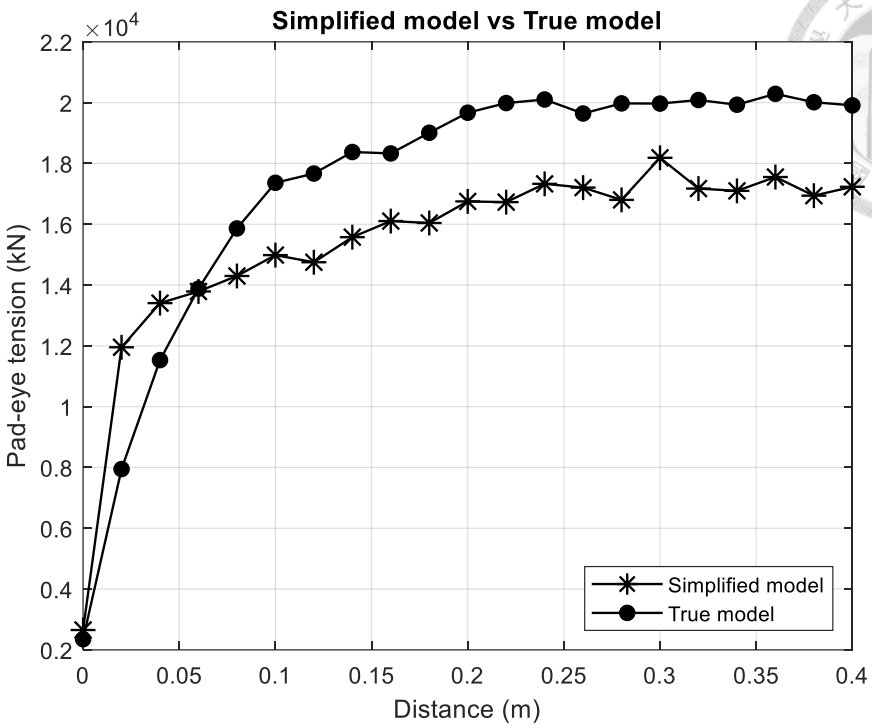

Figure 4. 8 True model and simplified model holding capacity comparison

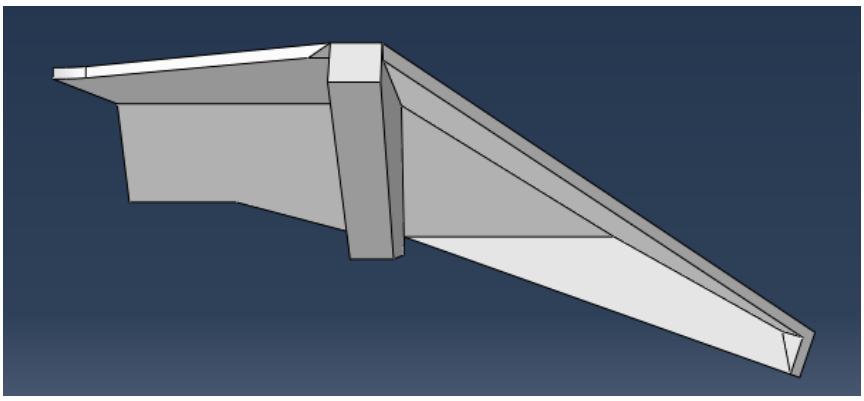

Figure 4. 9 Rear view of the halved true model

doi:10.6342/NTU202403515

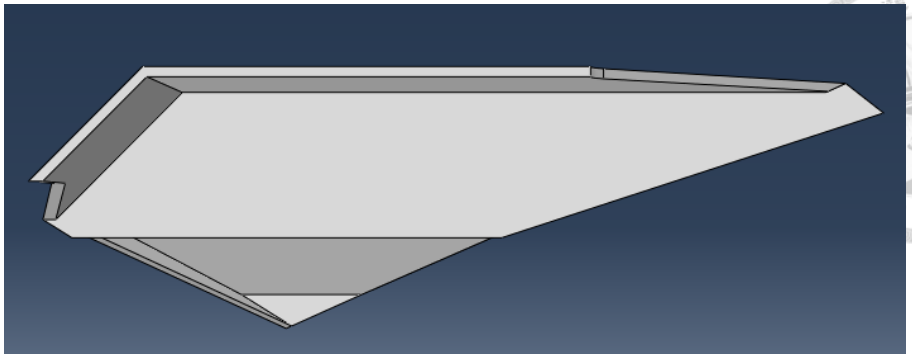

Figure 4. 10 Side view of the halved true model

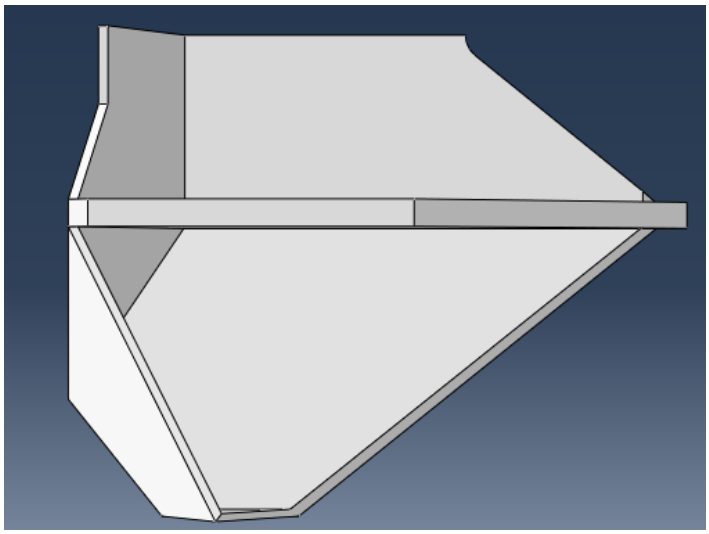

Figure 4. 11 Bottom view of the halved true model

4.2 Drag Anchor Model in Sand

In Section 4.2, the simulation results of the drag anchor in sandy soil will be presented. Unlike Section 4.1, there are no reliable predictive formulas currently available for sandy soils. Therefore, this study will conduct extensive numerical simulations for sandy soils and regress the simulation results into a formula. This subsection will introduce the parameters and sets used in the simulations.

doi:10.6342/NTU202403515

4.2.1 Parameters Used in the Regression Model

The regression model in this study targeted both total stress analysis and effective stress analysis. The difference between the two lies in the soil unit weight used in the simulation: total stress analysis does not subtract the unit weight of water, while effective stress analysis requires the unit weight of water to be subtracted from the unit weight of the sandy soil. In the analysis, the independent variables are depth, friction angle, fluke area, thickness, and fluke angle. The dependent variable is holding capacity. The parameter tables for the two analysis methods are shown in Table 4.2. It should be noted that because the fluke angle changes with depth, the fluke angles in the simulations are fixed at 25, 10, and 0 degrees for depths of 3, 6, and 10 meters, respectively.

Table 4.2 Parameter for two different analysis methods

Analysis	Depth (m)	Friction angle $(^\circ)$	Fluke area (m^2)	Thickness (m)	Fluke angle $(^\circ)$
Total stress	3,6,10	20,23,25,28,30	15,20,25	0.3,0.5,0.7,1,1.2	0,10,25
Effective stress	3,6,10	20,25,30	15,20,25	0.5,0.7,1	0,10,25

4.2.2 Regression analysis method

Before conducting the regression analysis, it is necessary to discuss the relationship between each independent variable and the dependent variable. If each variable has a linear relationship with the dependent variable, linear regression can be used. However, if any independent variable has a nonlinear relationship with the dependent variable, nonlinear regression must be used for the analysis.

doi:10.6342/NTU202403515

The relationship between each independent variable and the holding capacity is shown in Figure 4.12 and Figure 4.13, the complete information is provided in the appendix. It can be observed that when we fix the depth and thickness, the increase in the friction angle and the holding capacity shows a linear trend. Similarly, with the same friction angle, when the fluke area increases, the difference in holding capacity between two different fluke areas is quite close. Therefore, it can be considered that the increase in fluke area has a linear relationship with the holding capacity. When we fix the friction angle and fluke area, the relationship between thickness and holding capacity also exhibits a roughly linear trend. Similarly, with the same depth, when the anchor thickness increases, the difference in holding capacity between two different thicknesses is quite close. Therefore, it can be considered that the increase in thickness has a linear relationship with holding capacity. A similar trend can also be observed in the effective stress analysis.

In summary, this regression analysis will use linear regression. The equation we use is shown in Equation 4.1, Y is the dependent variable, which is the holding capacity. A represents the coefficients of the independent variables. This analysis uses 5 independent variables: X_1 to X_5, which correspond to depth, friction angle, fluke area, thickness, and fluke angle, respectively. A_1 to A_5 are the corresponding coefficients. The results of the regression will be presented in the next section.

$$\ln Y = A_0 + A_1 X_1 + A_2 X_2 + \cdots + A_n X_n \tag{4.1}$$

doi:10.6342/NTU202403515

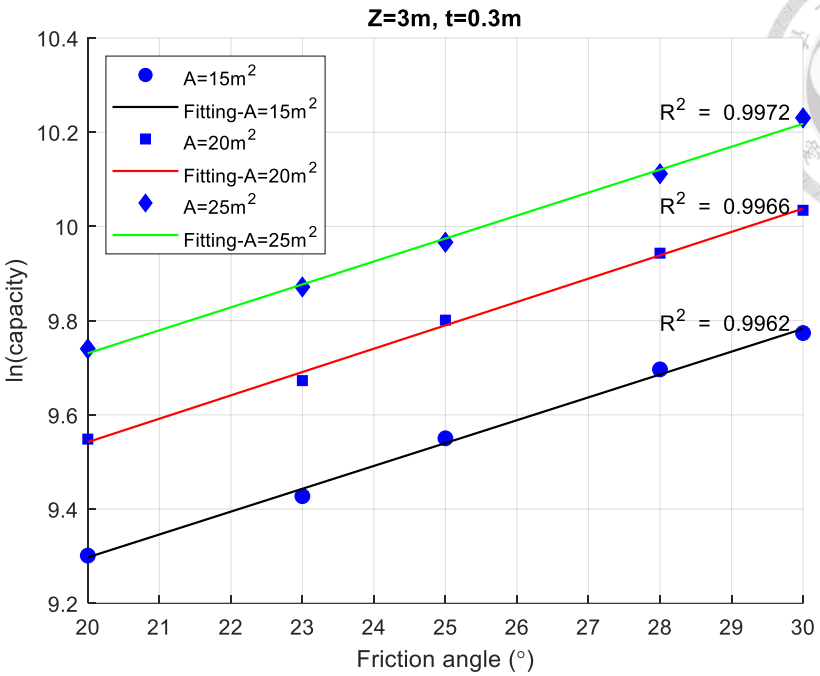

Figure 4. 12 The relationship between holding capacity and parameters (fixed depth and thickness)

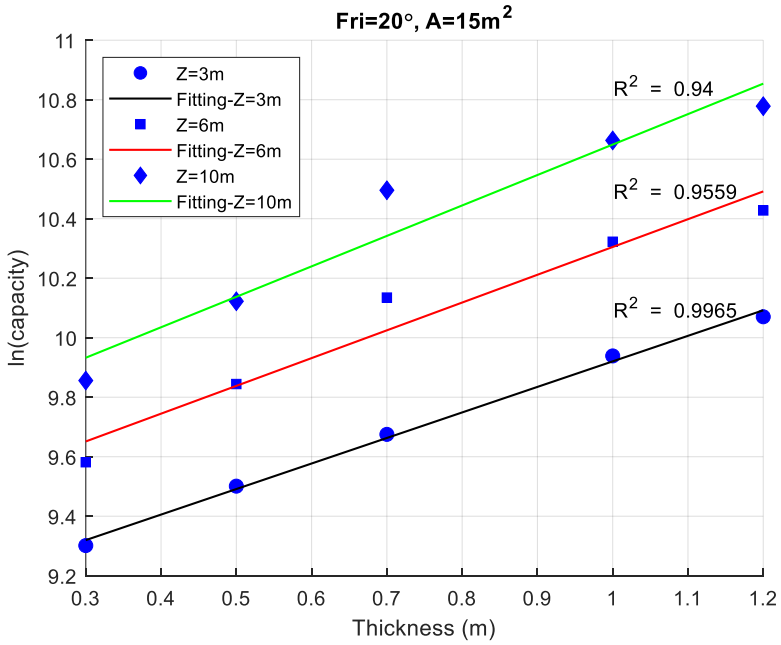

Figure 4. 13 The relationship between holding capacity and parameters (fixed friction angle and fluke area)

doi:10.6342/NTU202403515

4.2.3 Regression Analysis Results

This regression analysis was conducted using the Statistical Product and Service Solutions (SPSS) software developed by IBM. The analysis results are shown in Table 4.3 and Table 4.4. The R-squared values for the total stress analysis and effective stress analysis are 0.97 and 0.982, respectively, indicating a good regression fit. Additionally, the root mean square error (RMSE) values are 5201.71 kN and 2892.79 kN, respectively.

Table 4.3 Regression results of the two analysis methods

Analysis	R^2	A_0	A_1	A_2	A_3	A_4	A_5
Total stress	0.97	4.432	0.359	0.064	0.035	0.887	0.069
Effective stress	0.982	6.645	0.138	0.064	0.032	0.757	0.009

Table 4.4 The RMSE of the two analysis methods

Analysis	RMSE (kN)
Total stress	5201.71
Effective stress	2892.79

4.3 Earthquake Analysis

4.3.1 Contact Force During Seismic Loading

After the anchor dragging process is completed, a seismic time history is applied at the base of the model to conduct dynamic analysis and observe the changes in the contact forces between the anchor and the surrounding soil. The seismic time history used and the holding capacity during the seismic stage are shown in Figure 4.14 and Figure 4.15. The earthquake used in the analysis is the Kobe earthquake, with a duration of 47.98 seconds. As shown in Figure 4.15, the contact force between the anchor and the

doi:10.6342/NTU202403515

surrounding soil drops sharply upon the occurrence of the earthquake, decreasing to a level comparable to the pre-earthquake equilibrium state. This is because the anchor is not continuously penetrating the soil, making it impossible to measure the soil resistance applied to the anchor. According to Zhao and Liu (2016), Dou and Yu (2018), and Qiao et al.(2020), to measure the holding capacity of a drag anchor during dragging, soil resistance against the anchor needs to be stimulated by displacement. On the other hand, as per the American Bureau of Shipping (2017), once a drag anchor is installed, it can provide holding capacity equivalent to the installation pull force without requiring further penetration. Therefore, it is understood that the holding capacity of a drag anchor can only be measured during the dragging phase. After dragging is completed, the contact resistance on the anchor does not represent the holding capacity in that state.

Based on the above discussion, there is currently no method available to measure the holding capacity provided by a drag anchor during seismic events. Subsequent chapters will introduce approaches to assess the decrease in bearing capacity caused by seismic events post-seismic activity.

doi:10.6342/NTU202403515

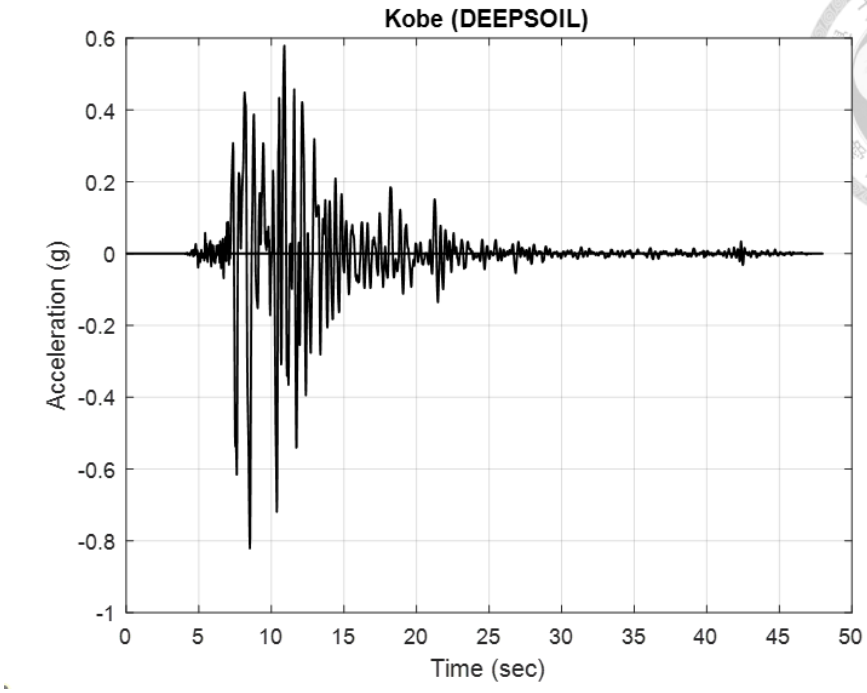

Figure 4. 14 Input motion at the base of the model (DEEPSOIL)

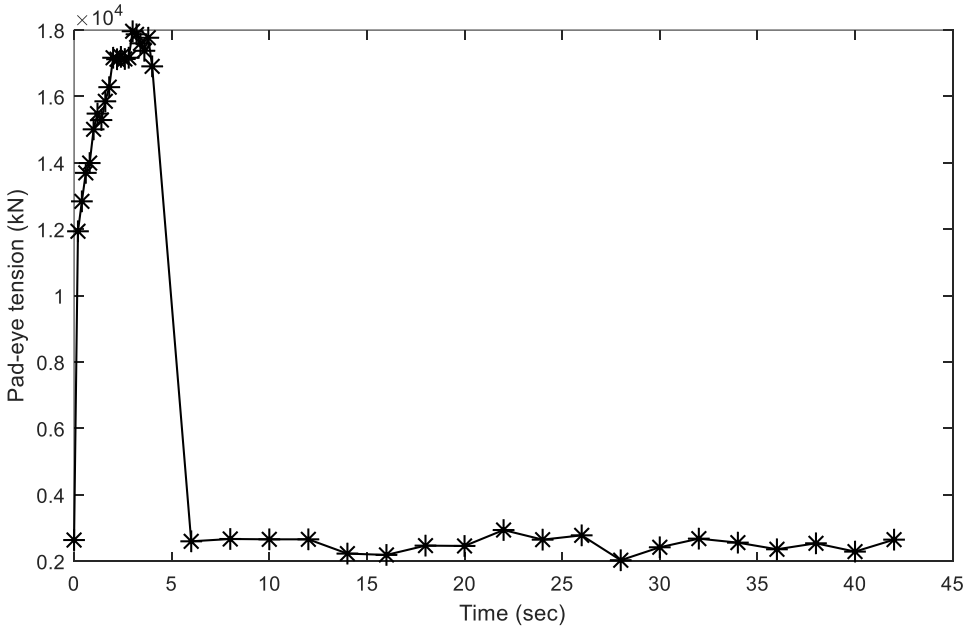

Figure 4. 15 Variations in contact force during the drag anchor stage and the earthquake stage

doi:10.6342/NTU202403515

4.4 Capacity Simulation After Cyclic Softening

4.4.1 Holding Capacity After Seismic Loading

According to the results of Section 3.4.1, the undrained shear strength is multiplied by the softening index, and then the drag anchor simulation is performed again. The simulation results are shown in Figure 4.16 to Figure 4.19 and Table 4.2.

When using DEEPSOIL 's input motions for calculations, the softening index for the ChiChi earthquake and the Kobe earthquake were 0.97 and 0.91, respectively. After reduction, the holding capacity was 17,149.78 kN and 16438.06 kN, respectively, differing by 0.45% and 4.6% from the original holding capacity of 17,224.94 kN. When using input motions from the PEER database for calculations, the softening index for the ChiChi earthquake and the Kobe earthquake were 0.851 and 0.9, respectively. After reduction, the holding capacity was 15638.86 kN and 16427.10 kN, respectively, differing by 9.2% and 4.6% from the original holding capacity of 17,224.94 kN. Due to the varying earthquake records at each station, the results for the softening index calculations differ. It can be observed that the primary factor affecting the softening index is the magnitude of the PGA. Therefore, in future site-specific analyses, it is essential to consider the influence of different stations.

After examining the impact of different station records and PGA on the results, we also investigated the effect of earthquakes with different periods on the softening index under the same PSA. The response spectra for these analyses are shown in Figures 3.53 and 3.54. Tables 4.3 and 4.4 present the calculation of the softening index for earthquakes with different periods, where the ChiChi and Kocaeli earthquakes represent long and short periods respectively. According to the results, under similar earthquake magnitudes (ChiChi = 7.7, Kocaeli = 7.6), the reduction in strength for short-period earthquakes is

doi:10.6342/NTU202403515

less than that for long-period earthquakes at the same PSA levels. The author believes this is because short-period earthquakes have shorter wavelengths, resulting in lower energy, whereas long-period earthquakes have longer wavelengths and higher energy. Therefore, the energy dissipation as the seismic waves reach the surface varies, as shown in Figure 3.53 and 3.54, leading to different PGA values and indirectly affecting the decrease in soil strength.

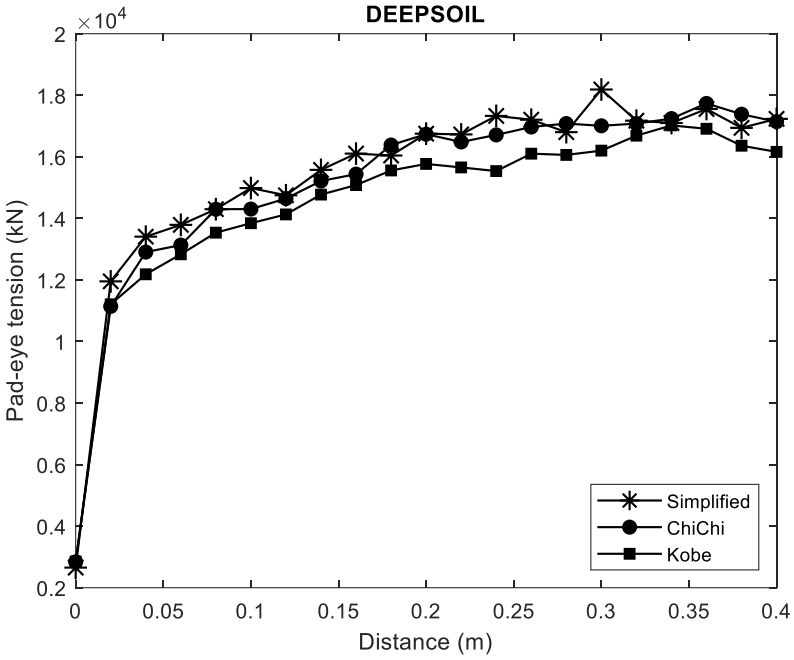

Figure 4. 16 Holding capacity after cyclic softening (ground motions from DEEPSOIL)

doi:10.6342/NTU202403515

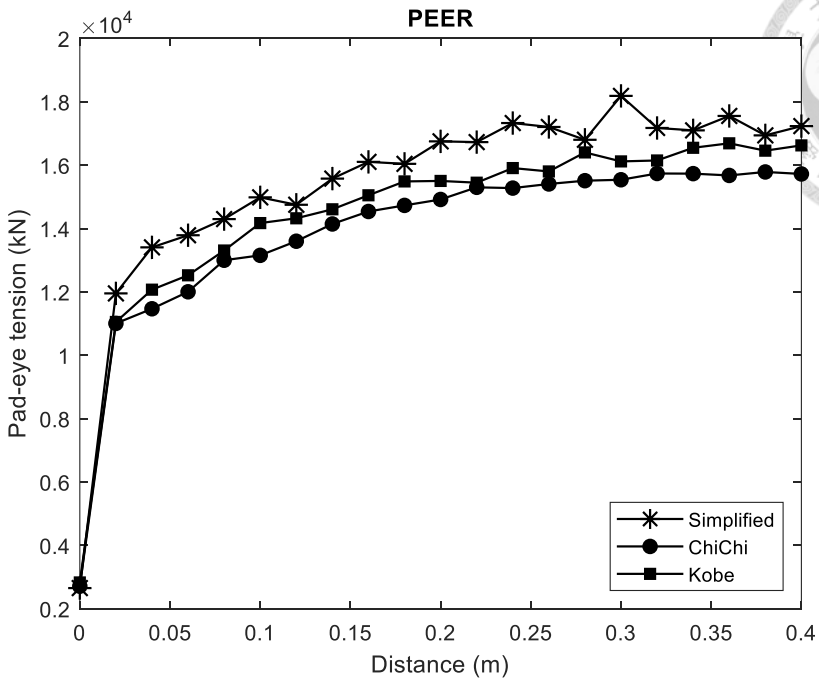

Figure 4. 17 Holding capacity after cyclic softening (ground motions from PEER)

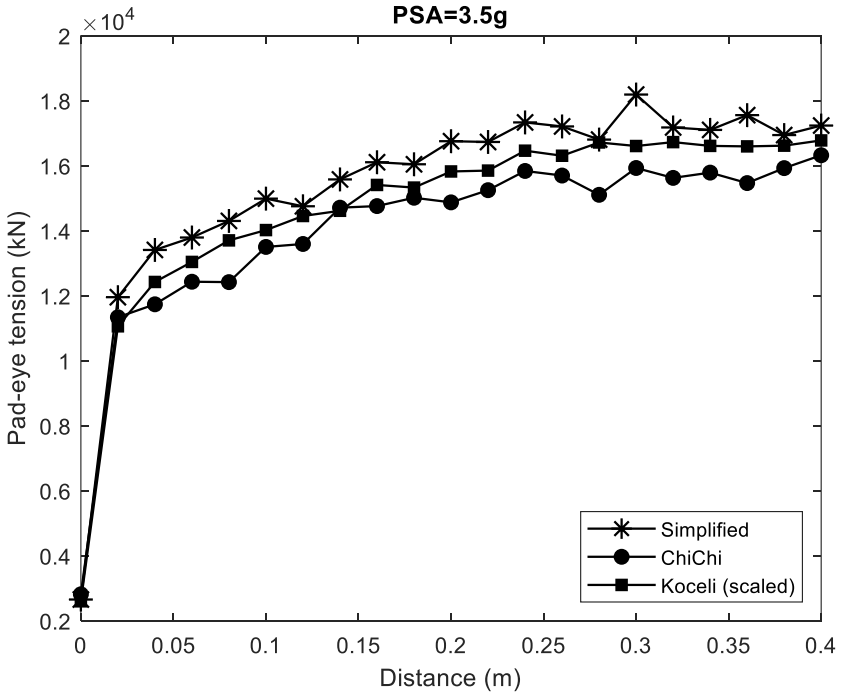

Figure 4. 18 Holding capacity after cyclic softening (PSA=3.5g)

doi:10.6342/NTU202403515

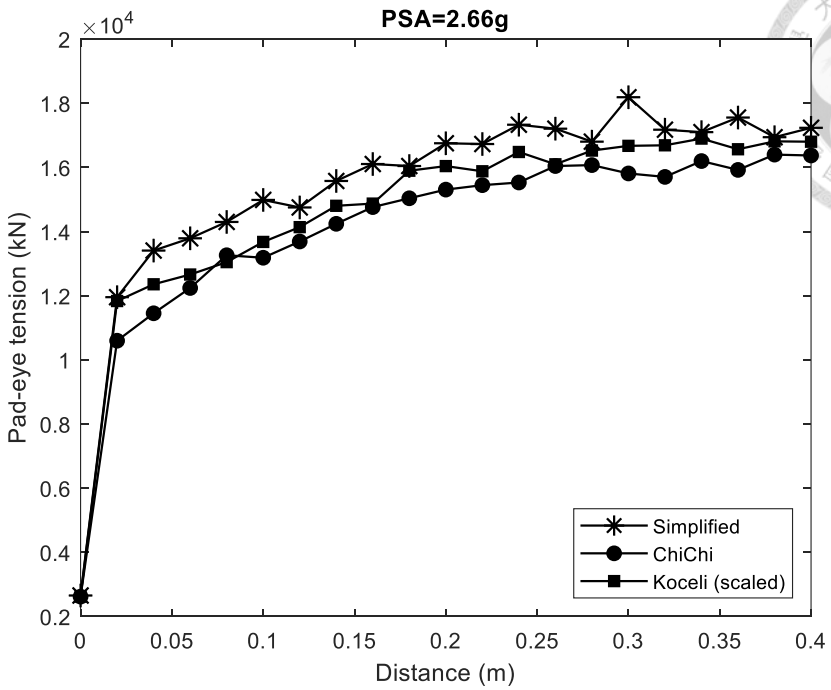

Figure 4. 19 Holding capacity after cyclic softening (PSA=2.66g)

Table 4.2 Cyclic softening evaluation results

Earthquake	station	Undrained shear strength after cyclic softening (kPa)	Holding capacity after cyclic softening (kN)	Capacity decrease (%)
ChiChi	DEEPSOIL	98.36	17149.78	0.45
Kobe	DEEPSOIL	92.27	16438.06	4.6
ChiChi	TCU084	86.29	15638.86	9.2
Kobe	KJMA	91.26	16427.10	4.6

doi:10.6342/NTU202403515

Table 4.3 Comparison of the softening index for earthquakes with different periods (PSA=3.5g)

Earthquake	PGA (g)	Undrained shear strength after cyclic softening (kPa)	Holding capacity after cyclic softening (kN)	Capacity decrease (%)
ChiChi (TCU084)	0.514	86.29	15638.86	9.2
Kocaeli (scaled)	0.311	93	16661.06	3.3

Table 4.4 Comparison of the softening index for earthquakes with different periods (PSA=2.66g)

Earthquake	PGA (g)	Undrained shear strength after cyclic softening (kPa)	Holding capacity after cyclic softening (kN)	Capacity decrease (%)
ChiChi (scaled)	0.458	88.22	16063.64	6.7
Kocaeli (scaled)	0.290	94.30	16707.66	3

doi:10.6342/NTU202403515

Chapter 5 Conclusions and Recommendations

5.1 Conclusions

This study follows the design process proposed by the American Bureau of Shipping (2017) to reconstruct the drag embedment anchor's dragging trajectory in clay seabed and develop a numerical model to predict the holding capacity under various soil conditions and drag anchor states. For sandy seabed, regression analysis was used to propose empirical formulas for predicting holding capacity. In subsequent seismic analyses, the effects of earthquakes on clay strength and holding capacity were examined. Based on the results of the aforementioned analyses, the conclusions of this study are summarized.

5.1.1 Drag Anchor analysis

1. The numerical model developed in this study shows difference within 15% compared to the theoretical solutions provided by ABS and the soil from BH04 borehole. The prediction results are satisfactory,
2. The simulation results show a 15.89% difference between the simplified model and the real model's holding capacity. This difference primarily arises from the difference in contact area between the anchor and the soil. The true model, compared to the simplified one, has more contact surface that provides additional contact force, resulting in a higher holding capacity in the real model.
3. For soil where the average undrained shear strength has already been used, it is not appropriate to further consider the variation of undrained shear strength with depth. This is because the average value already takes into account the average strength over the soil layer's thickness. Including this additional variation would increase the discrepancy between the simulated and predicted values.

doi:10.6342/NTU202403515

4. Based on the existing drag anchor results in sandy soil, the R square values for the simulated and predicted values under two different analysis methods, total stress analysis and effective stress analysis, are 0.97 and 0.982 respectively, This model allows the user to use simple parameters (depth, friction angle, fluke area, thickness, fluke angle) to do future design without trajectory prediction and numerical simulation.

5.1.2 Seismic Analysis

1. The N_c value calculated using empirical formulas is smaller than the value obtained from using the entire shear stress history. The author believes the difference is because the empirical formulas do not take into account the cumulative peak values from the entire history. Instead, they rely directly on surface seismic information, such as PGA, M_w, and surface response spectra, without considering the effects of the entire earthquake duration.
2. The N_c value calculated using only a portion of the shear stress history will be smaller than that calculated using the entire history, because the total accumulated peak values in the full history will be greater than those in a partial history.
3. The method proposed by Tsai et al. (2014) is based on calculations without performing ground response analysis, using only the seismic parameters obtained at the surface. If ground response analysis is conducted, N_c and γ_{eff} values can be directly calculated as described in Section 3.4.3. The results show that the reduction amounts obtained by the two methods are similar. Additionally, the reduction amounts from the method proposed by Tsai et al. (2014) are generally smaller, which can lead to less conservative results in design.

doi:10.6342/NTU202403515

4. Use γ_{eff} obtained by comparing τ_{avg} with the stress-strain curve at the target depth is smaller than the value obtained by directly using $0.65\gamma_{\max}$. The reduction factors obtained using the latter method are larger compared to the former. Therefore, for design purposes, this method will yield more conservative results.
5. The impact of earthquakes on holding capacity is mainly influenced by the magnitude of the PGA. Earthquakes with higher PGA result in a greater reduction in holding capacity compared to those with lower PGA.
6. Effects of ground motion period and ground motion duration may have some influence on the soil strength degradation but the effect may be minor.

5.2 Recommendations for Future Studies

1. In this study the mk6 model was simplified as a plate model which is based on Qiao er al. (2020), in future research other simplification method should develop
2. This study did not reconstruct the drag anchor's trajectory model in sand, hence it was unable to compare simulation results with theoretical solutions. Therefore, for future research, it is recommended to investigate the behavior of drag anchors in sand to facilitate the development of subsequent model constructions.
3. In the current analysis methods, due to convergence difficulties, it is impossible to directly simulate the drag anchor analysis in a water-saturated environment. Therefore, the effective stress analysis is conducted by adjusting the unit weight. In future research, performing water-soil coupling to more accurately simulate effective stress analysis is also a potential research direction.
4. This study did not conduct experiments for verification. Therefore, future work could involve conducting scaled experiments to validate the accuracy of this study's findings.

doi:10.6342/NTU202403515

REFERENCES

1. ABAQUS (2022) Analysis User's Manual (v6.14). Dassault Systems Simulia Inc.
2. American Bureau of Shipping. (2017). Guidance Notes on Design and Installation of Drag Anchors and Plate Anchors.
3. Anastasopoulos, I., Gelagoti, F., Kourkoulis, R., & Gazetas, G. (2011). Simplified Constitutive Model for Simulation of Cyclic Response of Shallow Foundations: Validation against Laboratory Tests. Journal of Geotechnical and Geoenvironmental Engineering, 137(12), 1154–1168.
4. Aubeny, C., and Chi, C.-M. (2014). Analytical Model for Vertically Loaded Anchor Performance. Journal of Geotechnical and Geoenvironmental Engineering, 140(1), 14–24.
5. Aubeny, C. P., and Chi, C. (2010). Mechanics of Drag Embedment Anchors in a Soft Seabed. Journal of Geotechnical and Geoenvironmental Engineering, 136(1), 57–68.
6. Darendeli, M. B. (2001). Development of a new family of normalized modulus reduction and material damping curves. The university of Texas at Austin.
7. Dou, Y., and Yu, L. (2018). Numerical investigations of the effects of different design angles on the motion behaviour of drag anchors. Applied Ocean Research, 76, 199–210.
8. Halama, R., Sedlk, J., and Ofer, M. (2012). Phenomenological Modelling of Cyclic Plasticity. In P. Miidla (Ed.), Numerical Modelling. InTech.
9. Kishida, T., & Tsai, C.-C. (2014). Seismic Demand of the Liquefaction Potential with Equivalent Number of Cycles for Probabilistic Seismic Hazard Analysis. Journal of Geotechnical and Geoenvironmental Engineering, 140(3), 04013023.

doi:10.6342/NTU202403515

10. Kuhlemeyer, R. L., and Lysmer, J. (1973). Finite Element Method Accuracy for Wave Propagation Problems. Journal of the Soil Mechanics and Foundations Division, 99(5), 421–427.
11. Liu, H., Zhang, W., Liu, C., and Hu, C. (2012). Movement direction of drag anchors in seabed soils. Applied Ocean Research, 34, 78–95.
12. Mucciacciaro, M., and Sica, S. (2018). Nonlinear soil and pile behaviour on kinematic bending response of flexible piles. Soil Dynamics and Earthquake Engineering, 107, 195–213.
13. Murff, J. D. (1994). Limit analysis of multi-footing foundation systems. Proc. of the 8th Int. Conf. on Computer Methods and Advances in Geomechanics, 1, 223–244.
14. Murff, J. D., Randolph, M. F., Elkhatib, S., Kolk, H. J., Ruinen, R., Strom, P. J., and Thorne, C. (2005). Vertically loaded plate anchors for deepwater applications. Proc., Int. Symp. on Frontiers in Offshore Geotechnics, IS-FOG05, 31–48.
15. Neubecker, S. R., and Randolph, M. F. (1995). Profile and Frictional Capacity of Embedded Anchor Chains. Journal of Geotechnical Engineering, 121(11), 797–803.
16. O'Neill, M. P., Bransby, M. F., and Randolph, M. F. (2003). Drag anchor flukesoil interaction in clays. Canadian Geotechnical Journal, 40(1), 78–94.
17. Peng, J., and Liu, H. (2019). Analytical study on comprehensive behaviors of drag anchors in the seabed. Applied Ocean Research, 90, 101855.
18. Peng, J., Liu, H., Liang, K., and Xiao, Z. (2021). A theoretical model for analyzing the behavior of drag anchors in layered soils. Ocean Engineering, 222, 108568.
19. Qiao, D., Guan, B., Liang, H., Ning, D., Li, B., and Ou, J. (2020). An Improved Method of Predicting Drag Anchor Trajectory Based on the Finite Element Analyses of Holding Capacity. China Ocean Engineering, 34(1), 1–9.

doi:10.6342/NTU202403515

20. Ruinen, R. M. (2004). Penetration analysis of drag embedment anchors in soft clays. ISOPE International Ocean and Polar Engineering Conference, ISOPE-I.
21. Seed, R. B., Cetin, K. O., Moss, R. E. S., Kammerer, A. M., Wu, J., Pestana, J. M., Riemer, M. F., Sancio, R. B., Bray, J. D., Kayen, R. E., and Faris, A. (2003). Recent Advances in Soil Liquefaction Engineering: A Unified and Consistent Framework.
22. Soleimanian, N., Bazaz, J. B., Akhtarpour, A., and Garivani, S. (2023). Effects of constitutive soil models on the seismic response of an offshore jacket platform in clay by considering pile-soil-structure interaction. Soil Dynamics and Earthquake Engineering, 174, 108165.
23. Tsai, C.-C., Mejia, L. H., and Meymand, P. (2014). A strain-based procedure to estimate strength softening in saturated clays during earthquakes. Soil Dynamics and Earthquake Engineering, 66, 191–198.
24. Vucetic, M., and Dobry, R. (1991). Effect of Soil Plasticity on Cyclic Response. Journal of Geotechnical Engineering, 117(1), 89–107.
25. Zhang, J., Cheng, W., Cheng, X., Wang, P., and Wang, T. (2021). Seismic responses analysis of suction bucket foundation for offshore wind turbine in clays. Ocean Engineering, 232, 109159.
26. Zhao, Y., and Liu, H. (2014). Numerical simulation of drag anchor installation by a large deformation finite element technique. International Conference on Offshore Mechanics and Arctic Engineering, 45411, V003T10A011.
27. Zhao, Y., and Liu, H. (2016). Numerical implementation of the installation/mooring line and application to analyzing comprehensive anchor behaviors. Applied Ocean Research, 54, 101–114.
28. 台灣電力公司 (2018)。 離岸風力發電第二期計畫可行性研究。

doi:10.6342/NTU202403515

29. 蘇仁偉 (2021)。 岩石隧道受震反應：現地監測資料解析與三維數值模擬，國立臺灣大學土木工程學系學位論文。

doi:10.6342/NTU202403515

Appendix A: Total Stress Analysis

Fix Depth and Thickness

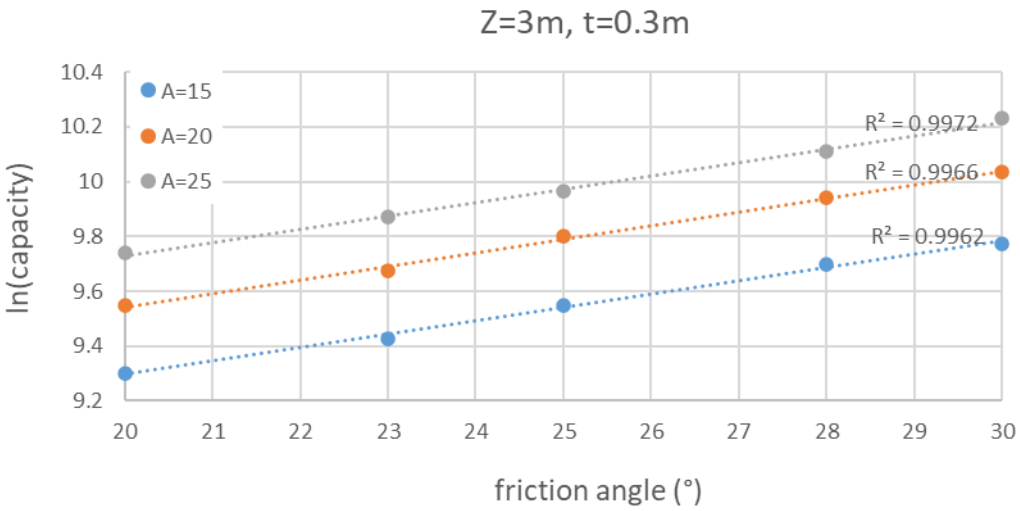

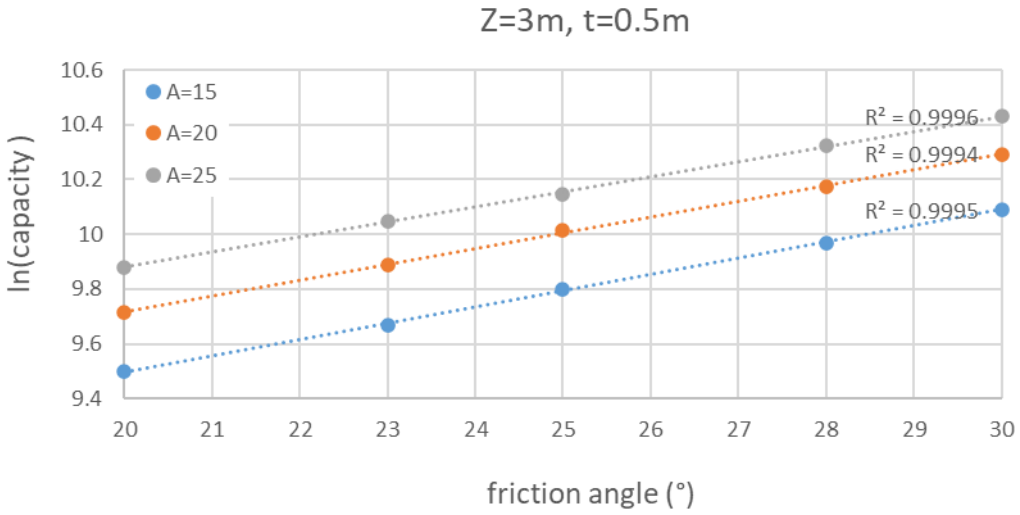

doi:10.6342/NTU202403515

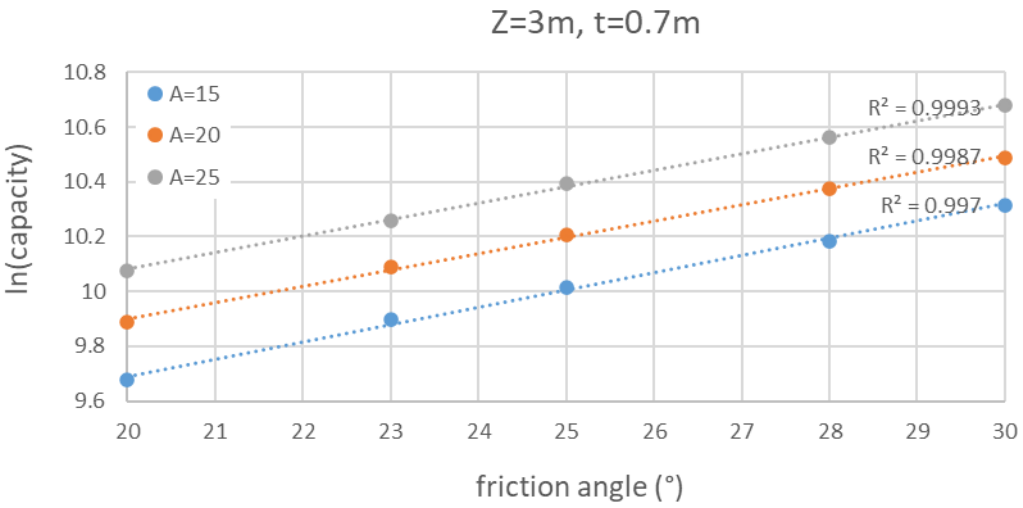

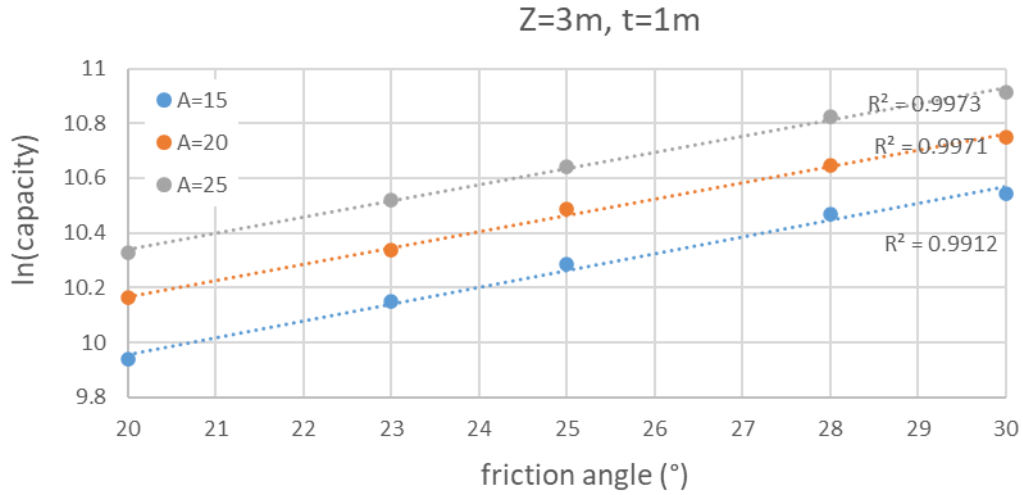

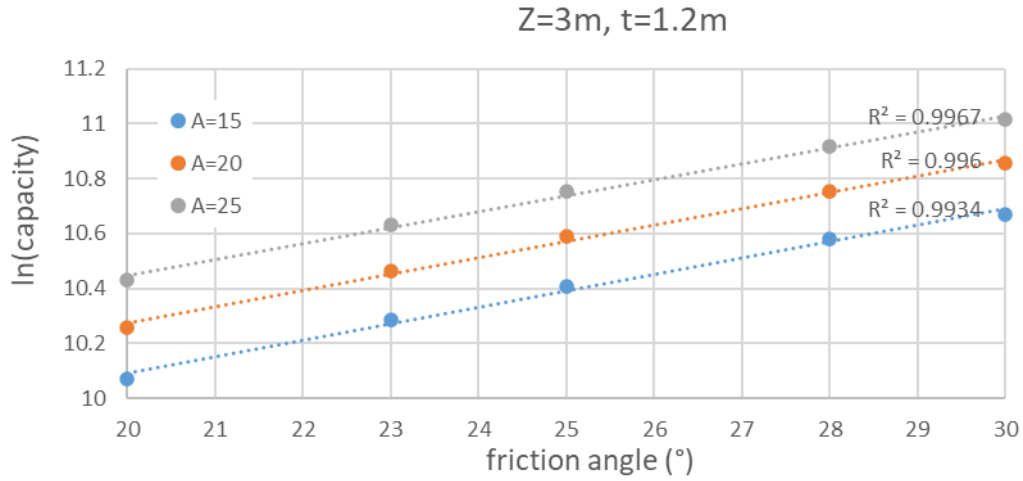

doi:10.6342/NTU202403515

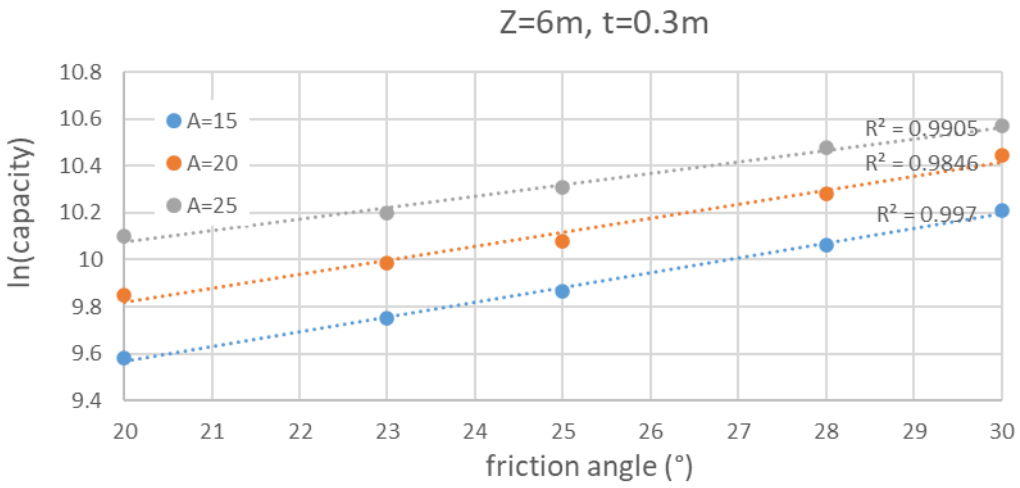

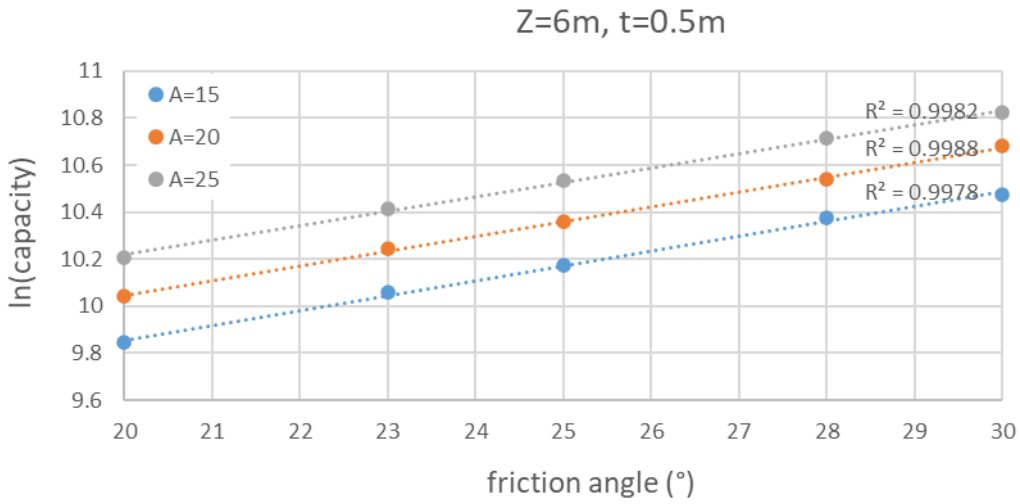

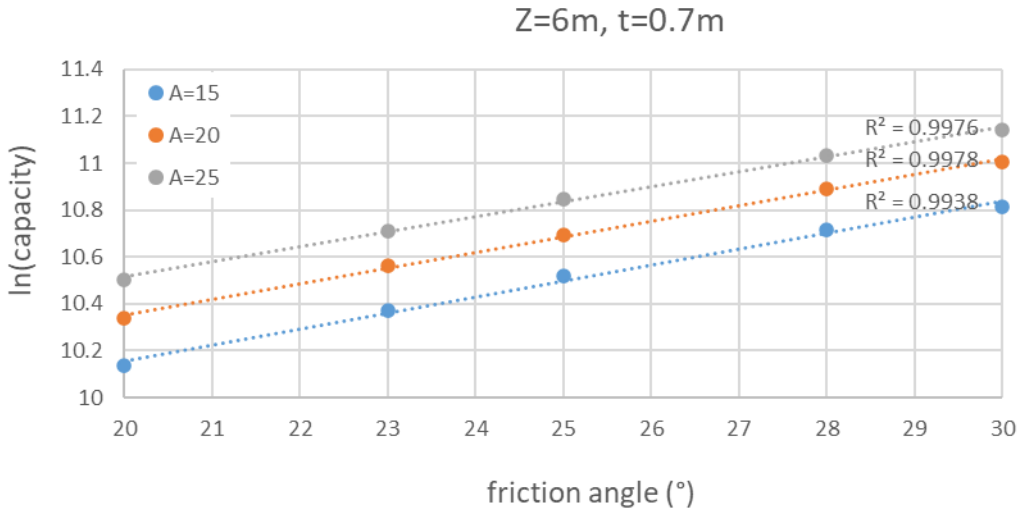

doi:10.6342/NTU202403515

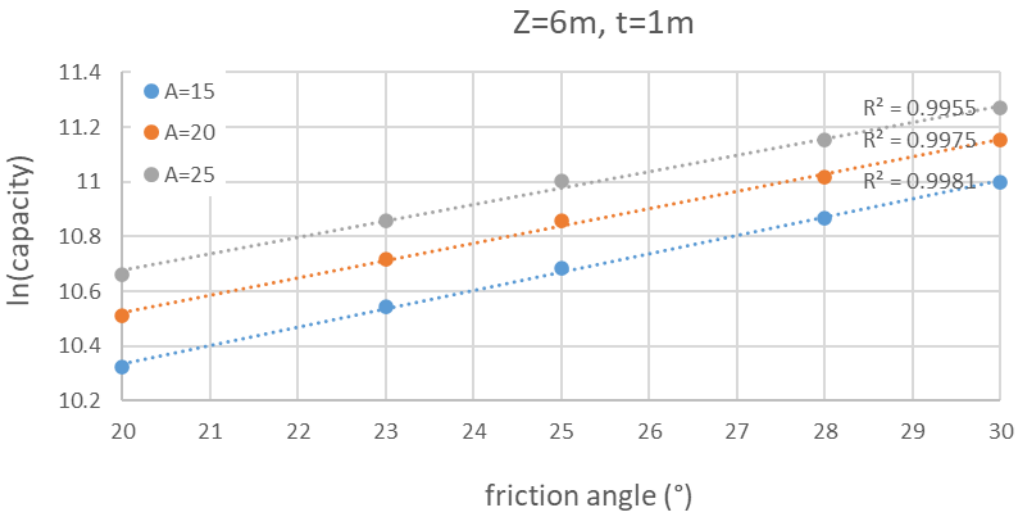

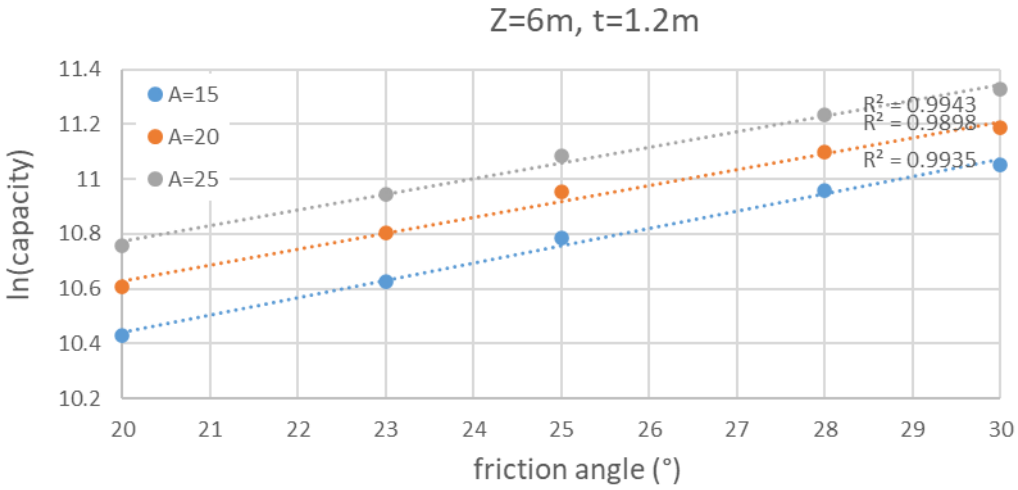

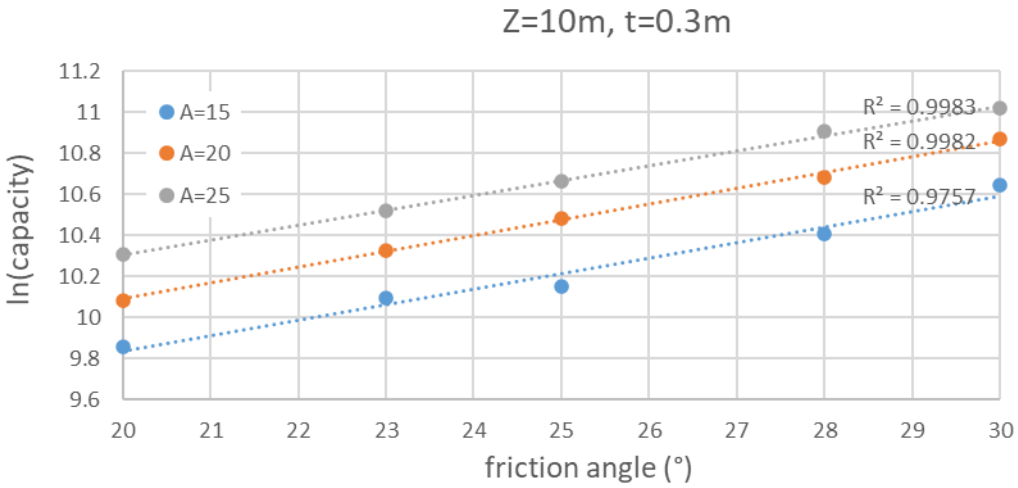

doi:10.6342/NTU202403515

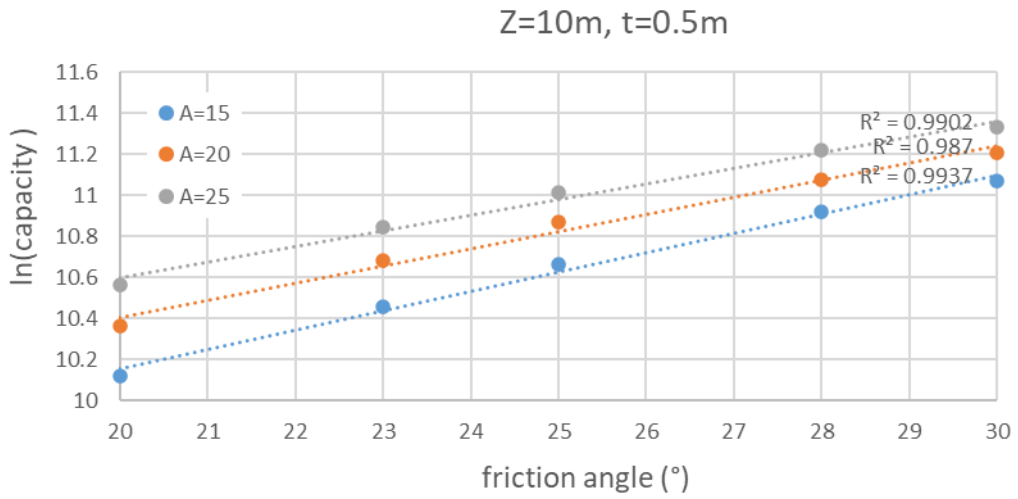

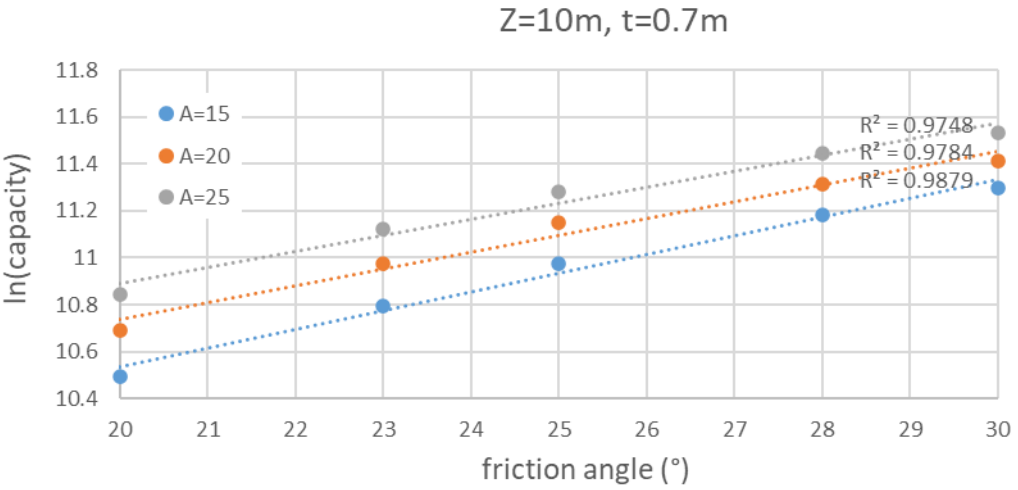

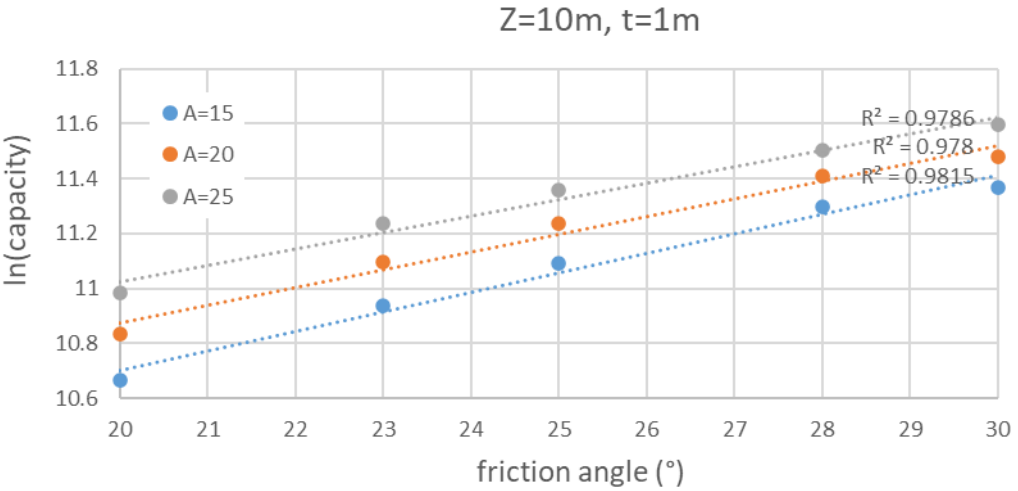

doi:10.6342/NTU202403515

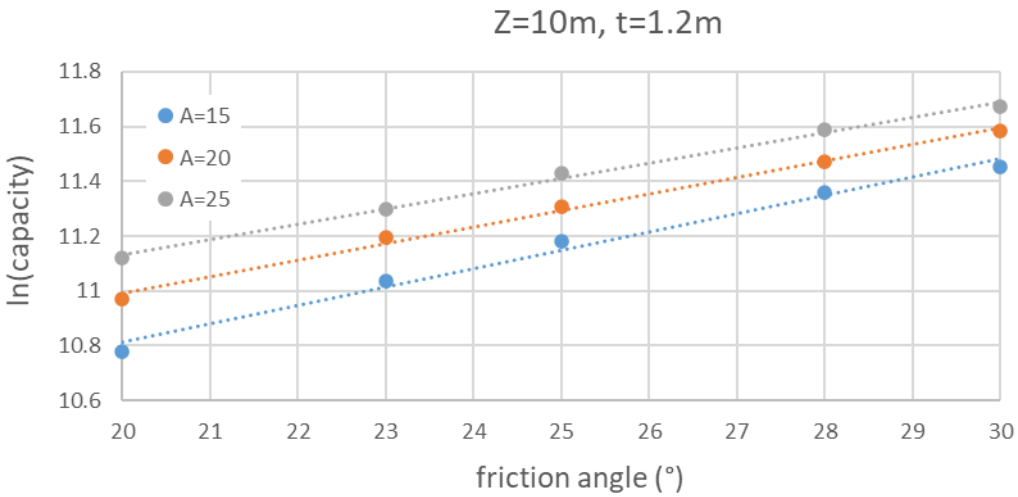

doi:10.6342/NTU202403515

Fix Friction Angle and Fluke Area

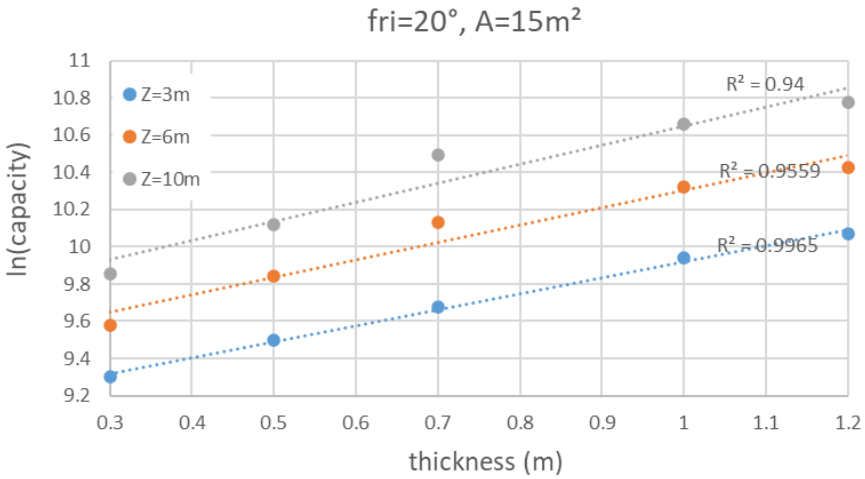

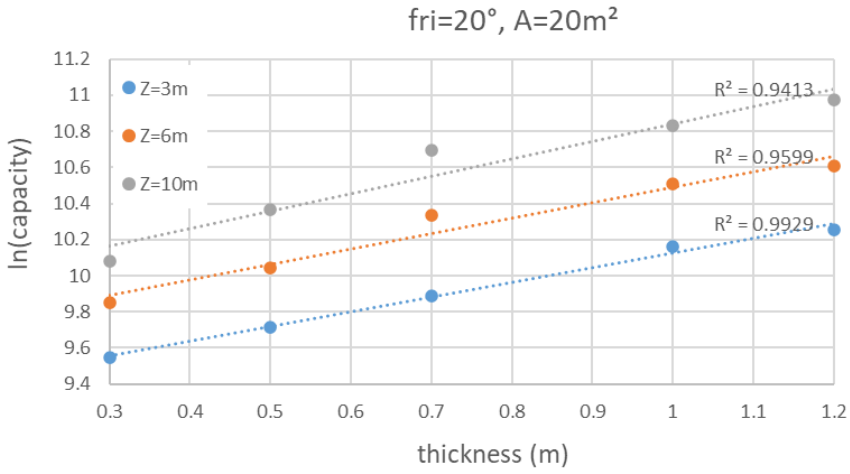

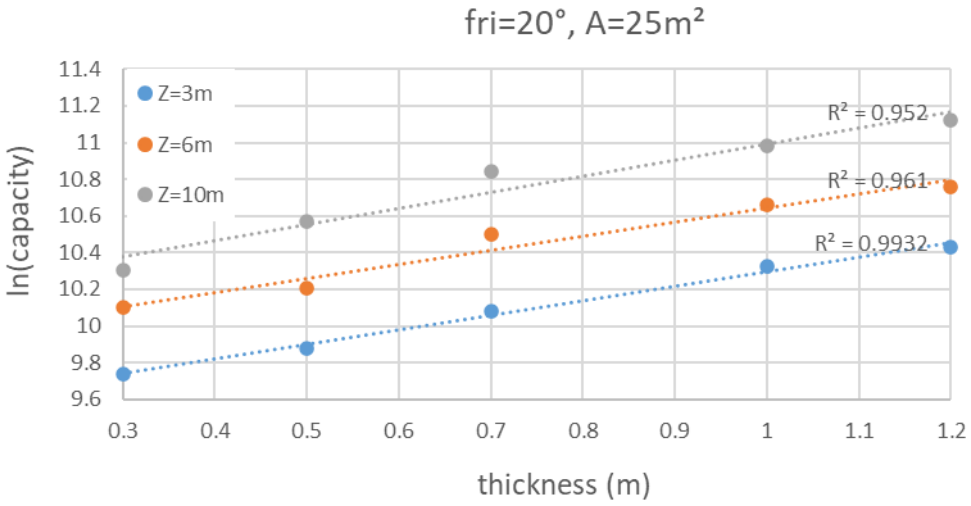

doi:10.6342/NTU202403515

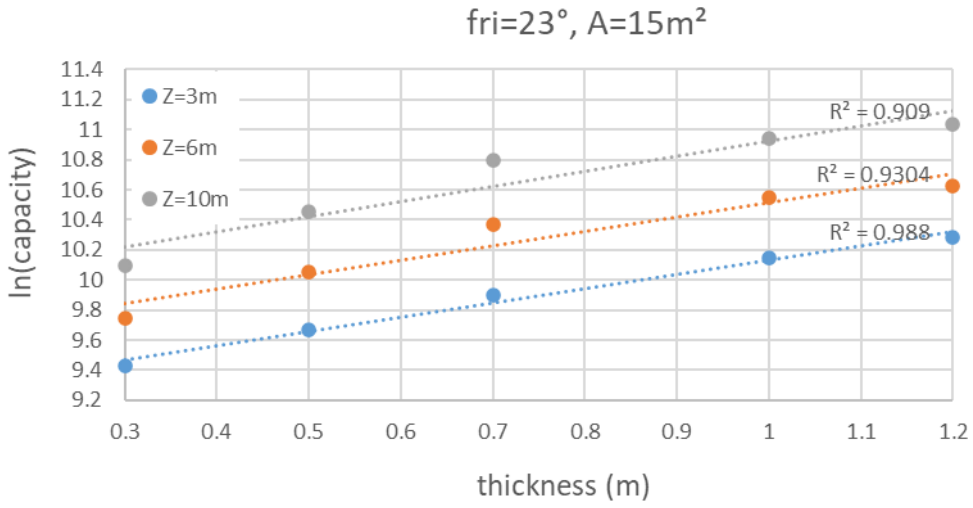

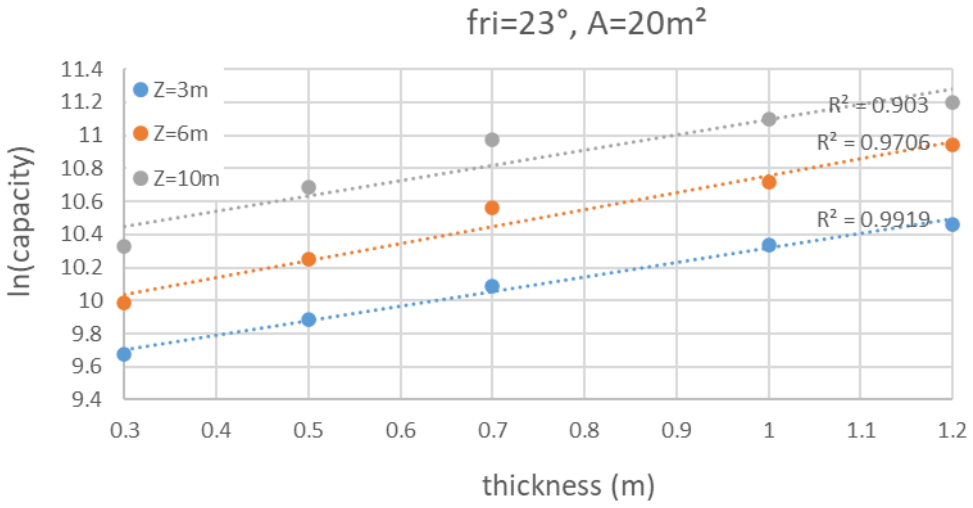

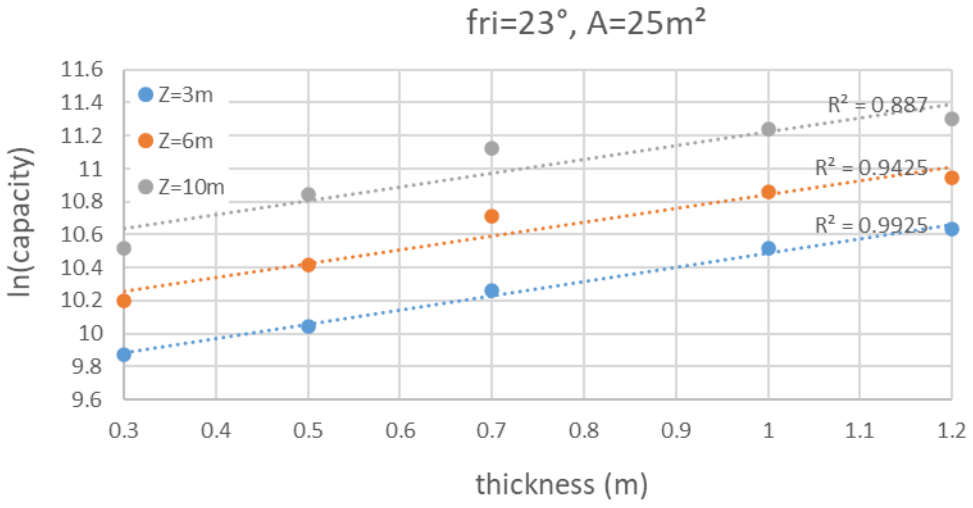

doi:10.6342/NTU202403515

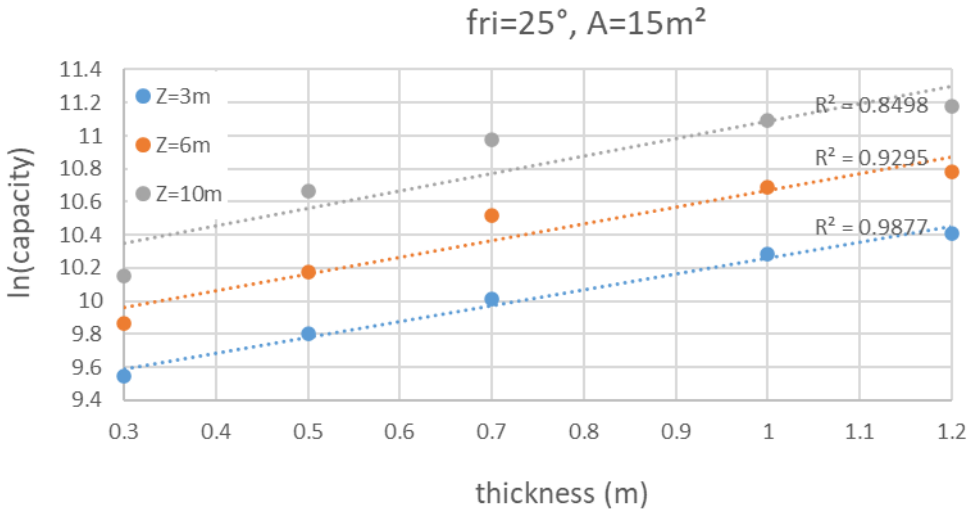

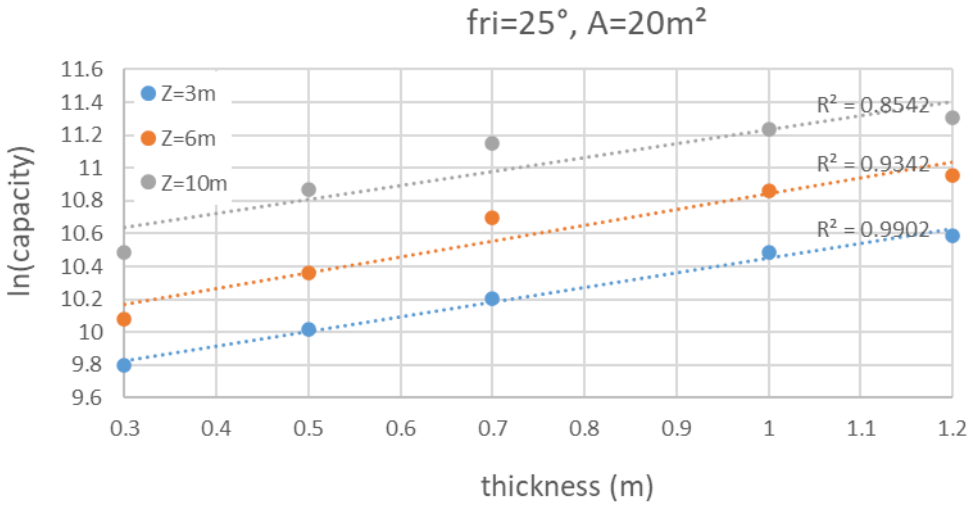

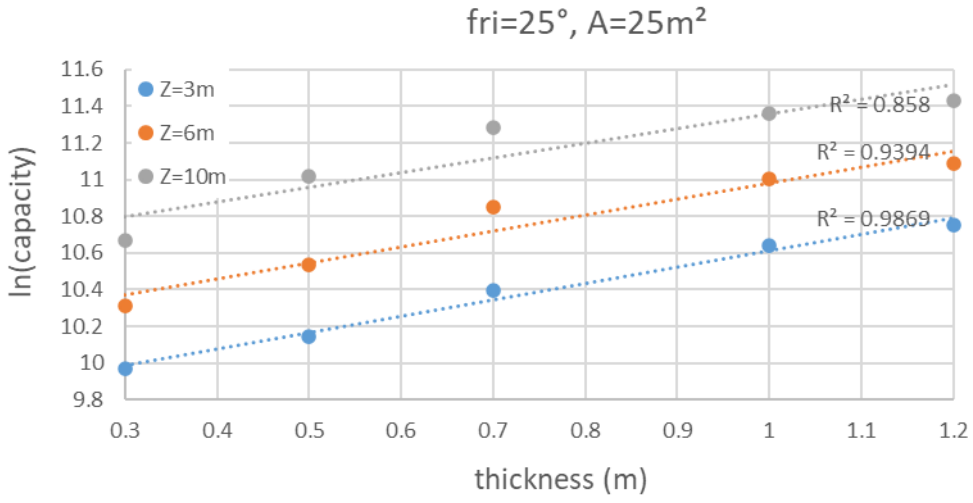

doi:10.6342/NTU202403515

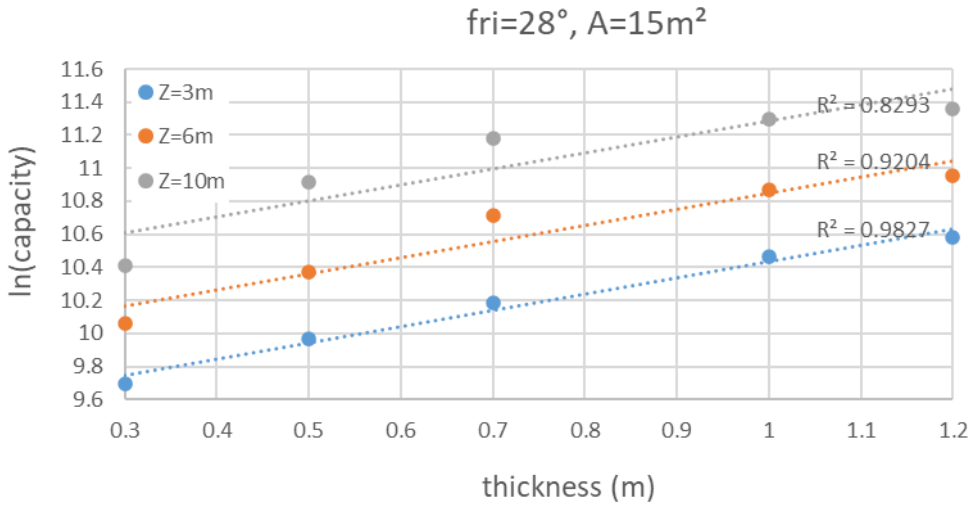

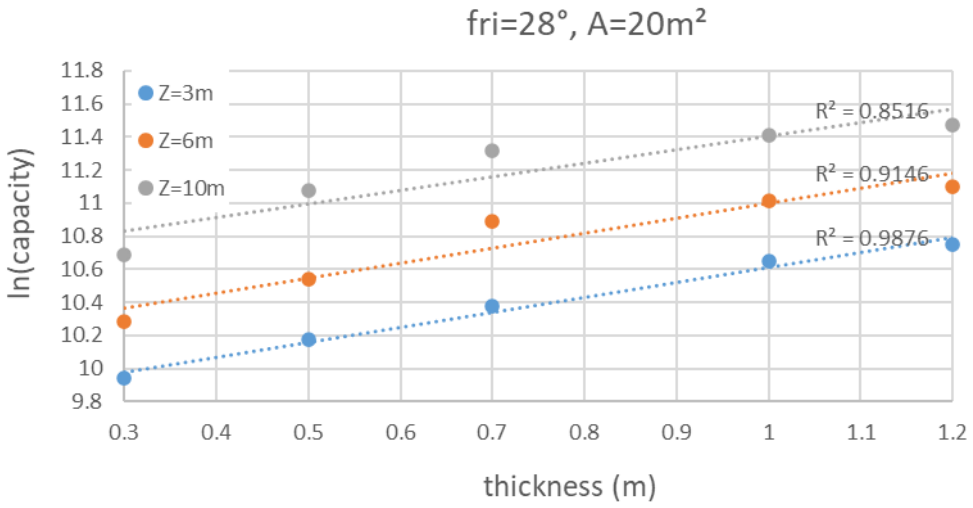

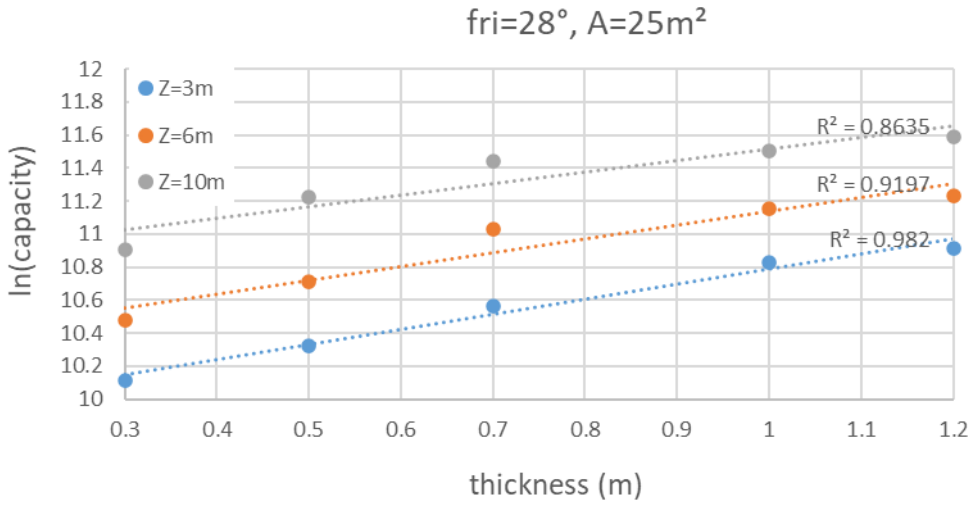

doi:10.6342/NTU202403515

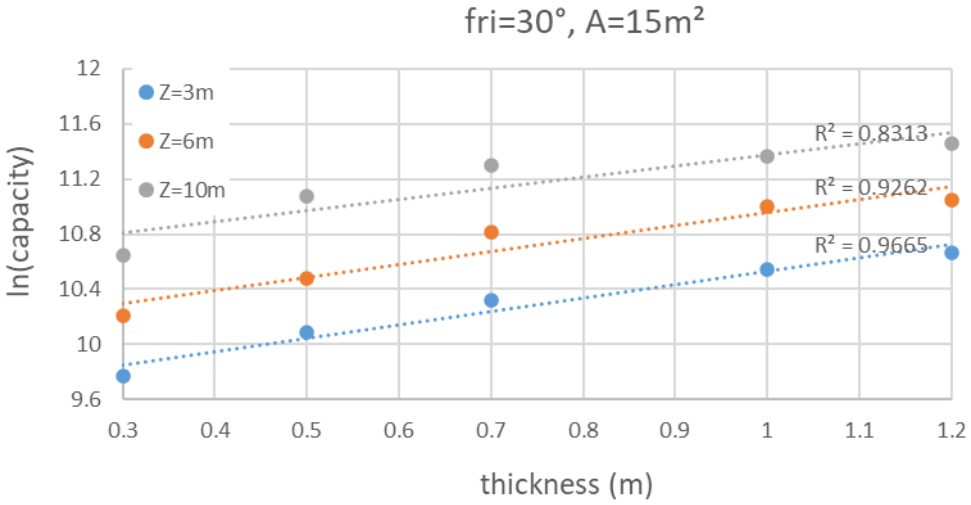

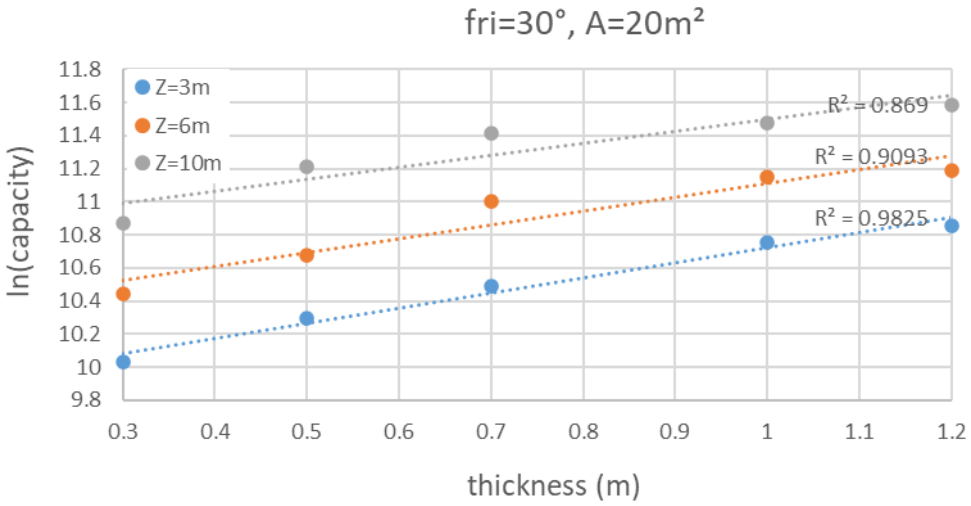

doi:10.6342/NTU202403515

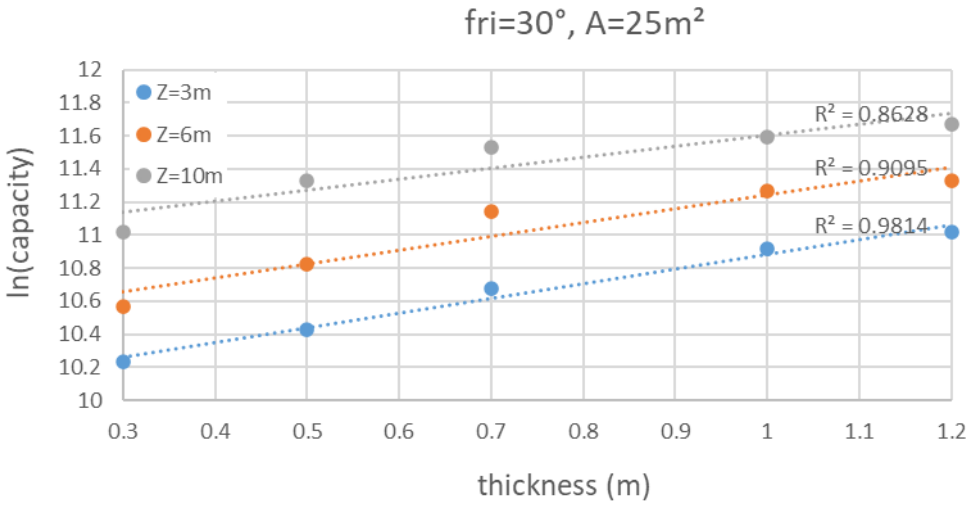

doi:10.6342/NTU202403515

Appendix B: Effective Stress Analysis

Fix Depth and Thickness

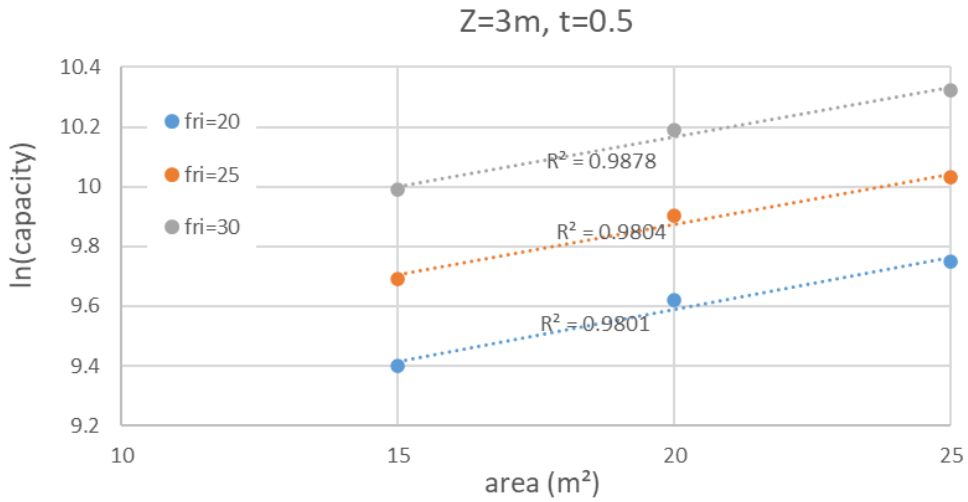

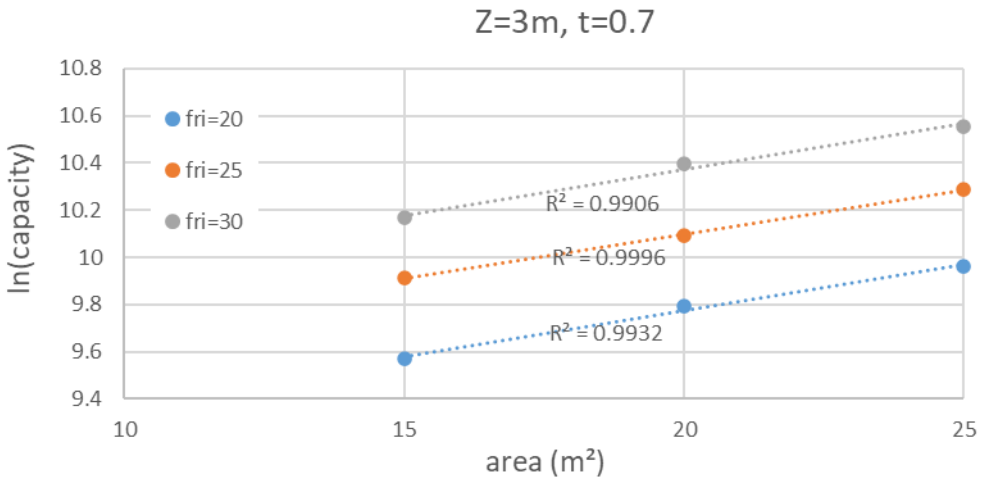

doi:10.6342/NTU202403515

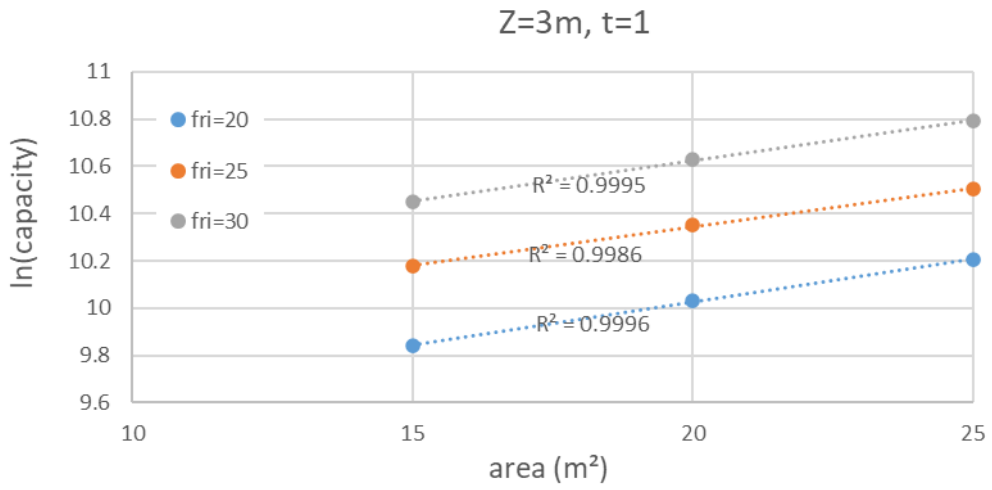

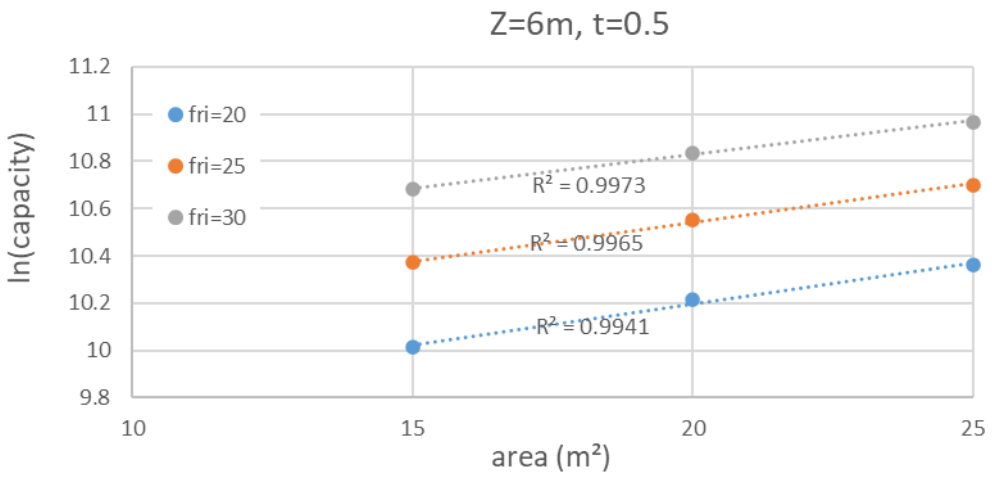

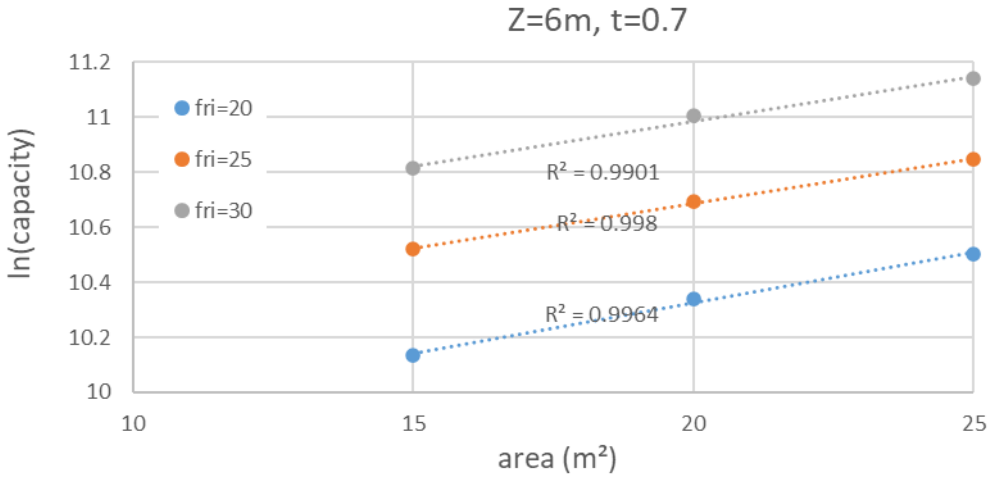

doi:10.6342/NTU202403515

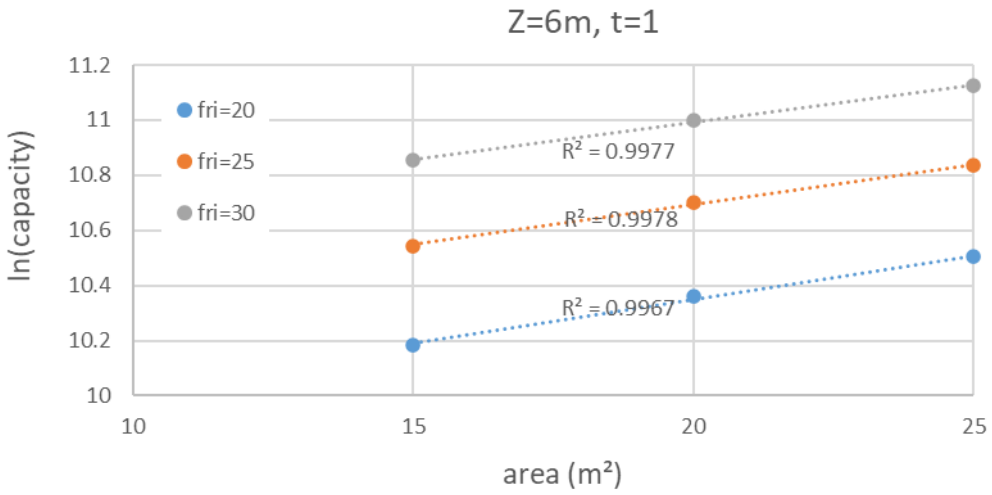

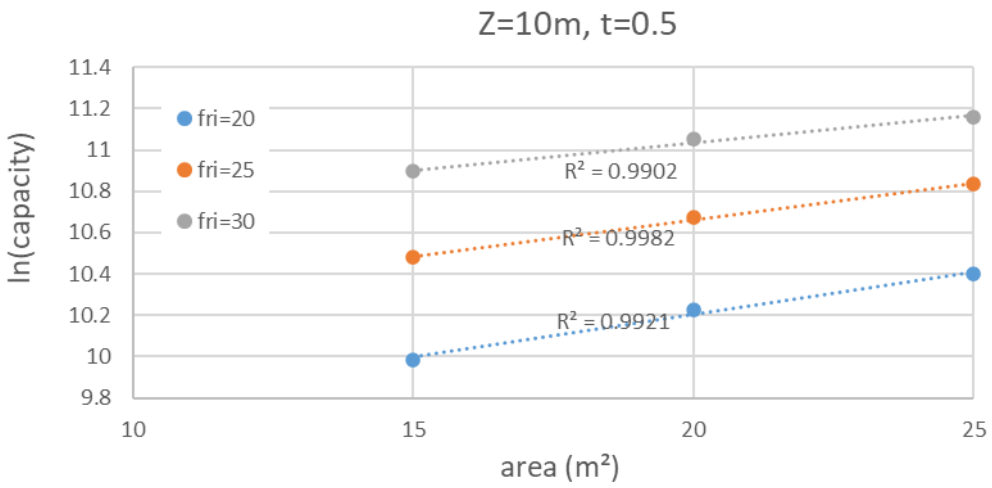

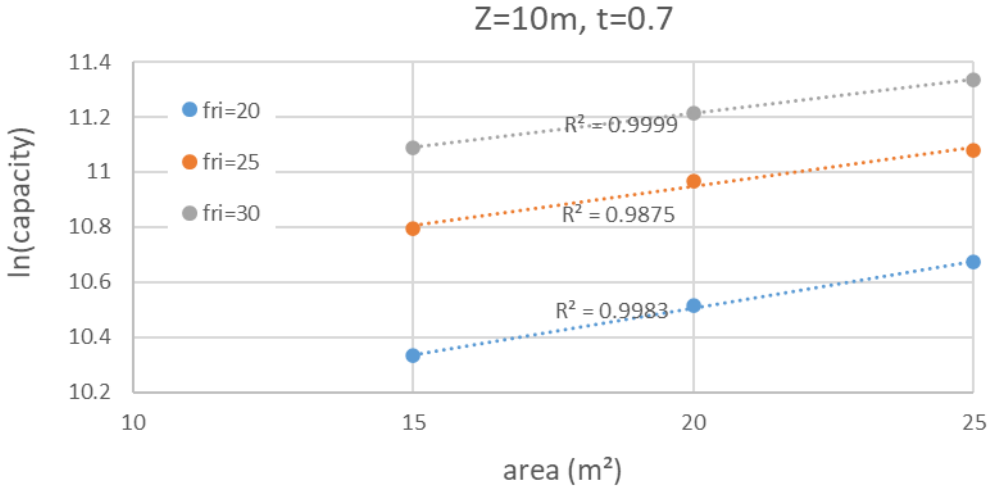

doi:10.6342/NTU202403515

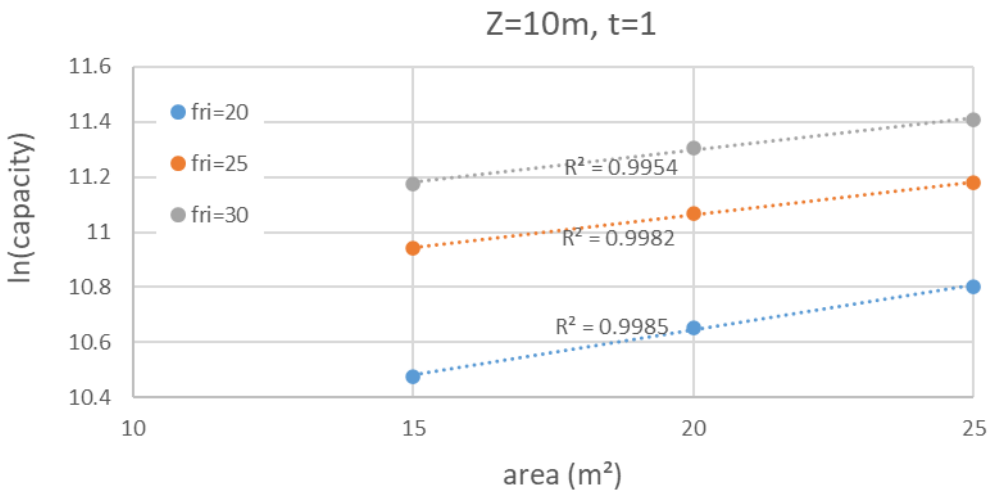

doi:10.6342/NTU202403515

Fix Friction Angle and Fluke Area

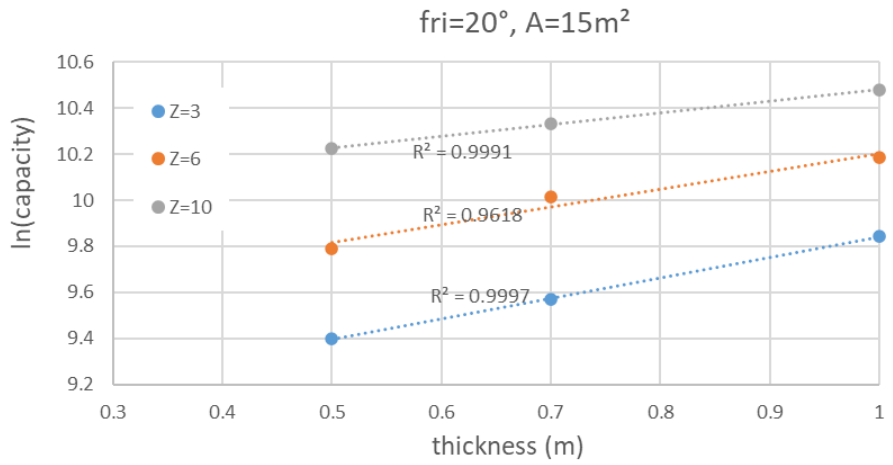

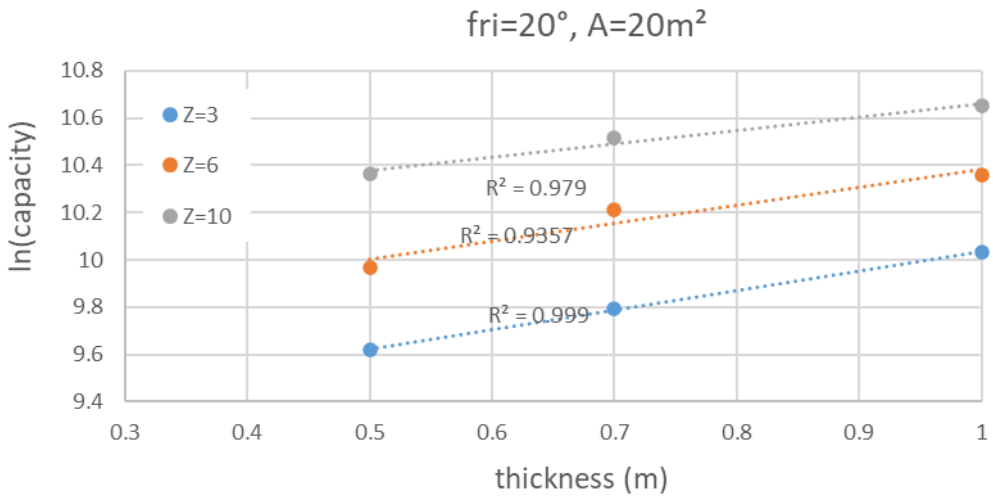

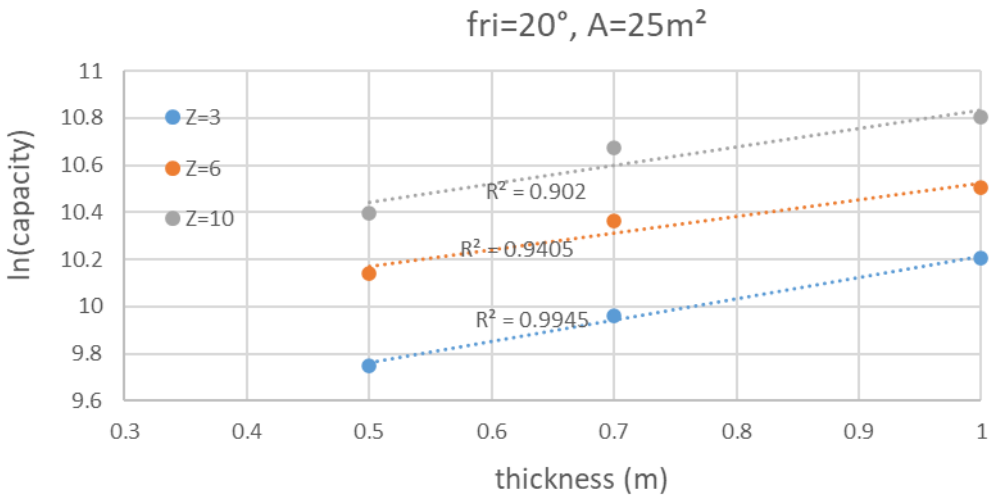

doi:10.6342/NTU202403515

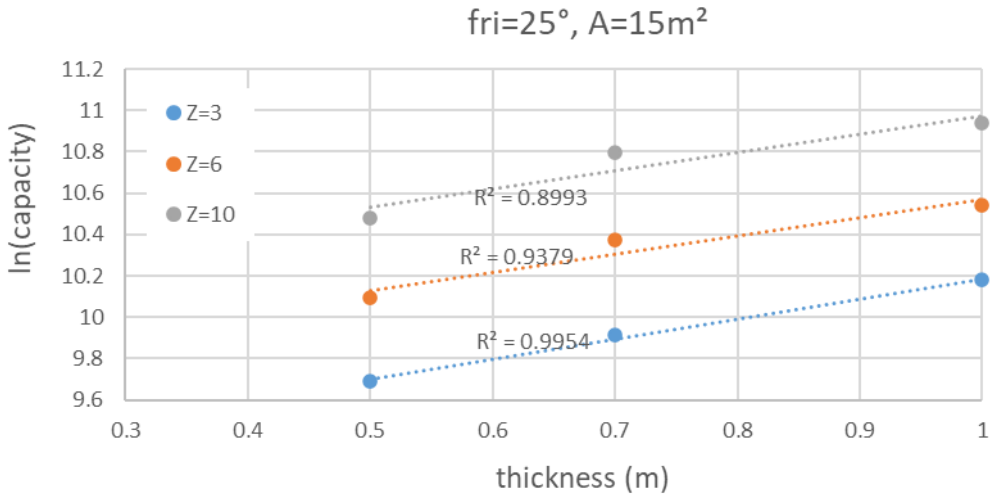

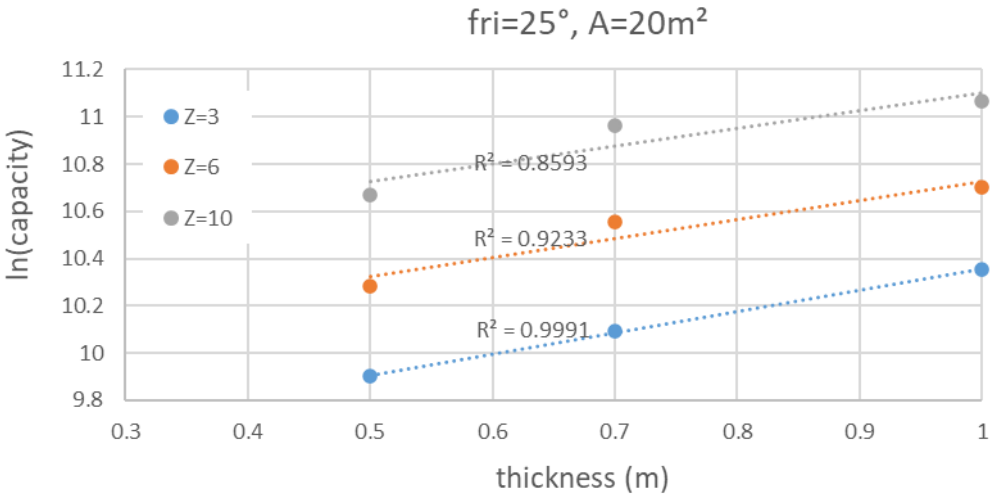

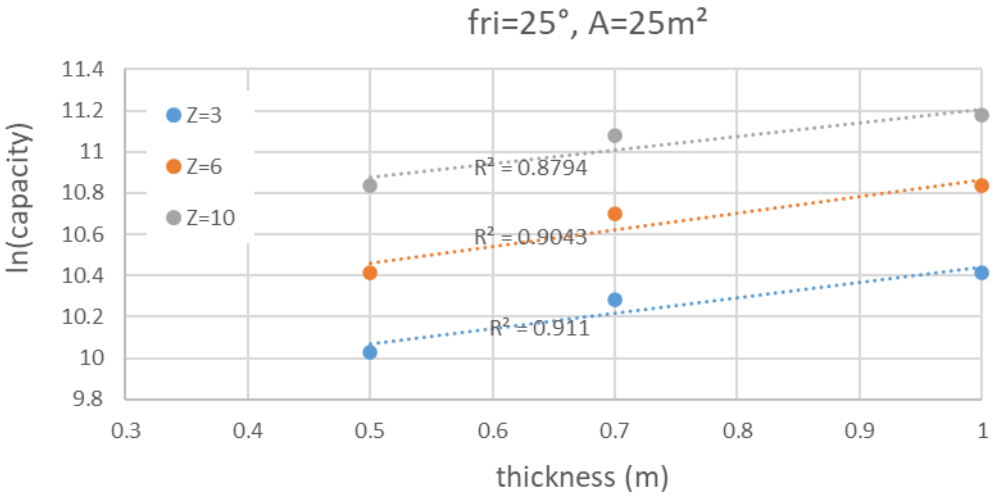

doi:10.6342/NTU202403515

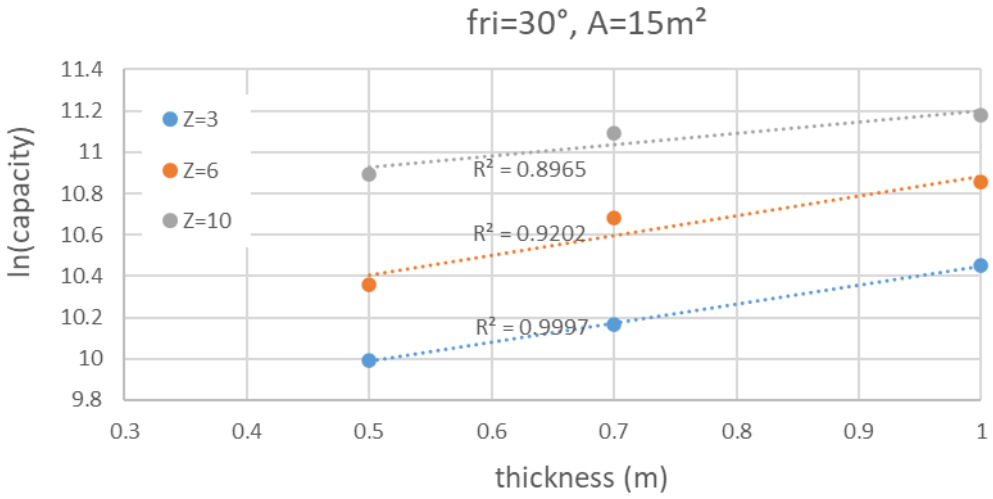

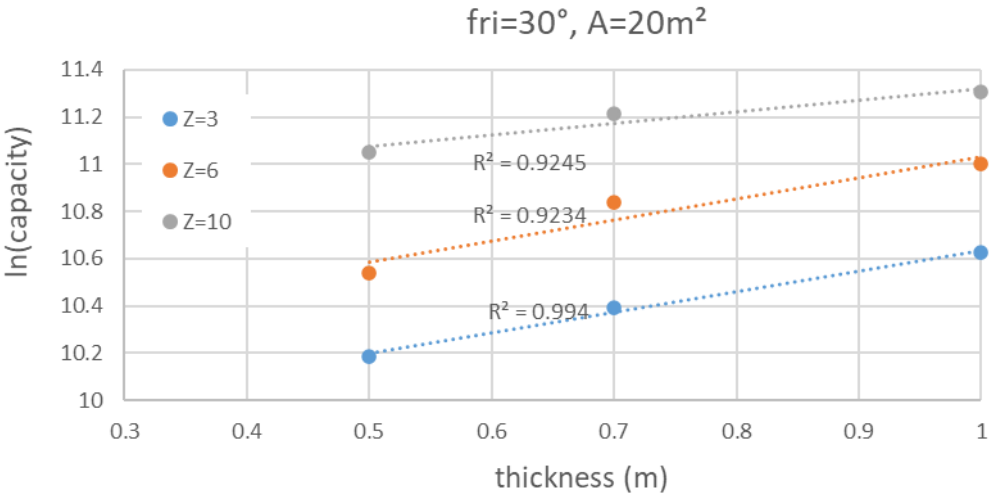

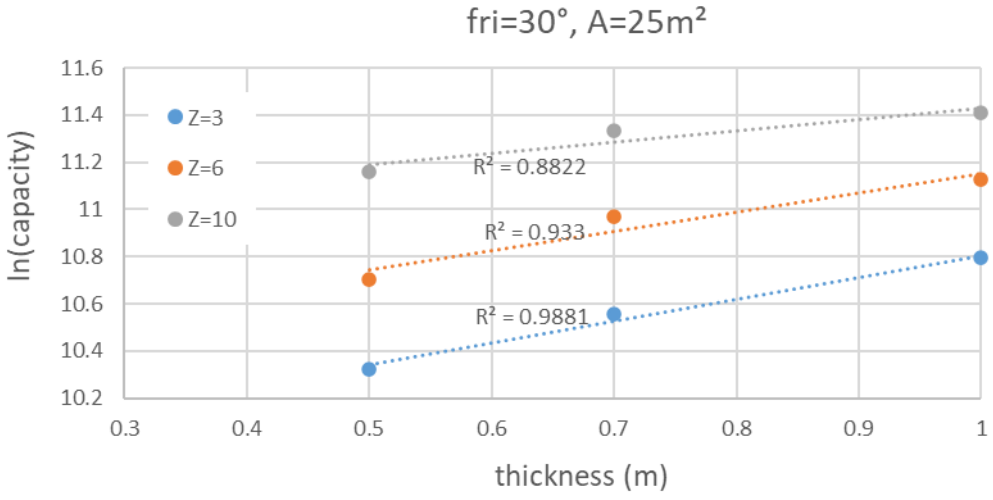

doi:10.6342/NTU202403515